Numerical Methods for Dynamics of Particles in Magnetized Liquids

WITH APPLICATIONS IN MAGNETIC
DENSITY SEPARATION OF END-OF-LIFE PLASTIC
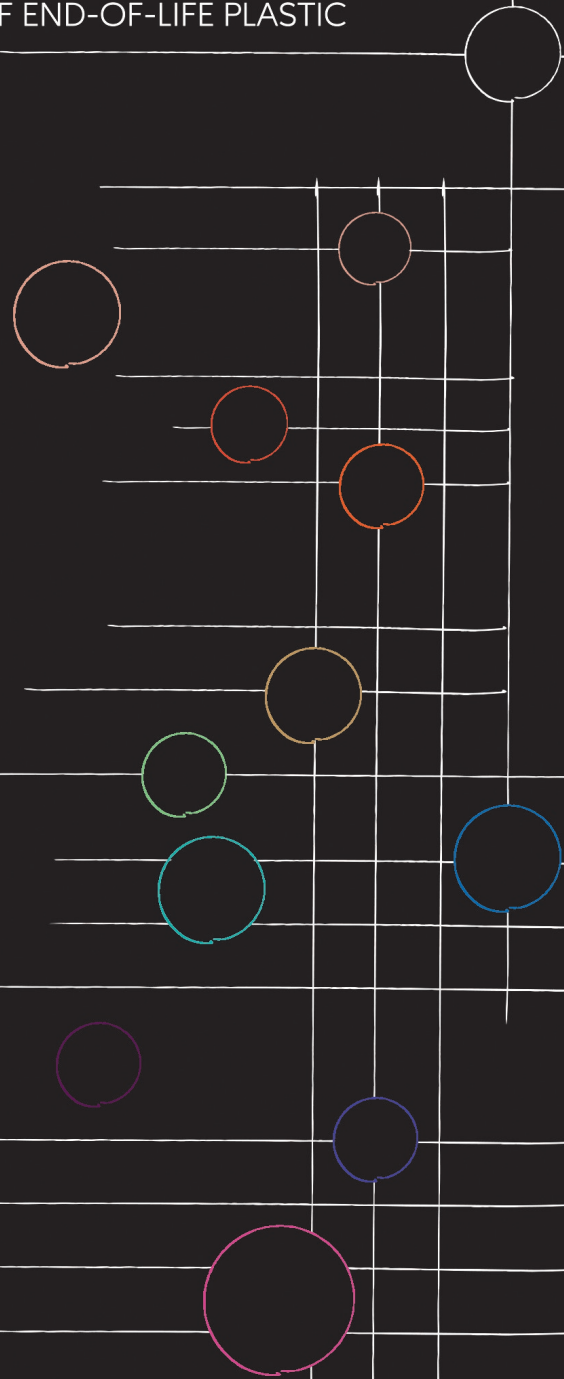
Numerical Methods for Dynamics of Particles in Magnetized Liquids

PROEFSCHRIFT

ter verkrijging van de graad van doctor aan de Technische Universiteit Eindhoven, op gezag van de rector magnificus prof.dr.ir. F.P.T. Baaijens, voor een commissie aangewezen door het College voor Promoties, in het openbaar te verdedigen op maandag 22 februari 2021 om 16:00

door

Sina Tajfirooz

geboren te Shiraz, Iran

Dit proefschrift is goedgekeurd door de promotoren en de samenstelling van de promotiecommissie is als volgt:

voorzitter:	prof. dr. ir. D.M.J. Smeulders	
1e promotor:	prof. dr. J.G.M. Kuerten	
2e promotor:	dr. ir. J.C.H. Zeegers	
leden:	prof. dr.-ing habil. J. Fröhlich	(Technische Universität Dresden)
	dr. ir. W.-P. Breugem	(Technische Universiteit Delft)
	prof. dr. ir. P.C. Rem	(Technische Universiteit Delft)
	prof. dr. F. Toschi	
	prof. dr. ir. A.W. Vreman	

Summary

Numerical Methods for Dynamics of Particles in Magnetized Liquids

The ever-increasing mass-production of plastics over the past 60 years has raised major environmental, economic, and societal concerns. The sustainability of the plastic industry is closely connected to the efficiency of sorting and separation technologies. Magnetic density separation (MDS) is an effective high-resolution method for sorting end-of-life plastic based on plastic type. MDS uses a magnetized fluid to fractionate a mixture by exploiting the Archimedes principle. Optimizing MDS processes requires a fundamental understanding of the collective motion of millimetre-sized particles in flows of magnetically responsive fluids. This dissertation considers the development of an efficient computational framework for the simulation of particle-laden flows commonly occurring in MDS systems.

When particles are introduced to a laminar or turbulent flow of a non-magnetic liquid, they usually undergo inertial effects stemming from the mass of the particles, the added mass of the fluid, and gravity. In magnetized liquids, however, the magnetically-modified pressure distribution inside the fluid introduces an additional force that influences the motion of immersed particles. The magnetic buoyancy force stemming from the polarisation force on fluid elements pushes the immersed particles to equilibrium points that are unique to their mass density. MDS systems exploit this principle to sort mixtures. As particles in MDS are generally produced through a shredding process, their shape can significantly deviate from a sphere. While spherical particles generally tend to move in the direction of the resultant force stemming from local fluid velocity and buoyancy, the motion of non-spherical particles is more complicated. The rotation of non-spherical particles influences their transitional motion even in the absence of inertial effects, making the particle shape an important parameter in MDS processes. Moreover, at appreciable particle volume fractions, inter-particle interactions can strongly influence the collective motion of particles and cannot be disregarded.

The two main approaches to simulating particle-laden flows are point-particle methods (PP-DNS) and particle-resolved methods (PR-DNS). Generally considered as a more accurate approach, PR-DNS methods resolve the flow field around each particle. PP methods, on the other hand, treat particles as points and incorporate force models to couple the fluid and particle momenta. Despite the considerable increase in computational capacities, modelling large particulate systems using particle-resolved methods is extremely expensive. PP-DNS methods, in contrast, offer a computationally efficient framework to simulate particle-laden flows and have been extensively applied to model the collective motion of small particles in laminar and turbulent flows. However, when the particle size increases or when its shape deviates from a sphere, PP-methods require careful adaptions. In this dissertation, we adopt a PP-DNS approach to study the underlying mechanisms in the buoyancy-driven motion of particles in magnetically responsive liquids.

In our first step towards obtaining a fundamental understanding of dynamics of particles in magnetized fluids, we represent the particles by spheres. A four-way coupled point-particle method is presented where all relevant interactions between an exter-

nal magnetic field, a magnetic liquid, and spherical particles are taken into account. Particle-particle interaction is modelled by a hard-sphere collision model which takes the interstitial fluid effects into account. First, the motion of particles in a paramagnetic liquid is studied in single- and two-particle systems. We observe very good agreements between our numerical results and experiments performed in single- and two-particle magnetofluidic systems. Next, we investigate the magneto-Archimedes separation of particles with different mass densities in many-particle systems interacting with the fluid. Our results reveal that history effects and inter-particle interactions significantly influence the levitation dynamics of particles and have a detrimental impact on the separation performance. We also investigate the effects of particle size, and initial distribution on the separation performance. The presented method is shown to be a robust and efficient computational framework for the investigation of flows of magnetically responsive fluids laden with spherical particles.

The next step towards a more realistic simulation of MDS processes is to investigate the effects of particle non-sphericity. We do this by considering ellipsoidal particles. Most of the existing models for fluid-particle interactions of ellipsoidal particles disregard inertial effects. Although such so-called Stoksian models can be applied in the vicinity of particle equilibrium positions, in regions far from the equilibrium positions, or in cases where a background flow is present, such models break down, and both are relevant in the MDS application. To predict the dependencies of steady hydrodynamic interactions of thin oblate spheroidal particles on particle orientation and Reynolds number, we present a novel approach. The conventional empirical correlations that approximate such dependencies are replaced by a neural-network-based correlation to provide accurate predictions for high-dimensional input spaces occurring in flows with non-spherical particles. By performing PR-DNS simulations a database consisting of Reynolds number- and orientation-dependent drag, lift and pitching torque acting on a 1:10 spheroid is collected. A feed-forward neural network is trained and validated with the generated database. The presented statistical approach outperforms existing empirical correlations in terms of accuracy. Moreover, the agreement between the numerical results and experimental observations prove the potential of this new method.

Finally, we present a PP-DNS framework for the investigation of flows laden with non-spherical particles. The particle tracking algorithm is adapted to capture the position and orientation of ellipsoidal particles in a magnetized liquid. A new strategy for two-way force and torque coupling between fluid and particles is presented, and efficient collision detection and response models are employed to describe the collisions of ellipsoidal particles. The results substantiate that at a fixed particle volume, the single-particle levitation time increases with the particle aspect ratio. It is shown that binary collisions have a smaller hampering effect on the levitation motion of 1:2 spheroids than of spheres. Experimental validations reveal that precise prediction of the particle orientation during collisions, requires more accurate models for rotational interactions of ellipsoidal particles with other particles and the carrier liquid. Results of many-particle simulations substantiate the importance of two-way coupling for non-spherical particles. Decreasing the particle aspect ratio from 1 to 0.1 is shown to yield a significant increase in the separation time even when collisions are disregarded. Finally, conclusions drawn from this thesis and possible perspectives of future research are discussed.

About the cover

The circular assembly half of which is visible on the front cover of this book is an artwork created by Mandy Barker, an award-winning international photographer. Through her work, she aims to raise awareness about plastic pollution in the oceans by highlighting the harmful impact of plastic pollution on marine life. This assembly represents a compact arrangement of more than 500 pieces of plastic debris that are found in the digestive system of an albatross chick in the North Pacific Gyre (see the image on the right [31]). The artwork belongs to the series SOUP which is a description given to plastic debris suspended in the sea, with particular reference to the mass accumulation in an area of the North Pacific Ocean known as the Garbage Patch [16].

Contents

1. Introduction

1.1. Background

1.1.1. An overview of plastic imprint

A decade ago, the level of the physical and chemical human imprint on planet earth has reached a comparable level to that of natural geophysical processes [137]. A characteristic marker of human activities is the widespread presence of plastics both on land and in the oceans [50]. The first synthetic plastic was produced in 1907, marking the beginning of the global plastics industry. However, the rapid growth of global plastic production only started in the 1950s. Due to their malleability, durability and low costs, over 65 years, annual production of plastics increased almost 200-fold to reach 381 million tonnes in 2015. The cumulative production until 2015 reaches 8300 million tons [54].

Figure 1.1 summarizes the global plastic production to final fate over the time span 1950-2015. Merely 30% of the total amount of produced plastics was still in use in 2015. About 55% of this total amount was land-filled or discarded, and 8% was incinerated. The share of recycled plastics is only 9%. This indicates that at the global level, plastic is being handled in a highly unsustainable manner yielding a rapid increase in global plastic pollution.
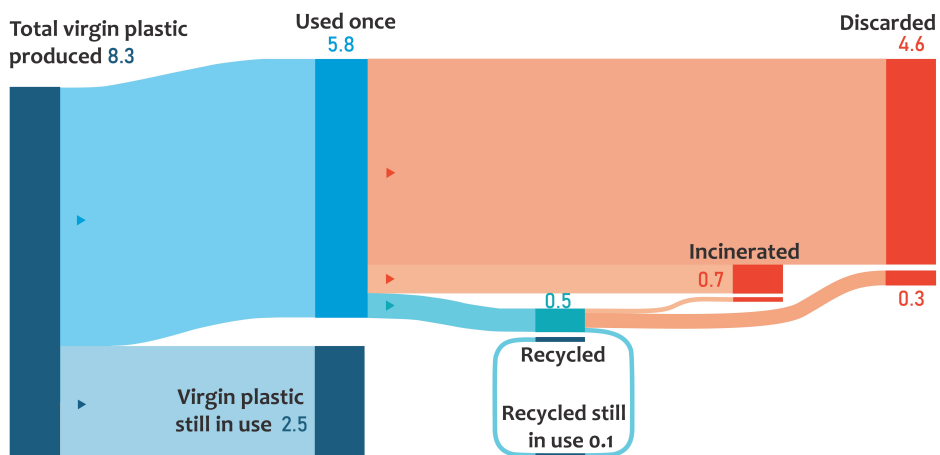
Figure 1.1.: Global plastic production and its fate from 1950 to 2015. The unit of the numbers is billion metric tonne. Retrieved from [54].

The environmental and economic consequences of plastic waste have become visible in the wake of the rapid increase in plastic pollution. The time it takes for the plastics to biodegrade entirely is not clear. Estimated times range from 450 years to never. Plastic

leakage to the environment in the form of macroscopic litter or microplastics damages biodiversity and exhausts the ecosystem services that are vital for life [49]. In 2015, Jambeck et al. [69] estimated that annually between 5.3 million and 14 million tons of plastic enter the oceans just from the coastal areas. Oceans plastic pollution is directly related to the death of millions of marine animals annually. Furthermore, mismanaged plastic waste contributes to climate change through greenhouse gas emissions both from manufacturing new plastic and from waste management.

At a regional level, there is a large gap in the sustainability of plastic management strategies in high-income developed countries and in developing countries. Plastic management in non-EU countries, for example, is differently regulated, and many non-EU countries have less strict regulations regarding plastic waste management. The study of Geyer et al. [54] showed that there is a strong geographical clustering in the mismanaged plastic waste and that Asia is a significant contributor to the world's plastic pollution in the oceans. According to their study, in 2010, China and Indonesia had the highest share of mismanaged plastic waste with approximately 28% and 10% of the global total, respectively. In 2017, China banned all import of non-industrial plastic waste to improve domestic recycling infrastructure and generate internal markets [22].

Although many countries in Europe and North America have high rates of plastic generation per capita, the contribution of most of these counties to mismanaged waste at risk of ocean pollution is relatively low. In 2012, 25.2 Mt of post-consumer plastic was collected in the EU, out of which around 60% was recovered and about 26% was recycled. The remainder of the recovered plastic was likely used as refuse-derived fuel or incinerated [126]. The share of recycled plastic in the EU, the world leader in plastic recycling, is much lower than that of other materials such as paper or metals [126]. The EU has recently taken measures to improve plastic production and waste management. These measures include the European strategy to obtain a circular economy concerning plastics and ambitious goals for the plastic recycling industry [44]. However, economic incentives have led to a lack of transparency about the plastic import to and export from the EU [105]. Traded plastic waste could end up in the oceans, land-filled or be incinerated through inadequate waste management systems.

Throughout the years, the emphasis has been on pre-consumer optimization of plastics while the attention to the post-consumer aspect of plastic products has been much less. Two main ways to change this trend is to either design new plastic products such that they are biodegradable or to increase the recycling rate of end of life plastic. Considering the current momentum of the plastic industry and the amount of piled up plastic waste on earth, the latter solution is deemed to be more effective. Developing efficient plastic recycling systems plays a pivotal role in this transition.

1.1.2. Plastic recycling industry and separation strategies

As can be seen in figure 1.2, there is a huge variety of plastics with a wide range of applications. Some plastic types are predominantly used in specific applications. For example, the use of polyvinylchloride (PVC) in packaging has been reduced in many countries, but PVC, together with polyurethane (PUR) and polystyrene (PS),

PET	HDPE	PVC	LDPE	PP	PS	OTHER
△ 1	△ 2	△ 3	△ 4	△ 5	△ 6	△ 7
PET *Polyethylene terephthalate*	**HDPE** *High-density polyethylene*	**PVC** *Polyvinyl chloride*	**LDPE** *Low-density polyethylene*	**PP** *Polypropylene*	**PS** *Polystyrene*	**OTHER**
Beverage bottles, food jars, clothing and carpet fiber, some shampoo and mouthwash bottles	Detergent and bleach bottles, snack boxes, milk jugs, toys, buckets, crates, plant pots, garden furniture, trash bins	Credit cards, window and doorframes, gutters, pipes and fittings, wire and cable sheathing, synthetic leather	Packaging film, shopping bags, bubble wrap, flexible bottles, wire and cable insulation	Bottle tops, drinking straws, lunch boxes, insulated coolers, fabric and carpet fiber, tarps, diapers	Plastic-foam cups, egg boxes, meat trays, packing peanuts, coat hangers, yogurt containers, insulation, toys	Nylon fabrics, baby bottles, compact disks, medical storage containers, car parts, watercooler bottles
11%	**14%**	**5%**	**20%**	**19%**	**6%**	**24%**

↑ *Percentage of global plastic waste, 2015*

Ease of recycling by type

△ Easy △ Difficult
△ Manageable △ Very difficult

Figure 1.2.: Typical applications of key plastic types worldwide and their contribution to the global plastic waste [111]. Ease of recycling varies per region: North America shown here.

is one of the key plastic types used in the building and construction sector. In the packaging markets, the polyolefins (i.e. polypropylene (PP) and polyethylene (PE)), polyethylene terephthalate (PET) and PS dominate. A major challenge in recycling plastic wastes is the separation of different plastic types. Due to their inherent molecular immiscibility and differences in processing requirements, most plastic types are incompatible. Impurities in recovered plastic deteriorate the quality of the product leading to the so-called "plastic down-cycling". For example, PP and PE are present as a mixture in end-of-life polyolefin fractions. The grade of the PP and PE should be better than 97% to be reused as a high-quality product [14, 125]. Therefore, a fast and efficient method for sorting that ensures a very low, ideally zero, level of impurity of the processed plastic is needed.

Among different recycling methods, mechanical recycling represents the major plastic recovery approach. A typical post-consumer recycling procedure consists of several steps: collection, sorting, cleaning, size reduction and separation. While compounding and cleaning technologies for polymer solid waste have significantly been improved, the development of efficient sorting and separation technologies still lags behind. Several promising methods have been investigated and applied. See, for example, Singh et al. [135] for an extensive review. To increase the recycling rate over a broad range of polymeric materials, efficient and economical separation technologies are required which are capable of targeting polymers by type and colour.

1.2. Magnetic density separation

The separation of mixtures of plastics based on their mass density is one of the most effective, high-capacity methods in industrial separation technologies for recycling plastic waste [53]. Due to the simplicity, automatability and flexibly of mass-density-based separation methods in operation, density-based separation is globally the most

widely used material separation process. A sink-float process can give an effective mass-density-based separation with both high grade and high recovery, provided the differences in mass density between the sub-populations is sufficiently large. Sink-float methods are used to separate polyolefins from PET in bottle recycling [37]. Extracting high-grade PP and PE fractions from typical shredder residue requires multi-step pre-separation [14]. A one-step continuous separation by multiple "cut mass densities" can be achieved by the magnetic density separation (MDS) technique [14, 88].

MDS is similar to the conventional sink-float methods as both exploit the Archimedes principle to separate materials based on mass density. MDS, however, incorporates magnetically responsive liquids and engineered magnetic fields to create a gradient of effective/apparent mass density within the liquid, which enables the continuous segregation of a mixture in one go [114, 124]. Exposure to a non-uniform magnetic field leads to a non-uniform pressure field within the liquid which, in turn, makes the buoyancy force acting on an immersed body position-dependent. A vertical gradient of the magnetic field makes the buoyancy force on a particle dependent on its vertical position inside the liquid, resulting in stable equilibrium heights which are unique to the mass density of the particles. Provided the residence time is sufficient and particles are free of air bubbles, particles released in the liquid travel to the position corresponding to their mass density and can subsequently be separated from the mixture. This high-resolution technique is capable of separating particles characterized by very close mass density values, such as polypropylene (PP) and polyethylen (PE) or PVC and rubber [88, 125]. A schematic representation of an MDS system is shown in figure 1.3.
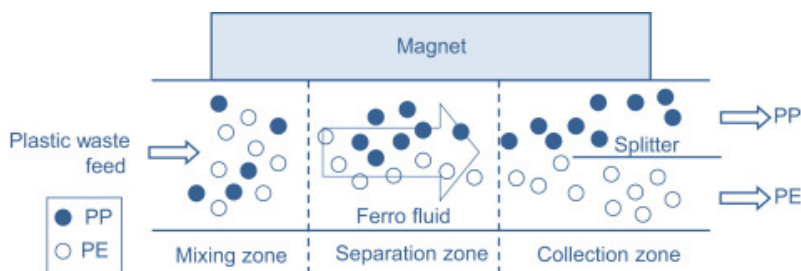
Figure 1.3.: Schematic representation of a magnetic density separation system for polypropylene (PP) and polyethylene (PE) (retrieved from Serranti and Bonifazi [124]).

The MDS approach makes use of only a single property of the particles, namely their mass density and is not dependent on the shape or size of the particles. The low viscosity and surface tension of the sorting medium in MDS systems enables the segregation of millimetre-sized mixtures in the separation zone. Sorted fractions are collected downstream of the separation zone in the so-called collection zone. Next to end of life plastic, MDS has been applied to separate nonferrous minerals, seeds, toxic wastes and electronic waste [14, 35, 75, 88, 100, 103, 114, 129, 136, 148, 156].

The performance of an MDS system relies on multiple elements in the system: magnets, magnetic liquid, level of turbulence in the separation zone and particle properties. That is why the optimization of magnetic density separators, requires in-depth

multidisciplinary knowledge of magnetostatics, chemistry, fluid mechanics and particle dynamics. In the following sections, we introduce different elements of a typical industrial MDS system.

1.2.1. Design of magnet systems

Magnets as one of the most important elements of MDS systems must satisfy multiple important criteria. First, the maximum magnetic field strength and its local gradient should be such that the resulting "apparent density" field is compatible with the mass densities of the particles to be separated, magnetic properties of the magnetic liquids, and the geometry of the separation channel. The magnitude of the magnetic field gradient and its direction directly determine the equilibrium positions of the particles, as well as their motion towards these positions. A high-intensity magnetic field enables the application of more dilute magnetic liquids which are less viscous and more economical. Furthermore, the induced magnetic field should have negligible transverse non-uniformities to avoid the "wiggling" motion of particles and the resulting reduction in the separation accuracy in the separation zone. A high-strength magnetic field can be generated by incorporating superconducting magnets such as niobium-titanium (NbTi) magnet systems. In non-ideal finite-length magnets, a not perfectly vertical magnetic field gradient is inevitable, which can hamper the motion of particles. Therefore, to prevent particle clogging, a certain minimum streamwise flow velocity should be sustained in the separation zone. This requirement, in turn, influences the minimum length of the magnet system to achieve an acceptable separation performance given the time required for the particles to reach their equilibrium positions.

1.2.2. Process liquid

The separation medium in industrial MDS systems is a synthetic colloidal magnetic fluid called ferrofluid. Ferrofluids which were first introduced by Papell [110] have much higher magnetic susceptibility than natural paramagnetic salt solutions or liquid oxygen, a property referred to as "superparamagnetism" [19, 118]. These colloidal ferromagnetic liquids contain nanometer-sized ferrous particles which are stabilized using surfactants which prevent the particles from approaching each other too closely.

In practical MDS systems, a large vertical distance is required over which a stable magnetic pressure is generated within the ferrofluid. This implies that the incorporated magnetic liquid should sustain its stability under the influence of strong magnetic fields over a long time interval. The feasibility of an industrial MDS system requires that such stable process liquids are cheap. Furthermore, its magnetic, physical and chemical properties should satisfy the magnetostatic and fluid-dynamic MDS design constraints. The chemical properties and colloidal stability of ferrofluids in MDS applications are subject to research [145, 146] with the aim to understand the nano-scale behaviour of ferrofluids, and therefore obtain optimal macroscopic properties.

1.2.3. Fluid-dynamical aspects

From the fluid mechanics viewpoint, the performance of MDS systems is closely related to the dynamics of dispersed particles in the flow of a magnetized liquid. The motion of particles, in turn, is influenced by any disturbance in the flow. To reach the necessary separation accuracy to obtain high-quality secondary products in one step, MDS needs to be sensitive to very small differences in the mass densities of the input materials. For example, for household packaging and car components, a separation inaccuracy in mass density as low as 1% ($10\,\mathrm{kg/m^3}$) is required [66]. This makes preventing any phenomenon which disturbs the motion of particles in the separation zone of great importance. Therefore, the turbulence level in the separation zone is a crucial aspect of MDS systems. Moreover, the motion of particles generates particle-induced disturbances which can negatively affect the separation performance.

1.2.3.1. Turbulence

For optimal performance of MDS systems, the turbulence level in the separation zone should be kept as low as possible. In new-generation MDS systems multiple measures are taken to maintain an ultra-low turbulence level [66] in the separation zone. First, flow laminator structures such as grids and honeycombs are mounted upstream of the separation zone to break up the large vortical structures and annihilate the transverse velocity in the flow [86]. Second, by incorporating moving walls at the top and bottom of the channel, the formation of boundary layers and transition to turbulence in the vicinity of the walls is circumvented [114].

Although design and usage of honeycomb flow straighteners have been very well established in the context of turbulence reduction in wind- and water-tunnels, their application to achieve the ultra-low turbulence required in MDS needs further research. The break-up of individual velocity profiles and vortex shedding behind such flow laminator elements can give rise to honeycomb-induced turbulence with an appreciable intensity which is detrimental to the performance of MDS systems.

1.2.3.2. Particle-fluid-particle interactions

It is well-known that flow field in the particle-laden flows can be substantially modified by the presence of the particles if the size of the particles is larger than the Kolmogorov length scale [42, 150]. This effect is further enhanced at higher particle volume fractions. At appreciable volume fractions, inter-particle interactions become important, making the particle-fluid-particle interactions more complex. Moreover, particle-fluid-particle interactions are shown to be considerably different for non-spherical particles leading to a substantial difference in the collective motion of particles [149]. Small non-spherical particles tend to react to small scales of the flow, and exhibit a rotational motion which has contributions from the fluid vorticity as well as its strain rate. Non-spherical particles in turbulent flows are shown to give rise to preferential orientation which is highly dependent on their shape.

The dynamics of particles in MDS is influenced by the coupled hydrodynamic and

magnetic interactions between an external magnetic field, a magnetic fluid, and millions of immersed poly-dispersed particles generated through a shredding process. In the absence of an external magnetic field, particles in MDS of end-of-life plastic behave like tracers as they have particle-to-fluid mass density ratios in the order of one. Once the magnetic field is turned on, the magnetically induced buoyancy-driven motion of a particle towards its equilibrium position provides a new and interesting type of particle motion. This dissertation addresses the design and application of a computational framework for the simulation of the collective motion of spherical and non-spherical particles in flows of magnetically responsive liquids. The following sections provide the preliminary theoretical background for studying particle-laden flows of magnetized fluids and introduces the scope of this work.

1.3. Preliminaries

1.3.1. Ferrohydrodynamic theory

Ferrohydrodynamics (FHD) is a branch of mechanics which addresses the motion of a magnetic fluid under the influence of forces of magnetic polarisation in the absence of electric currents. The development of ferrohydrodynamics theory started in the 1960s with the production of synthesized magnetic fluids (ferrofluids). Ever since magnetic liquids have been employed for several applications such as instrumentation, lubrication, printing, vibration damping, drug targeting, and material separation. In FHD free electric charges are normally absent, and the body force is due to the polarisation force which requires fluid magnetization in the presence of magnetic field gradients or discontinuities [118].

Neuringer and Rosensweig [101] were the first to propose a model for the motion of a magnetized fluid. This model is an extension to the Navier-Stokes equation where next to viscous and inertial effects the effect of magnetic forces is also taken into account. In flows where the orientation of the magnetic field slowly shifts relative to translating and rotating fluid elements, magnetization relaxation processes can be disregarded and the magnetization and the magnetic field can be assumed to be collinear ($\boldsymbol{M}\|\boldsymbol{H}$). Under this condition the so-called quasi-equilibrium ferrohydrodynamics model reads [118, 131]

$$\rho\left(\frac{d\boldsymbol{u}}{dt} + \boldsymbol{\nabla}\cdot(\boldsymbol{u}\otimes\boldsymbol{u})\right) = -\nabla p + \mu\Delta\boldsymbol{u} + \rho\boldsymbol{g} + \mu_0 M\nabla H; \quad \text{div}\,\boldsymbol{u} = 0, \qquad (1.1)$$

where $\otimes$ indicates tensor product, $\boldsymbol{u}$, p and μ are the fluid velocity, pressure and dynamic viscosity respectively, $\boldsymbol{g}$ is the gravitational acceleration, μ_0 the magnetic permeability in vacuum, $M = \|\boldsymbol{M}\|$ the magnitude of fluid magnetization and $H = \|\boldsymbol{H}\|$ is the magnetic field strength which is related to the magnetic induction $\boldsymbol{B}$ through $\boldsymbol{B} = \mu_0\boldsymbol{H} + \boldsymbol{M}$. The magnetic field strength and magnetic induction are determined by Maxwell's equations of magnetostatics in the absence of a current density and electric field:

$$\text{div}\,\boldsymbol{B} = 0; \quad \text{rot}\,\boldsymbol{H} = 0. \qquad (1.2)$$

1.3.1.1. Bernoulli equation and pressure in magnetized fluids

Under the assumption of a stationary incompressible potential flow of an ideal (homogeneous) magnetic fluid, and with gravity acting in the y- direction, (1.1) is simplified to the ferrohydrodynamics Bernoulli equation:

$$p + \rho u^2/2 + \rho_{\mathrm{f}} g y - \int_0^H M dH = \text{const.} \tag{1.3}$$

In the absence of an external magnetic field, the magnetic contribution to the static pressure is zero and (1.3) reduces to the conventional Bernoulli equation. For a fluid at rest writing the Bernoulli equation for two points inside the liquids gives:

$$p_1 + \rho_{\mathrm{f}} g y_1 - \int_0^{H_1} M_1 dH = p_2 + \rho_{\mathrm{f}} g y_2 - \int_0^{H_2} M_2 dH \tag{1.4}$$

It follows directly from (1.4) that the hydrostatic pressure gradient inside the liquid has two contributions, namely a gravitational contribution and a magnetic contribution. MDS exploits this principle to create the desired pressure field by incorporating the right combination of magnetic field and liquid magnetization. The steady-state FHD Bernoulli equation describes the working principle of MDS devices. Rosensweig discovered in (1966a) that "a stable levitation is possible if a non-magnetic object is immersed in a magnetic liquid and is brought into the presence of an appropriate non-uniform magnetic field".

By combining the gravitational and magnetic contributions to the static pressure inside the liquid one can express the static pressure as

$$p_{\mathrm{static}} = -\rho_{\mathrm{f}} g y + \mu_0 \int_0^H M dH = -\rho_{\mathrm{f,a}}(y) g y, \tag{1.5}$$

where

$$\rho_{\mathrm{f,a}}(y) = \rho_{\mathrm{f}} - \frac{\mu_0}{g y} \int_0^y M \frac{dH}{dy} dy \tag{1.6}$$

can be interpreted as the "apparent mass density" of a magnetized liquid. Once a container filled with a magnetic liquid is exposed to a vertical magnetic field gradient, the fluid-magnetic pressure changes such that particles with well-chosen mass densities stably levitate at heights corresponding uniquely to their mass densities. At these stable positions the apparent mass density of the fluid is equal to that of the particle. This phenomenon which we refer to as magneto-Archimedes levitation is illustrated in Figure 1.4.

1.3.1.2. A note on fluid magnetization behaviour: paramagnetism vs superparamagnetism

As shown in section 1.3.1.1, the fluid-magnetic pressure inside a quiescent magnetized liquid depends on the gradient of the magnetic field and on the magnetization
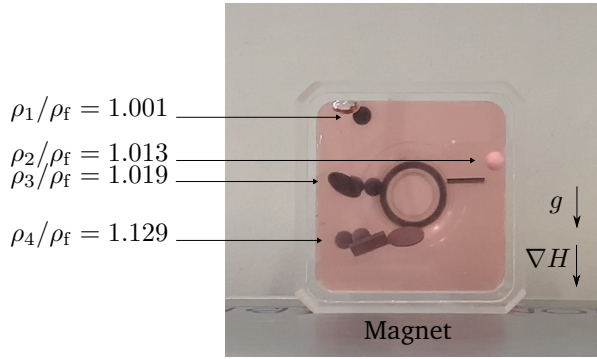
Figure 1.4.: Magneto-Archimedes levitation of a four-component plastic mixture in a magnetized liquid. The magnetic liquid is a saturated solution of $MnCl_2$ salt with $\rho_f = 1402 \, kg/m^3$ (Photograph courtesy R. Dellaert).

of the liquid. When studying magnetic liquids, one should distinguish between two major types of magnetization behaviour: paramagnetism and superparamagnetism. A Ferrofluid, as the principal magnetic fluid in FHD, is a suspension of nanometer-sized particles in a continuous medium. Stable ferrofluids do not settle out. Such ferrofluids are composed of small (3-15 nm), magnetic, single-domain particles coated with a molecular layer of dispersant and suspended in a liquid carrier. A typical ferrofluid consists of about 10^{23} particles per cubic meter and is opaque to visible light. In the absence of a magnetic field, these particles are randomly oriented. As the magnetic field strength increases, more and more particles align with the magnetic field direction and the fluid magnetization increases. At a sufficiently high magnetic field strength, once the particles are completely aligned with the magnetic field, the fluid magnetization saturates. Under the assumption of quasi-equilibrium FHD, this so-called superparamagnetic behaviour can be approximated by the adapted classical theory of Langevin [118, 131]:

$$\frac{M}{M_{sat}} = \coth \alpha - \frac{1}{\alpha} = \mathcal{L}(\alpha), \tag{1.7}$$

where M is the magnetization magnitude of the liquid which is collinear with the applied magnetic field H, M_{sat} is the saturation magnetization of the fluid, $\alpha = \mu_0 m H / (k_B T)$ is the Langevin argument with k_B denoting the Boltzmann constant, T the temperature and m the average dipole moment of magnetic nanoparticles. The magnitude of the fluid saturation magnetization is the sum of the magnetic moments of the suspended magnetic particles in a unit volume of the suspension:

$$M_{sat} = \phi_m M_{sat,p}, \tag{1.8}$$

where ϕ_m is the volume fraction of the nanoparticles, and $M_{sat,p}$ is their saturation magnetization.

In paramagnetic salt solutions where all moment directions are equally probable [19], or at low magnetic field strengths where $\alpha << 1$, so that $\mathcal{L}(\alpha) \approx \alpha/3$ a magnetic liquid exhibits paramagnetic behaviour. Figure 1.5 **(a)** compares the magnetization behaviour of a ferrofluid typically used in MDS systems with $M_{sat} = 650 A/m$ ($m = 3.46 \times 10^{-19} \, A/m^2$), with a saturated solution of $MnCl_2$. It can be seen that the

ferrofluid exhibits paramagnetic behaviour only at very low magnetic field strengths. The influence of the magnetization behaviour in the MDS context is illustrated in figure 1.5 **(b)** where the apparent mass densities of the two liquids exposed to an external magnetic field gradient are plotted as functions of the vertical distance from the magnet surface. Due to its stronger magnetization, the range of apparent mass density within a ferrofluid ($0.5 < \rho_p/\rho_f < 1$) is larger than that of a paramagnetic salt solution ($0.85 < \rho_p/\rho_f < 1$). Moreover, the height over which the gradient of apparent mass density is nonzero is around a factor of two larger in a ferrofluid.

(a)

(b)
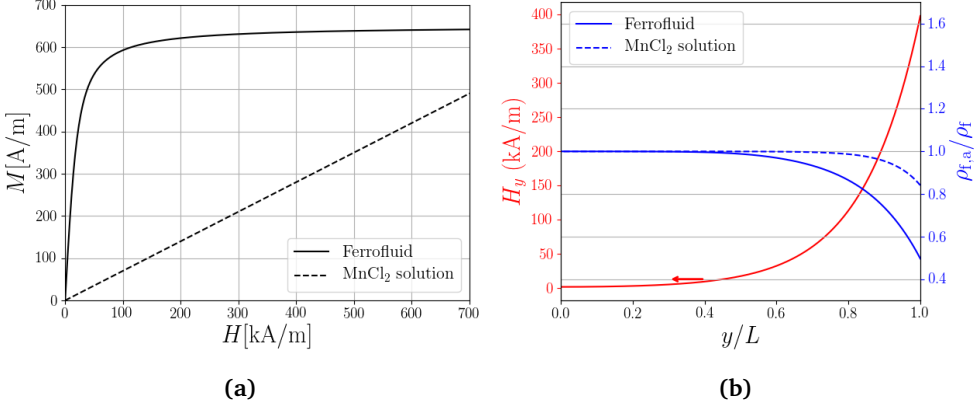
Figure 1.5.: (a) Magnetization behaviour of a ferrofluid with $M_{\text{sat}} = 650$ A/m ($m = 3.46 \times 10^{-19}$ A/m^2) and of a saturated MnCl$_2$ solution with $\chi = M/H = 7 \times 10^{-4}$. **(b)** Apparent mass density of the two liquid when exposed to a magnetic field described by $H = H_0 e^{-\pi(L+y)/p}$ with $H_0 = 422$ kA/m, $p = 0.118$ m, and $L = 0.4$ m. The mass density of the ferrofluid is $\rho_{\text{f,ferr}} = 1010$ kg/m^3 and that of the MnCl$_2$ solution is $\rho_{\text{f,MnCl}_2} = 1400$ kg/m^3.

1.3.2. Magneto-fluidic systems considered in this dissertation

1.3.2.1. Magnetic liquid

In this work, we chose to consider a paramagnetic MnCl$_2$ solution as the separation medium. The major drawback of paramagnetic salt solutions is their higher viscosity compared to diluted ferrofluids. Due to the low magnetic susceptibility of paramagnetic liquids, achieving high magnitudes of magnetization requires a high-concentration of salt. The dynamic viscosity of such saturated solutions is about four times larger than that of a diluted ferrofluid with a comparable magnitude of magnetization. The high viscosity of the fluid increases the resistance against the levitation motion of the particles and is therefore not favourable in practical MDS applications. Our choice is, however, founded on the following reasons:

1. The most important reason is the transparency of this liquid which enables optical measuring methods such as particle tracking velocimetry.

2. The more simple linear dependency of the magnetization behaviour of param-

agnetic liquids reduces the number of influence parameters in the mathematical model for the fluid behaviour.

3. The validity of quasi-equilibrium FHD theory for such paramagnetic liquids simplifies the model which describes the motion of the fluid by circumventing the need to solve a separate equation for the fluid magnetization [130]. Moreover, we can get around magnetoviscous and other dynamical effects which can become important in colloidal ferrofluids.

We should note that the framework presented in this dissertation is used for extensive studies on MDS in ferrofluids under the quasi-equilibrium FHD assumption. However, due to proprietary reasons, these are not included in this thesis.

1.3.2.2. Magnetic field

To further reduce the number of influence parameters in our study, we consider 1D magnetic fields which decay exponentially with the vertical distance from the surface of the magnet. This type of magnetic field can be generated by a specific assembly of alternating magnets called Halbach array [59]. The idea behind Halbach arrays is to create a wavelike magnetization pattern inside the array which results in an amplified magnetic field strength on one side (strong side) of the array, while on the other side (weak side), the magnetic fluxes of individual magnets cancel each other. A schematic representation of a Halbach array is shown in figure 1.6.
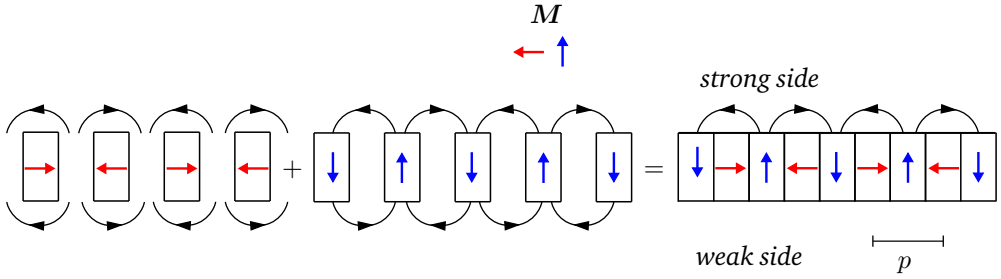
Figure 1.6.: A schematic of a discrete Halbach array with the pole size p, and the corresponding magnetic field lines. The magnetization of each magnet in the array is rotated $90°$ relative to that of the neighbouring magnets.

For an ideal infinite Halbach array where the magnetization inside the array is continuous and periodic, the magnetization vector can be written as $\boldsymbol{M} = (M_{\mathrm{r}} \cos kx)\boldsymbol{i} - (M_{\mathrm{r}} \sin kx)\boldsymbol{j}$, where M_r is the remnant magnetization and k is the spatial wave number. In the absence of an electric current, the Maxwell equation can be solved to obtain the magnetic induction on the strong side of the array [90]. The magnitude of the magnetic field on the strong side of the array reads $H_{\mathrm{strong}} = M_r \left(1 - e^{-\frac{\pi}{2}}\right) e^{-\frac{2\pi y}{\lambda}}$, where $\lambda = 2\pi/k$ is the magnetization wave length. The reader is referred the paper of Mallinson [90] for the derivation.

1.4. Objective and Outline

The opacity of the carrier liquid in industrial MDS systems on the one hand, and the large number of particles in these systems, on the other hand, make the application of experimental techniques to industrial MDS systems very challenging, if not impossible. Developing predictive models for capturing the collective motion of particles is, therefore of high practical importance in optimizing MDS systems. These models can be employed to quantify the spatial and temporal characteristics of the motion of particles in magnetized liquids and provide insights into the influences of parameters such as the particle shape and size, the magnetic field design, and flow disturbances on the performance of MDS systems. This dissertation aims at developing an accurate and efficient numerical framework for the buoyancy-driven motion of particles in the flow of a magnetized liquid.

As the starting point of our study, we make the assumption of spherical particle shape. This simplifying assumption paves the ground for obtaining a fundamental understanding of the motion of almost neutrally buoyant particles in a magnetized fluid and provides a stepping stone towards studying more complex non-spherical particles. **Chapter 2** of this thesis addresses the magneto-Archimedes separation of spherical particles. A point-particle Euler-Lagrange (PP-DNS) model is presented which captures all the relevant fluid-particle and particle-particles interactions for spherical particles in MDS systems. We parameterize the motion of a single particle in a magnetized liquid and introduce the relevant particle-fluid-particle interaction mechanisms in the MDS of spherical particles. The performance of the numerical model is experimentally validated, and the influences of unsteady fluid-particle interactions and collisions on the motion of particles in MDS systems is illustrated.

The next step in achieving a more realistic model for the MDS process is to include the effect of particle non-sphericity. Particles in practical MDS applications are rigid flakes which can be mathematically approximated by low-aspect-ratio oblate spheroids. In PP-DNS simulations momentum transfer between particles and fluid is achieved via the point-force approximation [15, 33, 81]. PP-DNS models for hydrodynamic interactions of inertial spherical particles within and beyond the Stokes regime have been derived and are widely used. For non-spherical particles, however, models for these interactions are scarce. The complexity of these interactions for non-spherical particles is due to the increase in the number of influence parameters; challenges in capturing these shape-specific interactions increase as the particles anisotropy increases. **Chapter 3** addresses the derivation of shape-specific correlations for steady hydrodynamic interactions of thin oblate spheroids at low to moderate Reynolds numbers. We present a novel approach for deriving a model for force and torque coefficients of a 1:10 spheroid immersed in a viscous fluid. A data set consisting of orientation- and Reynolds number-dependent steady forces and torques on a 1:10 oblate spheroid is generated using resolved simulations. Next, a machine-learning technique is employed to derive models for coefficients of steady drag, lift and pitching torque on the particle.

In **Chapter 4** we extend the numerical framework presented in Chapter 2 to develop a model for magneto-Archimedes levitation of non-spherical particles. This extended numerical framework employs appropriate force and torque models for ellipsoidal par-

ticles to capture the rotational and translational motion of non-spherical particles in a magnetized fluid. New collision detection and response models are incorporated for particle-particle interactions of ellipsoids, and a new simple strategy for the two-way fluid-particle momentum exchange is presented. First, the model is tested against experimental observations and afterwards, it is applied to large MDS systems to quantify the effects of particle aspect ratio and collisions in MDS of non-spherical particles.

Finally, in **Chapter 5**, we summarize the concluding remarks and discuss recommendations for future research.

2. Buoyancy-driven motion of spherical particles in paramagnetic fluids

This chapter[1] presents an Euler-Lagrange approach for simulating magneto-Archimedes separation of almost neutrally buoyant spherical particles in the flow of a magnetized liquid.

2.1. Introduction

With the recent proliferation of single-life-cycle plastic products, efficient plastic recycling technologies play a crucial role in environmental and economic sustainability plans [54]. Most of the commonly used recycling methods include shredding mixtures of different types of plastics followed by a melting and pelletizing process that transforms the plastic waste into new lower value plastic products. To steer away from plastic downcycling, high-resolution plastic sorting systems are required which are capable of segregation of plastic waste into fractions, which are homogeneous with respect to type and colour. Mass-density-based mechanical separation methods such as the sink-float technique have been shown to be efficient for the separation of polyolefins from a plastic waste stream [128]. However, continuous one-step separation of multiple types of polymers can not be achieved by the conventional sink-float techniques. In contrast, magnetic density separation (MDS) is a promising high-resolution mass density-based separation technique which incorporates a magnetically responsive liquid and magnets to separate particles by means of magneto-Archimedes levitation [14, 88, 114, 156]. Besides end-of-life plastics, MDS has also successfully been applied to separate ores, non-magnetic metals [75, 129, 136] and toxic wastes [103]. The present work aims at modelling particle-laden flows in magnetic density separators to separate plastic particles of different mass densities.

Since the invention of ferrofluids in the 1960s [110], the feasibility of the application of magnetically responsive liquids in technology and medicine has raised the interest in magnetic liquids. A ferrofluid is a stable colloidal suspension of ferri- or ferromagnetic nanoparticles in a carrier liquid. Due to their magnetic properties, these liquids react to an external magnetic field. An external magnetic field gradient generates an additional body force that alters the pressure inside the liquid. Saturated molecular solutions of salts such as manganese(II) chloride have magnetic properties similar to ferrofluids. The Langevin paramagnetic susceptibility of such paramagnetic solutions is about five orders of magnitude lower than that of synthetic colloidal ferrofluids [19]. Therefore, to generate forces of the same order of magnitude, stronger magnetic fields are required. However, the advantageous property of such solutions compared to a

---

[1]This chapter is based on the article: "Direct numerical simulation of Magneto-Archimedes levitation of spherical particles". S. Tajfirooz, J.G. Meijer, R.A. Dellaert, A.M. Meulenbroek, J.C.H. Zeegers, & J.G.M. Kuerten (2021). *Journal of Fluid Mechanics*, 910, A52.

ferrofluid is their transparency, which allows optical measurement techniques such as particle tracking velocimetry. Liquid oxygen also exhibits magnetic behaviour similar paramagnetic to salt solutions. However, its application is limited as sustaining oxygen in liquid phase requires cryogenic temperatures [25].

Neuringer and Rosensweig were the firsts to establish the theory for the motion of magnetically polarizable fluids, *ferrohydrodynamics* [101]. The theory was initially based on the assumption of a single-phase magnetizable medium with the magnetization in equilibrium (quasi-equilibrium ferrohydrodynamics). Later, the effects of the non-equilibrium process of magnetic relaxation and the moment of ponderomotive forces were also included [118, 130]. In his book, Rosensweig addressed magnetic levitation of non-magnetic particles in a ferrofluid, a phenomenon he referred to as magnetic levitation of the first kind. Under the assumption of quasi-equilibrium fluid magnetization, he derived an expression for the magnetic buoyancy force acting on a small non-magnetic spherical particle immersed in a magnetic liquid [117].

Rosensweig's observation of magnetic levitation of a solid object inside a ferrofluid triggered the idea of mass density-based separation of materials through magneto-Archimedes levitation. Since then, papers have been published on magneto-Archimedes levitation of particles in paramagnetic and superparamagnetic liquids [3, 38, 39, 52, 74, 85, 96, 97, 157]. When a non-magnetic body immersed in a magnetic fluid is exposed to a non-uniform magnetic field, due to the non-linear pressure distribution inside the liquid, the buoyancy force acting on the body is dependent on the position of the particle. An immersed body tends to travel to the point where the vertical component of the total buoyancy force cancels the particle weight, making the vertical position of this equilibrium point dependent on the mass density of the body only. MDS exploits this principle to characterize subpopulations with different mass densities and separate them from mixtures.

MDS of end-of-life plastic is carried out by immersing a mixture of shredded plastic waste in a magnetically responsive liquid exposed to a magnetic field generated by properly designed magnets [14, 66, 88, 125]. A continuous separation process is achieved by generating a flow of magnetic liquid through the magnetic field. Magnets used in MDS are designed such that the magnitude of the induced magnetic field has a gradient perpendicular to the flow direction and parallel to the gravitational force. This will cause the immersed particles to be sorted in different mass density fractions which are levitated at different heights. Once a mixture of particles is injected into the flow at the upstream end of the channel, sorted fractions can be recovered by employing separator plates mounted at different heights at the downstream end. Incorporating two magnets located at the top and bottom of the system enables separation of particles both lighter and heavier than the carrier liquid. A schematic of a typical MDS system for separation of waste plastic is shown in figure 2.1.

Odenbach [103] addressed the possibilities and challenges in the commercial use of MDS. In the design of an MDS system, one has to consider not only the properties of the magnetic field and the magnetic liquid, but also the interaction of the dispersed particles with the magneto-fluidic system, and the inter-particle interactions. The particle separation time, defined as the time required for all particles to reach their corresponding equilibrium positions is an important MDS design parameter. The shorter the particle separation time, the shorter will be the time required for the particles to
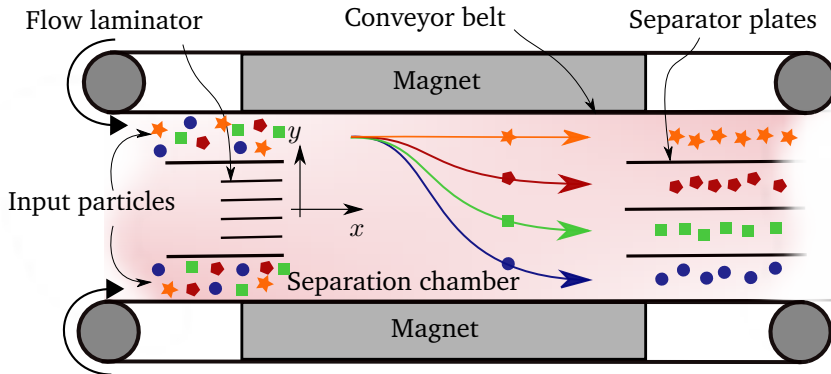
Figure 2.1.: A schematic of a magnetic density separator. Different markers (colours) represent different mass densities.

be exposed to the magnetic field. Decreasing the particle separation time can lead to an increase in the throughput of particles and therefore, an increase in the efficiency of an MDS system. The particle separation time is in turn dependent on several parameters such as the particle size and shape, the magnetic fluid viscosity and its magnetization, and the external magnetic field. At appreciable volume fractions, the particle separation time can be increased due to the inter-particle collisions.

The turbulence level in the separation channel is another crucial parameter in MDS [66]. Maintaining a low turbulence level in the separation channel is highly favourable, as turbulence level and mixing are intimately connected. A high turbulence level leads to an enhanced mixing, which can hamper the separation process. In new generations of MDS systems, measures have been taken to reduce the turbulence level in the separation chamber. These measures include the use of flow laminators such as honeycombs and screens at the upstream end of the separation channel and incorporation of moving walls [125]. The former decreases the upstream flow velocity fluctuations and vortices, and the latter aims to prevent the formation of boundary layers.

Design optimization of magnetic density separators requires a fundamental understanding of the collective motion of particles in a magnetic liquid. This requires the solution of many-particle problems that are coupled to a flow problem which is influenced by an external magnetic field. In this work, we present and employ a carefully chosen Euler-Lagrange approach to simulate the motion of particles in paramagnetic liquids.

Euler-Lagrange simulations are usually categorized into two families, which are particle-resolved simulations and point-particle simulations. Due to the prohibitively large computational resources required for particle-resolved simulations, we use a point-particle method, by incorporating appropriate models for forces and torques acting on the particles [80]. The feedback forces and torques from particle to fluid are treated by introducing local source terms to the time-dependent incompressible Navier-Stokes equation of the fluid, which is solved with a pseudo-spectral method. We combine the point-particle approach with experimental observations to investigate the particle dynamics in paramagnetic liquids. The dynamics of a single particle as it moves towards

its equilibrium position in a magnetic liquid is the basis for the behaviour of many-particle systems. A fundamental understanding of the motion of a single particle in a magnetic liquid is therefore crucial to understand the collective motion of particles in larger magneto-fluidic systems. Furthermore, the existence and stability of an equilibrium at which a particle is eventually levitated provides a useful framework for the investigation of particle motion in liquids within the Stokes regime (near the equilibrium point) and beyond it (further from the equilibrium) where advective inertial forces are important. The motion of spherical and non-spherical particles in non-magnetic fluids has been the subject of several numerical and experimental investigations, see for instance Jenny et al. [71], Horowitz and Williamson [65], Elghobashi and Truesdell [42], Ern et al. [43], but only a limited number of studies have addressed the dynamics of particles (drops) in magnetic liquids [55, 79, 143]. When a particle is allowed to move freely under the combined effect of the magnetic buoyancy force and gravity, new features can occur in the particle motion. Singh et al. [134] used a one-fluid numerical model to explore the centre of mass and interface dynamics of an almost neutrally buoyant droplet (mass density ratio of 1.15) levitating in a ferrofluid. By approximating the vertical motion of the droplet by a simple dynamical model, the authors showed that depending on the parameters of the considered magneto-fluidic setup, the behaviour of vertical droplet motion can be monotonic or oscillating.

In the present work, we combine experimental observations with numerical simulations to investigate the motion of rigid non-magnetic spherical particles within the particle-to-fluid mass density ratio range $[0.7, 1.3]$ in a paramagnetic liquid. Our numerical model employs a four-way coupled point-particle approach to represent both the fluid flow and the motion of the inertial particles. The aim of this paper is threefold. First, the 1D dynamics of a single spherical particle moving in a paramagnetic liquid exposed to a magnetic field gradient is addressed. Through *a priori* mathematical analysis, the nature of the motion of a single spherical particle in a paramagnetic liquid is parameterized. Solutions of the governing equation of the translational motion of a spherical particle in a paramagnetic liquid are compared to experimental observations. Second, the effect of collisions in two-particle systems is investigated. We validate our numerical model by comparison with results of particle tracking velocimetry (PTV) experiments in one- and two-particle systems. Finally, many-particle systems are numerically studied. Parametric studies are performed to investigate the effect of the incorporation of the Basset history force, two-way coupling and collisions in a practical MDS case. Next, the effect of particle size and initial particle distribution on the separation efficiency is investigated.

The rest of the paper is organized as follows. We introduce the mathematical model for the problem in section 2.2. With an introduction to the hydrodynamics of magnetically responsive liquids in section 2.3, we address the concept of apparent mass density and buoyancy force in magnetic liquids. Different elements of the model, including the magnetic field, magnetic liquid and the immersed particles are discussed. The numerical solution approach and the experimental setup are described in sections 2.3 and 2.4 respectively. In section 2.5 first, the vertical motion of an individual spherical particle in a magnetic liquid is parameterized. Next, the numerical results are validated against experimental observations in single- and two-particle systems. Finally, the separation performance of many-particle systems is investigated numerically. Concluding remarks and future directions are addressed in section 2.6.

2.2. Mathematical description

In this section, we present the mathematical model for the incompressible isothermal channel flow of a magnetically responsive fluid laden with spherical particles. The considered system consists of three elements: A magnetic liquid considered as a continuous phase which is described by an Eulerian approach, discrete particles which are described in a Lagrangian way, and a steady external magnetic field.

For the equation of motion of the magnetic liquid, we follow the quasi-equilibrium theory of Rosensweig [118], where fluid magnetization is assumed to be in local equilibrium with the magnetic field and $M \times H = 0$, where H is the magnetic field vector and M is the fluid magnetization vector. The particles are assumed to be rigid spheres which interact with each other through collisions. The discrete particles and the continuous phase are coupled by means of two-way momentum transfer. We first introduce the governing equations of motion of a paramagnetic liquid exposed to a magnetic field gradient in section 2.2.1. In section 2.2.2 the magnetic fields considered in this study are presented. Section 2.2.3 addresses the buoyancy force in magnetic liquids and introduces the concept of apparent mass density. The equations describing the motion of particles in a paramagnetic liquid are presented in section 2.2.4.

2.2.1. Continuous phase

The motion of a magnetically responsive fluid in a magnetic field is influenced by a Kelvin body force which arises from the interaction between the local magnetic field and the molecular magnetic moments characterized by the fluid magnetization. This force is in addition to the gravitational body force acting on the fluid. Under the assumption of equilibrium magnetization, the governing equations of the incompressible flow of a Newtonian magnetically responsive fluid can be written as [118]

$$\rho_{\mathrm{f}} \left(\frac{\partial \boldsymbol{u}}{\partial t} + (\boldsymbol{u} \cdot \boldsymbol{\nabla})\boldsymbol{u} \right) = -\boldsymbol{\nabla} p^* + \mu \nabla^2 \boldsymbol{u} + \mathfrak{F}^{\mathrm{inter}}, \tag{2.1}$$

$$\boldsymbol{\nabla} \cdot \boldsymbol{u} = 0, \tag{2.2}$$

where $\boldsymbol{u}$ denotes the fluid velocity, μ is the dynamic viscosity of the fluid, and ρ_{f} is the mass density of the fluid. p^* represents a reduced pressure which accounts for the effects of the gravitational and the magnetic body forces. With gravity acting in the direction of $-\boldsymbol{e}_y$, this reduced pressure is defined as

$$p^* = p - p_{\mathrm{static}} = p + \rho_{\mathrm{f}} g y - \mu_0 \int_0^H M dH, \tag{2.3}$$

where $M = |\boldsymbol{M}|$ is the magnitude of the fluid magnetization, $H = |\boldsymbol{H}|$ is the magnetic field strength, and μ_0 denotes the permeability of vacuum. The term $\mathfrak{F}^{\mathrm{inter}}$ in equation (2.1) is the fluid-particle coupling term which takes care of the momentum transfer from the discrete particles to the fluid.

The flow field is obtained by solving (2.1) and (2.2) in a cubic domain with dimensions $L_x \times L_y \times L_z$, where x, y, and z denote the stream-wise, wall-normal, and span-wise directions respectively.

The magnetic liquid considered in this study is an aqueous paramagnetic fluid ($MnCl_2$ salt solution) with a linear magnetization behavior. If we let χ denote the magnetic susceptibility of the liquid, the magnetization vector field is defined as

$$\boldsymbol{M} = \chi \boldsymbol{H}. \tag{2.4}$$

Both magnetic susceptibility and dynamic viscosity of paramagnetic salt solutions are dependent on concentration of the solution [9].

2.2.2. Magnetic field

In this work, we consider one-dimensional magnetic fields which are uniform in planes parallel to the surface of the magnet ($\frac{\partial H}{\partial x} = \frac{\partial H}{\partial z} = 0$), and decay exponentially with the vertical distance from the magnet surface. Such magnetic fields can be generated by incorporating a specially designed array of alternately rotating magnetic poles [113] [46] [132]. In the regions sufficiently far from the magnet edges, the generated magnetic field by such configurations closely follows

$$\boldsymbol{H} = H(y)\boldsymbol{e}_y. \tag{2.5}$$

For a magnet located at the bottom of the computational domain such that its upper surface is located at $y = -L$, the magnetic field strength reads

$$H(y) = H_0 e^{-\pi(L+y)/p}, \quad y \in [-L, \infty], \tag{2.6}$$

where H_0 is the magnetic field strength at the surface of the magnet, and p denotes the pole size. Expression (2.6) is the solution of the Maxwell equation on the strong side of an infinitely long Halbach array with continuously varying magnetization [59]. The reader is referred to Mallinson [90] for the derivation. If the magnet is located at the top of the computational domain with its lower (strong) surface at $y = +L$, the magnetic field strength follows

$$H(y) = H_0 e^{-\pi(L-y)/p}, \quad y \in [-\infty, L]. \tag{2.7}$$

In case two identical magnets are located at the top and bottom of the computational domain with their strong sides facing each other, the magnitude of the magnetic field is assumed to be a linear superposition of the magnetic fields corresponding to each magnet:

$$H(y) = H_0 \left(e^{-\pi(L+y)/p} + e^{-\pi(L-y)/p} \right), \quad y \in [-L, L]. \tag{2.8}$$

For the sake of simplicity, in section 3 we consider a one-magnet configuration with a magnetic field strength following (2.6). For simulations of many-particle systems discussed in Section 4, a two-magnet configuration with a magnetic field strength given by (4.26) is considered.
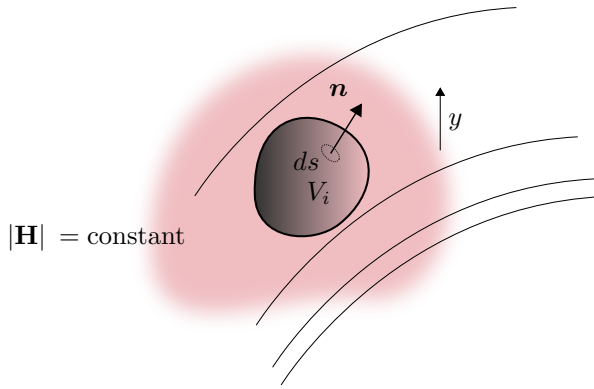
Figure 2.2.: A particle immersed in a magnetic liquid exposed to a magnetic field gradient.

2.2.3. Buoyancy in magnetic liquids

Let us now consider a situation when a non-magnetic body with volume V_i is immersed in a magnetic liquid exposed to an arbitrary magnetic field as shown in figure 2.2. The buoyancy force acting on the body can be calculated by applying the Gauss divergence theorem to the surface integral of the statice pressure at the interface s:

$$
\begin{aligned}
\boldsymbol{F}_{\mathrm{B}} &= -\int_s p_{\mathrm{static}}\boldsymbol{n}\mathrm{d}s = -\int_{V_i} \nabla p_{\mathrm{static}}\mathrm{d}V \\
&= \int_{V_i} (\rho_{\mathrm{f}} g \boldsymbol{e}_y - \mu_0 M \nabla H)\mathrm{d}V.
\end{aligned}
\tag{2.9}
$$

Under the assumption of a constant magnetic force within the volume of the immersed body (small body), the term $M\nabla H$ can be assumed to be constant within the volume V_i, and the buoyancy force can be approximated by:

$$
\boldsymbol{F}_{\mathrm{B},i} \approx \rho_{\mathrm{f}} V_i g \boldsymbol{e}_y - \mu_0 V_i M \nabla H.
\tag{2.10}
$$

The first term in (2.10) is the conventional gravitational buoyancy force (also known as the Archimedes force) which is constant throughout the liquid. The second term is the magnetic contribution to the buoyancy force we refer to as "magnetic buoyancy force". If the magnets are designed such that the magnetic field gradient is parallel to the gravitational force, the total buoyancy force reads

$$
\boldsymbol{F}_{\mathrm{B},i} \approx (\rho_{\mathrm{f}} g - \mu_0 M \frac{dH}{dy})V_i e_y.
\tag{2.11}
$$

The magnitude of the total buoyancy force acting on a body immersed in a magnetic liquid is dependent on the local gradient of the magnetic field and the magnetization of the liquid. We can combine the magnetic and the gravitational contributions and rewrite the buoyancy force in the form of the gravitational buoyancy force:

$$
\boldsymbol{F}_{\mathrm{B},i} = \rho_{\mathrm{f,a}} V_i g \boldsymbol{e}_y,
\tag{2.12}
$$

where

$$\rho_{\text{f,a}} \approx \rho_{\text{f}} - \left(\frac{\mu_0}{g} \right) M \frac{dH}{dy} \qquad (2.13)$$

is denoted as the "apparent fluid mass density".

If it exists, the equilibrium position of an immersed body, is the position where the magnitude of the buoyancy force is equal to the magnitude of the opposing gravitational body force acting on the body:

$$\boldsymbol{F}_{\text{B},i} + \boldsymbol{F}_{\text{G},i} = \rho_{\text{f,a}} V_i g \boldsymbol{e}_y - \rho_{\text{p}} V_i g \boldsymbol{e}_y = 0. \qquad (2.14)$$

At this position, the local apparent mass density of the fluid is equal to the mass density of the body. For a fixed magnetofluidic system, the equilibrium position of a body is only dependent on the mass density of the body. Therefore, by a careful adjustment of the magnetic field and the magnetic fluid properties, a gradient of apparent mass density can be generated wherein particles in a specific mass density range can be separated.

It should be noted that approximation (2.13) is based on the assumption that the term $M \frac{dH}{dy}$ is constant within the volume of a particle, which is only valid for a small particle size, or a small gradient of the magnetic field. An accurate expression for the apparent mass density of the magnetic liquid can directly be derived from the definition of the static pressure in (4.18):

$$p_{\text{static}} = -\rho_{\text{f}} g y + \mu_0 \int_0^H M dH = -\rho_{\text{f,a}}(y) g y, \qquad (2.15)$$

which gives

$$\rho_{\text{f,a}}(y) = \rho_{\text{f}} - \frac{\mu_0}{g y} \int_0^y M \frac{dH}{dy} dy. \qquad (2.16)$$

If the integral is taken over a small interval $y \approx d_{\text{p}}$, (3.18) reduces to the approximation (2.13).

The apparent mass density profile of a paramagnetic liquid exposed to a magnetic field of a bottom-magnet system given by (2.6) reads

$$\rho_{\text{f,a}} = \rho_{\text{f}} + \frac{\pi \mu_0 \chi H_0^2}{p g} e^{\frac{-2\pi(L+y)}{p}}. \qquad (2.17)$$

For a top-magnet configuration where the magnetic field follows (2.7) apparent fluid mass density is

$$\rho_{\text{f,a}} = \rho_{\text{f}} - \frac{\pi \mu_0 \chi H_0^2}{p g} e^{\frac{-2\pi(L-y)}{p}}, \qquad (2.18)$$

and for a two-magnet configuration with a magnetic field given by (4.26), the apparent mass density of the liquid reads

$$\rho_{\text{f,a}} = \rho_{\text{f}} - \frac{2\pi \mu_0 \chi H_0^2}{p g} e^{-\frac{2\pi L}{p}} \sinh(\frac{2\pi y}{p}). \qquad (2.19)$$

It follows directly from (2.17) and (2.18) that the maximum change in the apparent mass density of the fluid for a one-magnet system is

$$|\Delta\rho_{\text{f,a}}|_{\text{max}} = |\rho_{\text{f,a}} - \rho_{\text{f}}|_{\text{max}} = \frac{\pi\mu_0\chi H_0^2}{pg}, \qquad (2.20)$$

and from (2.19), for a two-magnet configuration

$$|\Delta\rho_{\text{f,a}}|_{\text{max}} = |\rho_{\text{f,a}} - \rho_{\text{f}}|_{\text{max}} = \frac{\pi\mu_0\chi H_0^2}{pg}|1 - e^{\frac{-4\pi L}{p}}|. \qquad (2.21)$$

The local gradient of the apparent mass density in the magnetic liquid is an indication of the separation resolution in an MDS system, as it determines the local separation distance of two consecutive mass density groups. The maximum gradient of apparent mass density for a one-magnet system is

$$\max\left(\frac{d\rho_{\text{f,a}}}{dy}\right) = \frac{2\pi^2\mu_0\chi H_0^2}{p^2 g}. \qquad (2.22)$$

For a two-magnet configuration, the maximum gradient of apparent mass density is

$$\max\left(\frac{d\rho_{\text{f,a}}}{dy}\right) = \frac{4\pi^2\mu_0\chi H_0^2}{p^2 g}\left(1 + e^{\frac{-4\pi L}{p}}\right). \qquad (2.23)$$

2.2.4. Particle phase

2.2.4.1. Equation of motion

The motion of rigid spherical particles immersed in a magnetically responsive liquid is described by solving the translational and rotational equations of motion for each particle where contributions from various fluid-solid interaction mechanisms are taken into account.

The translational motion of particles is based on an extension of the equation of motion derived by Maxey and Riley [94]. It is well known that for almost neutrally buoyant particles the contributions of the Basset history force, the added mass force, and the force due to the undisturbed velocity field to the motion of the particle cannot be neglected [80]. The included forces in the Maxey-Riley equation are the force due to the undisturbed velocity field, $F_{\text{U},i}$, steady viscous drag force, $F_{\text{D},i}$, added mass force, $F_{\text{AM},i}$, history force, $F_{\text{H},i}$, gravitational body force, $F_{\text{G},i}$, and the buoyancy force, $F_{\text{B},i}$.

For the drag coefficient, we consider the widely used correlation of Schiller and Naumann [123] for a non-creeping flow. The history force correction to the drag is based on the classic Basset kernel. Although, correlations for history force for non-creeping flows are derived [76], in this work we neglect the finite Reynolds number effects on the history kernel. The Faxén corrections for non-uniform flows and the lift force are not considered here as the background flow is assumed to be uniform.

The trajectory of each particle is obtained by solving the following set of differential equations:

$$\frac{d\boldsymbol{x}_i}{dt} = \boldsymbol{v}_i, \tag{2.24}$$

$$\frac{d\boldsymbol{v}_i}{dt} = \frac{1}{m_i}\left(\sum \boldsymbol{F}_i + \boldsymbol{F}_i^{(c)}\right), \tag{2.25}$$

with

$$\sum \boldsymbol{F}_i = \underbrace{\rho_{\mathrm{f}} V_i \frac{D\boldsymbol{u}_i}{Dt}}_{\boldsymbol{F}_{\mathrm{U},i}} + \underbrace{\rho_{\mathrm{p},i} V_i \frac{(\boldsymbol{u}_i - \boldsymbol{v}_i)}{\tau_{t,i}}\left(1 + 0.15 Re_{t,i}^{0.687}\right)}_{\boldsymbol{F}_{\mathrm{D},i}}$$

$$+ \underbrace{\frac{3}{2}\left(\pi \rho_{\mathrm{f}} \mu\right)^{1/2} d_{\mathrm{p}}^2 \left[\int_{-\infty}^{t} \frac{\frac{d}{d\tau}(\boldsymbol{u}_i - \boldsymbol{v}_i)}{(t - \tau)^{1/2}} d\tau\right]}_{\boldsymbol{F}_{\mathrm{H},i}} \tag{2.26}$$

$$+ \underbrace{\frac{1}{2}\rho_{\mathrm{f}} V_i \left(\frac{D\boldsymbol{u}_i}{Dt} - \frac{d\boldsymbol{v}_i}{dt}\right)}_{\boldsymbol{F}_{\mathrm{AM},i}} - \underbrace{\rho_{\mathrm{p},i} V_i g \boldsymbol{e}_y}_{\boldsymbol{F}_{\mathrm{G},i}} + \underbrace{\rho_{\mathrm{f},\mathrm{a}} V_i g \boldsymbol{e}_y}_{\boldsymbol{F}_{\mathrm{B},i}},$$

where $Re_{t,i} = d_{\mathrm{p}}|\boldsymbol{u}_i - \boldsymbol{v}_i|/\nu$ denotes the particle translational Reynolds number, $\boldsymbol{v}_i$ is the particle translational velocity, and $\boldsymbol{u}_i$ is the undisturbed fluid velocity at the position of the particle. $\tau_{t,i} = \rho_{\mathrm{p}} d_{\mathrm{p}}^2/18\mu$ is the particle translational relaxation time. $\boldsymbol{F}_i^{(c)}$ represents the force on a particle due to a collision with another particle or a wall.

Special care must be taken in evaluating the Basset history term when the relative particle-fluid velocity undergoes a step change. The derivation of the Basset history force is based on the assumption that the particle is present in the fluid at all times. The case where the particle initial velocity is not equal to the initial fluid velocity at the position of the particle is equivalent to the case where the particle is in a stagnant fluid for $t \in (-\infty, 0)$ and the fluid velocity undergoes a step change at $t = 0$ [76]. Under such circumstance the Basset integral can be written as

$$\int_{-\infty}^{t} \frac{\frac{d}{d\tau}(\boldsymbol{u}_i - \boldsymbol{v}_i)}{(t - \tau)^{1/2}} d\tau = \int_{t_s^+}^{t} \frac{\frac{d}{d\tau}(\boldsymbol{u}_i - \boldsymbol{v}_i)}{(t - \tau)^{1/2}} d\tau + \frac{\boldsymbol{u}_i(t_s^+) - \boldsymbol{v}_i(t_s^+) - \boldsymbol{u}_i(t_s^-) + \boldsymbol{v}_i(t_s^-)}{(t - t_s)^{1/2}}, \tag{2.27}$$

where $t_s = \max\{0, t_c\}$ is the time at which the step change occurs. A step change can occur in simulations with non-zero velocity difference between the particle and the fluid at $t = 0$, or during a particle-particle or particle-wall collision at $t = t_c$. The second term on the RHS of (2.27) is associated with such step changes in the particle-fluid relative velocity.

At a collision instance, t_c, the post-collision history integral can be written as

$$\int_{-\infty}^{t} \frac{\frac{d}{d\tau}(\boldsymbol{u}_i - \boldsymbol{v}_i)}{(t - \tau)^{1/2}} d\tau = \int_{t_c^+}^{t} \frac{\frac{d}{d\tau}(\boldsymbol{u}_i - \boldsymbol{v}_i)}{(t - \tau)^{1/2}} d\tau + \frac{\boldsymbol{u}_i(t_c^+) - \boldsymbol{v}_i(t_c^+) - \boldsymbol{u}_i(t_c^-) + \boldsymbol{v}_i(t_c^-)}{(t - t_c)^{1/2}}. \tag{2.28}$$

Under the assumption of an infinitesimally small collision duration, the fluid velocity remains constant; $\boldsymbol{u}_i(t_c^-) = \boldsymbol{u}_i(t_c^+)$. After each collision, the Basset integral (the pre-collision history) can be set to zero and the post-collision Basset history can be calculated as

$$F_h = \frac{3}{2}\left(\pi\rho_f\mu\right)^{1/2} d_i^2 \left[\int_{t_c}^t \frac{\frac{d}{d\tau}\left(\boldsymbol{u}_i - \boldsymbol{v}_i\right)}{(t-\tau)^{1/2}} d\tau + \frac{\boldsymbol{v}_i(t_c^-)) - \boldsymbol{v}_i(t_c^+)}{(t-t_c)^{1/2}} \right]. \qquad (2.29)$$

Inclusion of the Basset history force in (2.26) presents a numerical difficulty which mainly arises from the need to store the relative particle acceleration over the entire history of particle motion. Section 2.3 addresses the employed numerical approximation to overcome this difficulty.

The rotational motion of the dispersed phase is based on the theoretical equation of Dennis et al. [36] for the steady viscous torque against particle rotation. The angular velocity of the particles is obtained by solving

$$\frac{d\boldsymbol{\Omega}_i}{dt} = \frac{1}{I_i}\left(\boldsymbol{T}_i + \boldsymbol{T}_i^{(c)}\right), \qquad (2.30)$$

where

$$\boldsymbol{T}_i = -\, C_T \frac{1}{2}\rho_p \left(\frac{d_p}{2}\right)^5 \left|\frac{1}{2}\boldsymbol{\omega}_i - \boldsymbol{\Omega}_i\right| \left(\frac{1}{2}\boldsymbol{\omega}_i - \boldsymbol{\Omega}_i\right), \qquad (2.31)$$

with

$$C_T = \begin{cases} \frac{64\pi}{Re_{r,i}} & \text{if } Re_{r,i} \le 32, \\ \frac{12.9}{\sqrt{Re_{r,i}}} + \frac{128.4}{Re_{r,i}} & \text{if } 32 < Re_{r,i} < 1000, \end{cases} \qquad (2.32)$$

where $Re_{r,i} = d_p^2 \left|\frac{1}{2}\boldsymbol{\omega}_i - \boldsymbol{\Omega}_i\right| / \nu$ is the rotational Reynolds number, $\boldsymbol{\Omega}_i$ represents the particle angular velocity, $\boldsymbol{\omega}_i$ is the undisturbed fluid vorticity at the position of the particle, and $I_i = \frac{2}{5}m_i(d_p/2)^2$ is the moment of inertia. $\boldsymbol{T}_i^{(c)}$ is the torque on a particle due to a collision with a particle or a wall. It should be noted that in this chapter the torque coupling between the particles and the liquid is assumed to be one-way, *i.e* no feedback torque is imposed on the liquid.

2.2.4.2. Collisions

The inter-particle and particle-wall interactions are treated by a hard-sphere collision model which closely follows the method of Hoomans et al. [64]. The collision time is assumed to be infinitesimally small, and the pre- and post-collision translational and angular velocities are explicitly related through normal and tangential restitution coefficients and a dynamic friction factor. Consider two colliding particles with center position vectors $\boldsymbol{x}_a$ and $\boldsymbol{x}_b$, and contact point c. The normal unit vector at the contact point c is $\boldsymbol{n} = (\boldsymbol{x}_a - \boldsymbol{x}_b)/|\boldsymbol{x}_a - \boldsymbol{x}_b|$. If we let the superscripts $+$ and $-$ represent the post- and pre- collision properties respectively, the tangential unit vector at the contact point is $\boldsymbol{t} = \left(\boldsymbol{v}_{ab}^- - \boldsymbol{n}(\boldsymbol{v}_{ab}^- \cdot \boldsymbol{n})\right)/|\boldsymbol{v}_{ab}^- - \boldsymbol{n}(\boldsymbol{v}_{ab}^- \cdot \boldsymbol{n})|$, where $\boldsymbol{v}_{ab} = \boldsymbol{v}_{a,c} - \boldsymbol{v}_{b,c}$ is the particle relative velocity at the contact point. The post-collision translational and

rotational velocities can be derived according to the following equations:

$$m_a \left(\boldsymbol{v}_a^+ - \boldsymbol{v}_a^- \right) = -m_b \left(\boldsymbol{v}_b^- - \boldsymbol{v}_b^+ \right) = \boldsymbol{J},$$

$$\frac{I_a}{R_a} \left(\boldsymbol{\omega}_a^+ - \boldsymbol{\omega}_a^- \right) = \frac{I_b}{R_b} \left(\boldsymbol{\omega}_b^+ - \boldsymbol{\omega}_b^- \right) = -\boldsymbol{n} \times \boldsymbol{J}, \tag{2.33}$$

where $R = d_{\mathrm{p}}/2$ is the particle radius, m is the particle mass, and $\boldsymbol{J}$ is the impulse vector. The normal component of the impulse vector is given by

$$J_n = -(1 + e_{n,\mathrm{eff}}) m_{ab} \boldsymbol{v}_{ab}^- \cdot \boldsymbol{n}, \tag{2.34}$$

where $e_{n,\mathrm{eff}} = -\boldsymbol{v}_{ab}^- \cdot \boldsymbol{n} / \boldsymbol{v}_{ab}^+ \cdot \boldsymbol{n}$ denotes the effective coefficient of normal restitution, and m_{ab} is the reduced mass defined as $m_{ab} = m_a m_b / (m_a + m_b)$.

For the tangential component of the impulse vector a distinction can be made based on the type of collision being either "sticking" or "sliding":

$$J_t = \begin{cases} -\frac{2}{7} \left(1 + e_{t,\mathrm{eff}} \right) m_{ab} \boldsymbol{v}_{ab,0} \cdot \boldsymbol{t} & \text{if } \mu_f J_n \geq \frac{2}{7} \left(1 + e_{t,\mathrm{eff}} \right) m_{ab} \boldsymbol{v}_{ab,0} \cdot \boldsymbol{t} \text{ (stick)}, \\ -\mu_f J_n & \text{otherwise} \quad \text{(slide)}, \end{cases}$$

(2.35)

where $e_{t,\mathrm{eff}} = -\boldsymbol{v}_{ab}^- \cdot \boldsymbol{t} / \boldsymbol{v}_{ab}^+ \cdot \boldsymbol{t}$ is the effective coefficient of tangential restitution, and μ_{fric} is the coefficient of dynamic friction.

From the modeling viewpoint, appropriate values for the coefficients of restitution and friction coefficient are of great importance in the prediction of the post-collision dynamics. When inter-particle or particle-wall collisions occur in the absence of a viscous fluid (dry collisions), the kinetic energy of the particles is dissipated purely due to the contact mechanism. In a viscous fluid however, the collision process is influenced by the viscous and inertial interactions of the particle with the fluid. To account for the hydrodynamic effects of the surrounding fluid on the normal component of motion during a collision, an effective coefficient of normal restitution is introduced [34] [56]. The normal component of post-collision velocity of particles during a non-head-on collision follows the behavior of a head-on collision [153]. Regardless of the type of collision (oblique or head-on), the effective (wet) normal coefficient of restitution increases with the binary normal Stokes number defined as

$$\mathrm{St}_n = \frac{2}{9} \frac{\rho_{\mathrm{p}}^*}{\rho_{\mathrm{f}}} \mathrm{Re}_{\mathrm{rel}},$$

where $\rho_{\mathrm{p}}^* = (1/\rho_{\mathrm{p},1} + 1/\rho_{\mathrm{p},2})^{-1}$ is a reduced particle mass density, and $\mathrm{Re}_{\mathrm{rel}} = d_{\mathrm{p}} u_{\mathrm{p},n,\mathrm{rel}}/\nu$ denotes the relative Reynolds number based on the normal component of the particle relative velocity $u_{\mathrm{p},n,\mathrm{rel}}$. Izard et al. [67] proposed a model which can capture the experimentally observed effective coefficient of normal restitution for the range of Stokes number $0 < \mathrm{St}_n < 10^6$. This correlation relates the effective normal coefficient of restitution to the corresponding dry coefficient, the Stokes number, and the effective particle roughness height. For a particle-particle collision this correlation reads

$$\frac{e_{n,\mathrm{eff}}}{e_{n,\mathrm{dry}}} = \left(1 + \frac{1}{\mathrm{St}_n} \ln \left(\frac{2\eta_e}{d_{\mathrm{p}}} \right) \right) \exp \left(-\frac{\pi/2}{\sqrt{\mathrm{St}_n + \ln \left(\frac{2\eta_e}{d_{\mathrm{p}}} \right)}} \right), \tag{2.36}$$

where η_e is an effective average particle surface roughness height.

The qualitative behavior of immersed oblique collisions is similar to that of dry collisions. The effective values for coefficients of dynamic friction and tangential restitution depend on the considered fluid-particle system and the relative velocity of the particles [73]. According to Walton's hard-sphere model [151], the dynamic friction coefficient and the tangential coefficient of restitution can be obtained by plotting the tangent of rebound angle as a function of tangent of incidence angle. These two tangents are given by

$$
\begin{aligned}
\Psi_{\text{after}} &= \frac{(\boldsymbol{v}_{ab}^+ \cdot \boldsymbol{t})}{(\boldsymbol{v}_{ab}^- \cdot \boldsymbol{n})}, \\
\Psi_{\text{before}} &= \frac{(\boldsymbol{v}_{ab}^- \cdot \boldsymbol{t})}{(\boldsymbol{v}_{ab}^- \cdot \boldsymbol{n})}.
\end{aligned}
\tag{2.37}
$$

For the sticking collisions $\Psi_{\text{after}} = -e_{t,\text{eff}}\Psi_{\text{before}}$, and for sliding collisions $\Psi_{\text{after}} = \Psi_{\text{before}} - \frac{7}{2}\mu_{\text{eff}}(1 + e_{n,\text{eff}})$. In a similar manner, in section 2.5.2.2 we will determine the effective (lubricated) dynamic friction coefficient μ_{eff} and effective coefficient of tangential restitution, $e_{t,\text{eff}}$ by performing several particle-particle collision experiments at different incidence angles.

2.3. Numerical approach

2.3.1. Fluid phase

The flow field is obtained by reducing (2.1) and (2.2) to a fourth-order equation for wall-normal velocity component and a second-order equation for the wall-normal component of vorticity. The equations are discretized in space by using a pseudo-spectral method. Our method incorporates a Fourier-Galerkin approach in the periodic directions, x and z, and a Chebyshev-tau method in the wall-normal direction, y. The temporal discretization of the linear terms is carried out by a three-stage Runge Kutta scheme, and the non-linear terms are advanced in time by the Crank-Nicolson method. For details of the numerical approach, the reader is referred to Kuerten et al. [81].

2.3.2. Particle phase

2.3.2.1. Time integration

The equations of translational and rotational motion of spherical particles (2.24, 3.20, 2.30) are discretized in time using a forward Euler method. Our explicit scheme takes the partial time step of each stage of the Runge-Kutta scheme used for the fluid solver as a time step. In the numerical solution of system (2.26), integration of the Basset history term is the most time-consuming. To decrease the numerical costs of the evaluation of the Basset history contribution, we use the method of Van Hinsberg et al. [144] where a "window" is applied to the Basset kernel. The history kernel is split into a window kernel and a tail kernel. The window kernel (recent history)

is approximated by an ordinary trapezoidal rule over the interval $[t - t_{\mathrm{win}}, t]$ that consists of the N_{w} previous time steps. The tail kernel (old history) over the time interval $(-\infty, t - t_{\mathrm{win}})$ is approximated by a sum of exponential functions, leading to a considerable reduction in computational time as well as memory requirements.

2.3.3. Two-way coupling: Fluid-particle momentum transfer

The presence of particles in the fluid is represented by a local feedback force from the particles on the fluid defined as

$$\mathfrak{F}^{\mathrm{inter}}\left(\boldsymbol{x}\right) \equiv -\sum_{n=1}^{N_{\mathrm{p}}} \mathcal{P}\left(\boldsymbol{x} - \boldsymbol{x}_{\mathrm{p}}^{(n)}\right) \boldsymbol{F}_{2\mathrm{w}}^{(n)} \tag{2.38}$$

where N_{p} is the total number of particles and $\boldsymbol{F}_{2\mathrm{w}}^{(n)}$ is the feedback force from the nth particle modeled as

$$\boldsymbol{F}_{2\mathrm{w}}^{(n)} = \boldsymbol{F}_{\mathrm{U}} + \boldsymbol{F}_{\mathrm{D}} + \boldsymbol{F}_{\mathrm{H}} + \boldsymbol{F}_{\mathrm{AM}}. \tag{2.39}$$

In point-particle Euler-Lagrange simulations the term $\mathcal{P}\left(\boldsymbol{x} - \boldsymbol{x}_{\mathrm{p}}^{(n)}\right)$ is usually a numerical projection of the Dirac delta function from the particle center $\boldsymbol{x}_{\mathrm{p}}^{(n)}$ to the Eulerian grid point $\boldsymbol{x}$. A common approach to numerical projection $\mathcal{P}$ is to distribute the feedback force over the eight grid points surrounding the particle center using the same weights as for the interpolation of fluid properties to the position of the particle (point-force approach). In the limit of particles which are much smaller than the size of the Eulerian grid spacing, this approach is theoretically valid. However, as the particle size approaches the size of the grid spacing, the feedback force to the fluid momentum equation is spread over a volume. Since in our simulations the grid size can be smaller than the particle diameter d_{p}, we choose to distribute the particle feedback force over a volume approximately equal to the volume of the particle. A top-hat filter is implemented to distribute the feedback force from the Lagrangian particle position to the Eulerian grid points:

$$\mathcal{P}(\boldsymbol{x} - \boldsymbol{x}_{\mathrm{p}}) = \begin{cases} \dfrac{1}{\sigma_1 \sigma_2 \sigma_3}, & \text{if } |x_k - x_{\mathrm{p},k}| < \sigma_k/2 \ (k = 1, 2, 3), \\ 0, & \text{otherwise.} \end{cases} \tag{2.40}$$

The width of the filter σ_k, $k = 1, 2, 3$ is closest to the width of the particle encompassing cube in each direction. This means that the particle feedback force is distributed over a rectangular block with a volume closest to the volume of the smallest bounding box around the particle. This allows us to keep the feedback force distribution volume constant under mesh refinement. Furthermore, considering the fact that the grid spacing is not uniform in the wall-normal direction, the distribution volume is independent of the local grid spacing. Figure 2.3 shows a schematic of the applied filter for several particle positions.
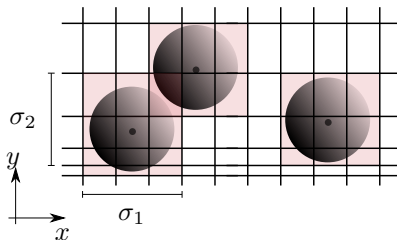
Figure 2.3.: A 2D schematic of the top-hat filter used to distribute the feedback force from the Eulerian particle position to the Eulerian grid points. σ_1 and σ_2 are widths of the filter in x- and y- directions respectively.

2.4. Experimental setup

We validate the results of our numerical approach with experimentally obtained particle tracks in single- and two-particle systems. For this purpose, an experimental setup is designed which enables the investigation of levitation motion of single spherical particles, as well as binary collision dynamics in a paramagnetic liquid subject to a magnetic field gradient. The paramagnetic liquid is synthesized by dissolving solid $\mathrm{MnCl_2}$ salt in distilled water up to the saturation point. The solution is afterwards filtered twice with filters of pore sizes 3 μm and 1 μm, and is stabilized by hydrochloric acid. The molality of the final aqueous solution is 4.62 mol/kg.

Measurements are performed in a $15 \times 15 \times 15$ cm^3 cubic tank. The particles can be inserted either at the top or through a hole at the bottom of the tank. A magnet is located underneath the tank to generate the desired magnetic field in the form of (2.6). The magnet is designed such that the induced magnetic field has a vertical gradient at the centre of the tank, where the measurements are performed. Two cameras are used to record the particle trajectories through two perpendicular sidewalls of the tank by means of 3D PTV. A schematic of the experimental setup is shown in figure 3.15 (a). The particles considered for the experiments are spherical unplasticized polytetrafluorethylene (PVC-U) and polyoxymethylene (POM) beads with mass densities $\rho_{\mathrm{p},1} = 1434$ kg/m^3, and $\rho_{\mathrm{p},2} = 1406$ kg/m^3, respectively. Some of the experimental parameters are summarized in table 3.2. Figure 3.15 (b) depicts the magnetic field strength on the vertical line passing through the centre of the tank, which is measured using a Gauss-meter. An exponential function of the form of (2.6) is fitted to the measured magnetic field strength profile to find the values of p and H_0, which are given in table 3.2.
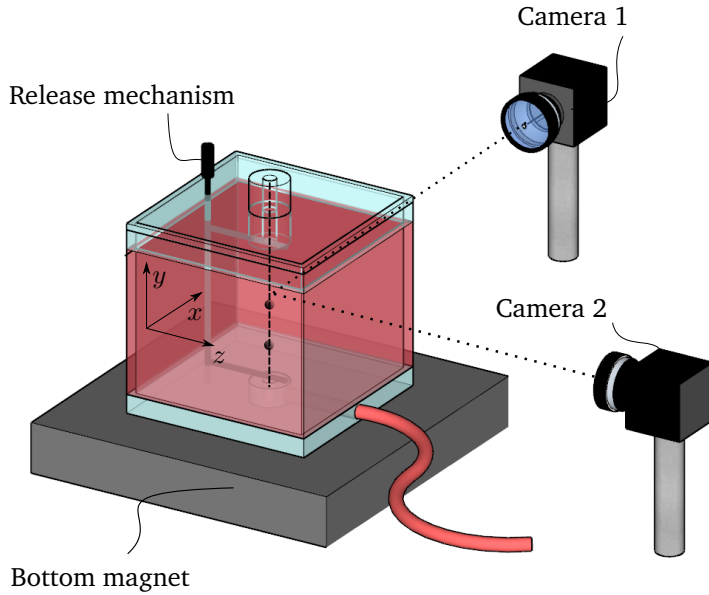
(a) Experimental setup
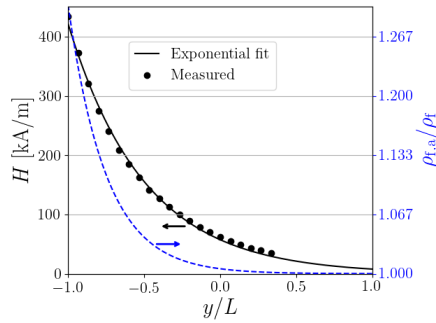
(b) Magnetic field strength and apparent mass density on a vertical line passing through the center of the tank

Figure 2.4.: (a) A sketch of the experimental setup. A tank filled with manganese(II) chloride solution is placed on top of a magnet. The particles are released by a rotating release mechanism. Two cameras record the motion of released particles. (b) Magnetic field strength on the vertical line at the centre of the tank (black symbols). The measured magnetic field strength is fitted to an exponential function of the form $H = H_0 e^{-\pi(L+y)/p}$ with $H_0 = 422$ kA/m and $p = 0.118$ m. The apparent mass density of the magnetic fluid with $\chi = 7 \times 10^{-4}$ is indicated by the blue dashed line. The corresponding vertical axes are indicated by the arrows. The magnetic susceptibility is calculated by measuring the magnetization of the liquid using a vibrating sample magnetometer (EZ-9 from Microsense), and computing the slope of the H-M curve. During the measurement, the magnetic liquid showed no hysteresis, which indicates the paramagnetic behaviour of the liquid.

$\rho_{\mathrm{p,1}}$ [kg/m^3]	1.434×10^3
$\rho_{\mathrm{p,2}}$ [kg/m^3]	1.406×10^3
ρ_{f} [kg/m^3]	1.403×10^3
μ_{f} [kg/m/s]	5.54×10^{-3}
χ_{f}	7×10^{-4}
L [m]	0.075
p [m]	0.1181
H_0[kA/m]	422

Table 2.1.: Properties of the experimental setup. The particles used for the experiments are spherical PVC-U (p$_1$) and POM (p$_2$) beads. The paramagnetic liquid is a saturated aqueous solution of $MnCl_2$ salt. The molal concentration of the synthesized solution is 4.62 mol/kg. The susceptibility of the paramagnetic liquid is calculated by measuring the magnetization of the solution, and the dynamic viscosity of the liquid is measured using a rheometer.

2.5. Results and discussion

In this section, we first present and discuss our results for single- and two-particle systems. In these systems, the particle-induced flow is neglected, and the equations of motion of the fluid are not solved, which is valid at the very low particle volume fraction of these simulations. In subsection 2.5.3, we address many-particle systems in which we do solve the fluid equations and also consider two-way momentum coupling between the fluid and particles.

2.5.1. The motion of a single particle immersed in a quiescent paramagnetic liquid

The buoyancy-driven motion of spherical particles in Newtonian fluids has been extensively studied. It is shown experimentally [65] and numerically [71] that the motion of a freely falling or ascending sphere under the action of gravity in a Newtonian fluid is fully characterized by two dimensionless numbers namely the particle relative mass density $\rho_{\mathrm{p}}/\rho_{\mathrm{f}}$, and the Galileo number $Ga = \sqrt{|1 - \rho_{\mathrm{p}}/\rho_{\mathrm{f}}|\, gd_{\mathrm{p}}^3}/\nu$. For a particle settling in a magnetic liquid an "apparent Galileo number" can be defined as $Ga_a = \sqrt{|1 - \rho_{\mathrm{p}}/\rho_{\mathrm{f,a}}|gd_{\mathrm{p}}^3}/\nu$. Unlike the settling of a particle in a non-magnetic liquid, for a particle traveling inside a magnetically responsive liquid in a direction parallel to the magnetic field gradient, the apparent Galileo number is not constant. This number is dependent on the local apparent mass density of the liquid and therefore on the position of the particle. The further away the position of the particle from its equilibrium point, the larger will be the apparent Galileo number. As the particle approaches its equilibrium position, the apparent Galileo number goes to zero. For the magnetofluidic systems considered in this study, the range of the apparent Galileo number is $0 \leq Ga_{rma} \leq 150$. Within this range, it is known that, regardless of the

particle mass density ratio, the particle trajectory is vertical and quasi-steady [71]. Therefore, we can assume that the motion of a single particle in a quiescent magnetic fluid exposed to a magnetic field with negligible horizontal gradients is in y-direction. Based on this assumption, the governing equation of motion of the particle can be reduced to a two-dimensional scalar non-linear system. In the following section we will investigate the solution behavior of such non-linear systems through a dynamical analysis.

2.5.1.1. Equilibrium position and nature of particle motion

In our analysis we make the following simplifying assumptions: Considering the fact that the fluid is at rest ($U_0 = 0$), we neglect the effect of fluid motion on the particle. Based on our earlier discussion, considering the range of apparent Galileo number and the 1D magnetic field, we can further assume that the particle does not undergo any rotational or lateral movement. Under these assumptions, (2.24) and (3.20) can be simplified to the following system of scalar equations:

$$\frac{dy}{dt} = v,$$
$$\frac{dv}{dt} = \frac{\rho_p}{\rho_p + 0.5\rho_f}\left[-\frac{\left(1 + 0.15Re_p^{0.687}\right)}{\tau_{t,i}}v - \frac{3}{2}\left(\pi\rho_f\mu\right)^{1/2}d_i^2\int_0^t\frac{1}{(t-\tau)^{1/2}}\frac{dv}{d\tau}d\tau \quad (2.41)$$
$$+ \left(\frac{\rho_{f,a}}{\rho_p} - 1\right)g\right].$$

System (2.41) is a non-autonomous system of two first-order nonlinear differential equations. The time-dependency stems from the Basset history contribution.

For brevity we present our analysis for a bottom-magnet configuration where the fluid apparent mass density follows (2.6). For such a configuration System (2.41) can be written in matrix notation as

$$\dot{\boldsymbol{Y}} = \frac{d\boldsymbol{Y}}{dt} = \boldsymbol{F}(\boldsymbol{Y}, t), \quad (2.42)$$

where

$$\boldsymbol{Y} = \begin{pmatrix} y \\ v \end{pmatrix} \quad (2.43)$$

and

$$\boldsymbol{F}(\boldsymbol{Y}, t) = \begin{pmatrix} v \\ \alpha\xi v + \eta\xi + \beta\xi e^{\theta y} + \alpha\epsilon\xi v|v|^{0.687} + \zeta\xi\int_0^t\frac{1}{(t-\tau)^{1/2}}\frac{dv}{d\tau}d\tau \end{pmatrix} \quad (2.44)$$

with

$$\alpha = -\frac{1}{\tau_t}, \quad \eta = \left(\frac{\rho_f}{\rho_p} - 1\right)g, \quad \beta = \frac{2\pi\mu_0\chi H_0^2}{pg\rho_p}e^{-2\pi L/p}, \quad \theta = -\frac{2\pi}{p},$$
$$\epsilon = -0.15(\frac{d_p}{\nu})^{0.687}, \quad \zeta = -1.5\left(\pi\rho_f\mu\right)^{1/2}d_p^2, \quad \xi = \frac{\rho_p}{\rho_p + 0.5\rho_f}.$$

By setting $\dot{\boldsymbol{Y}} = (0,0)^T$ and $t \to \infty$, the history integral term tends to zero as $t \to \infty$ and the equilibrium point of the system reads

$$\boldsymbol{Y}_e = \begin{pmatrix} y_e \\ 0 \end{pmatrix} = \begin{pmatrix} \frac{1}{\theta} \ln(\frac{-\eta}{\beta}) \\ 0 \end{pmatrix}, \tag{2.45}$$

where y_e corresponds to the equilibrium position of the particle in the magnetic liquid. Considering the fact that $\beta > 0$, an equilibrium point exists only if $\eta < 0$ i.e. $\frac{\rho_f}{\rho_p} \leq 1$. This implies that a bottom-magnet configuration is only capable of levitating particles which are heavier than the magnetic liquid. Particles which are lighter will eventually float on top of the liquid.

Given the initial position and velocity of the particle, a numerical approximation of system (2.42) can be solved to find the vertical position and velocity of the particle as functions of time. It is, however, useful to obtain a qualitative understanding of the behavior of a particle near its equilibrium point, before solving the system. If we assume that the history force is negligible compared to the other forces acting on the particle, system (2.42) can be converted to an autonomous system of the form

$$\dot{\boldsymbol{Y}} = \frac{d\boldsymbol{Y}}{dt} = \boldsymbol{G}(\boldsymbol{Y}), \tag{2.46}$$

where

$$\boldsymbol{G}(\boldsymbol{Y}) = \begin{pmatrix} v \\ \alpha\xi v + \eta\xi + \beta\xi e^{\theta y} + \alpha\epsilon\xi v |v|^{0.687} \end{pmatrix}. \tag{2.47}$$

Without losing generality we can shift the equilibrium point of the system to the origin by making the substitution $\tilde{\boldsymbol{Y}} = \boldsymbol{Y} - \boldsymbol{Y}_e$. Near the equilibrium point, $\tilde{\boldsymbol{Y}} \to (0,0)^T$. Therefore, system (2.47) can be approximated by the linear system

$$\dot{\tilde{\boldsymbol{Y}}} = \mathbf{J}\tilde{\boldsymbol{Y}}, \tag{2.48}$$

where the Jacobian matrix $\mathbf{J}$ is

$$\mathbf{J} = \begin{pmatrix} 0 & 1 \\ \beta\theta\xi e^{\theta y_e} & \alpha\xi \end{pmatrix} = \begin{pmatrix} 0 & 1 \\ -\eta\theta\xi & \alpha\xi \end{pmatrix}. \tag{2.49}$$

The stability and type of the critical point of the system (2.48) are determined by eigenvalues of the matrix $\mathbf{J}$, $\lambda_{1,2} = \alpha\xi/2 \pm \left(\alpha^2\xi^2/4 - \eta\theta\xi\right)^{0.5}$. It can be shown that except for the special case where $\alpha^2/4 = \eta\theta$, the stability and type of the critical point are not affected by the non-linear terms in the system (2.46). Therefore the behavior of the solution of non-linear system (2.46) can be determined by studying the much simpler linear system (2.48). In case of an existing equilibrium point, considering the fact that $\alpha\xi < 0$ and $\eta\theta\xi > 0$, the eigenvalues are either negative real numbers or complex numbers with a negative real part. Therefore the solution of the system is always asymptotically stable. The behavior of the solutions is dependent on the sign of $(\alpha^2\xi^2/4 - \eta\theta\xi)$. If $\alpha\xi/2 > \sqrt{\eta\theta\xi}$, the eigenvalues are real and the equilibrium point is an asymptotically stable *node*. The particle, in this case, monotonically moves

Configuration	y_e	$d_{\mathrm{p,crit}}$
Top-magnet	$\frac{p}{2\pi}\ln\left(\frac{(\rho_f-\rho_p)pg}{2\pi\mu_0\chi H_0^2}\right)$	$\left[\frac{81\mu^2 p}{\pi(\rho_p-\rho_f)(2\rho_p+\rho_f)g}\right]^{0.25}$
Bottom-magnet	$-\frac{p}{2\pi}\ln\left(\frac{(\rho_p-\rho_f)pg}{2\pi\mu_0\chi H_0^2}\right)$	$\left[\frac{81\mu^2 p}{\pi(\rho_f-\rho_p)(2\rho_p+\rho_f)g}\right]^{0.25}$
Two-magnet	$-\frac{p}{2\pi}\sinh^{-1}\left(\frac{(\rho_p-\rho_f)pg}{4\pi\mu_0\chi H_0^2}\right)$	$\left[\frac{162g\mu^2 p^2 e^{\frac{2\pi L}{p}}}{\pi\sqrt{16\pi^2\mu_0^2 M_0^2 H_0^2+g^4 p^2(\rho_f-\rho_p)^2 e^{\frac{4\pi L}{p}}}(\rho_f+2\rho_p)}\right]^{0.25}$

Table 2.2.: Particle equilibrium position and critical particle diameter for top-, bottom-, and two-magnet configurations with magnetic fields following (2.7), (2.6), and (4.26) respectively.

towards its equilibrium point. On the other hand, for $\alpha\xi/2 < \sqrt{\eta\theta\xi}$ the eigenvalues are complex numbers. The equilibrium point, in this case, is a *spiral point*; The particle exhibits an oscillatory motion around the equilibrium point while it approaches it. For a fixed magnetofluidic configuration a critical particle diameter can be found above which oscillatory behavior occurs. This critical diameter for a single-magnet configuration, regardless of the magnet position is

$$d_{\mathrm{p,crit}} = \left[\frac{81\mu^2 p}{\pi\left(\rho_p - \rho_f\right)\left(2\rho_p + \rho_f\right)g}\right]^{0.25} \tag{2.50}$$

A similar analysis can be performed for top-magnet and two-magnet configurations with magnetic fields described by (2.7) and (4.26), respectively. The results are summarized in table 2.2. It is notable that for one-magnet configurations the particle behavior is dependent on three parameters only, namely α, η, and θ. For two-magnet systems the nature of particle motion is also dependent on the parameter β which contains the magnetic field strength, H_0.

To illustrate the dependency of particle dynamics on its diameter, we consider the bottom-magnet configuration presented in section 2.4 with parameters given in table 3.2. In such configuration, the equilibrium position of a particle with a mass density $\rho_p = 1.434 \times 10^3$ kg/m^3 is $y_e = -0.35L$. The corresponding critical diameter is $d_{\mathrm{p,crit}} = 3.2$ mm. To obtain the particle vertical position as a function of time, system (2.46) is solved by an explicit Euler method.

Figure 2.5 compares the time evolution of the vertical position of four particles with diameters of 1, 2, 4, and 6 mm obtained by solving system (2.46) with the same initial condition, $Y_0 = (-0.9L, 0)^T$. The transition from monotonic to oscillatory motion can be observed by comparing the results of the 2- and 4-mm particles.

The effect of particle size on the nature of particle motion can be further illustrated by exploring the phase portraits and direction fields associated with solutions of system (2.46). Figure 2.6 compares the direction fields and phase portraits of solutions of this system obtained with combinations of three different initial positions, and three different initial velocities for $d = 2$ mm (a) and $d = 6$ mm (b). Regardless of the initial condition, a 2-mm particle moves monotonically towards its equilibrium position, whereas a 6-mm particle exhibits a spiraling behavior. Due to the larger magnetic buoyancy force, a 6-mm particle gains larger velocity and overshoots the equilibrium
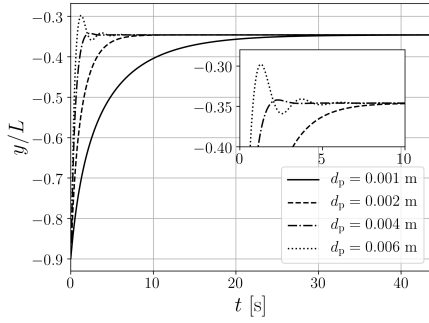
(a) Vertical position versus time
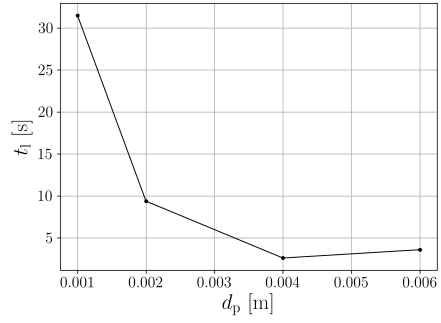
(b) Levitation time versus particle diameter

Figure 2.5.: Effect of particle size on levitation dynamics. (a) Time plots of particle vertical position for 1-, 2-, 4-, and 6-mm particles. (b) Particle levitation time as a function of particle diameter. The particle critical diamter is $d_{\mathrm{p,crit}} = 3.2$.

point.

We study the effect of particle size on the temporal evolution of particle position by comparing the time it takes for particles with different sizes to reach to their equilibrium position. If we let $\{t_{l,i}\}$ denote a set containing roots of the equation $|y(t) - y_{\mathrm{eq}}| = \mathrm{tol}$, with tol denoting a considered tolerance, a particle levitation time can be defined as $t_{\mathrm{l}} = \max\{t_{l,i}\}$. The effect of particle diameter on levitation time is illustrated in 2.5 (b), where particle levitation time t_l is plotted versus the particle diameter. All the reported levitation times are computed with a tolerance of $\mathrm{tol} = 0.5$ mm. In figure 2.5 (b) particle levitation time is plotted against the particle diameter. It can be clearly seen that increasing the particle size leads to an initial rapid decrease in the levitation time. The levitation time reaches a minimum at around $d_{\mathrm{p}}, = 0.0045$ m, and starts to increase afterward. This behavior is due to the increased amplitude of oscillations around the equilibrium height at higher particle diameters.

2.5.1.2. History Effects

In the previous analysis effects stemming from the Basset history force are neglected. However, it is known that the history force can be large at high particle acceleration rates. Therefore, in this section we investigate the effect of Basset history force on particle motion. Figure 2.7 compares the temporal evolution of position and velocity of a particle with $d_{\mathrm{p}} = 2$ mm and $\rho_{\mathrm{p}} = 1.434 \times 10^3$ kg/m^3 with initial condition $Y_0 = (-0.9L, 0)^T$ over time interval $[0, t_{\max} = 13.11]$ s with and without Basset history force. A window size of $t_w = 0.1t_{\max}$ is considered for the computation of the history kernel.

For the 2-mm particle, the history force leads to a slight decrease in the initial acceleration followed by a decrease in the deceleration of the particle as it approaches its equilibrium position. Initially the history force slows down the particle as it introduces

(a) $d_p = 2$ mm

(b) $d_p = 6$ mm
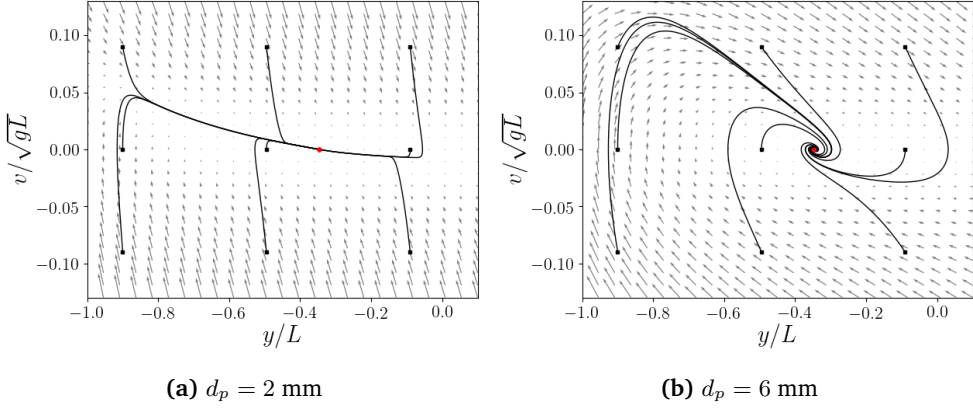
Figure 2.6.: Direction field and phase portraits for the solutions of system (2.46) with nine different initial conditions (black circles). The critical point of the system is $\boldsymbol{Y}_e = (0, -0.35L)^T$ (red circle). The critical diameter for the considered parameters is $d_{\mathrm{p,crit}} = 3.2$ mm. (a) $d_p = 2$ mm: The critical point is a node. (b) $d_p = 6$ mm: The critical point is a spiral point.

(a) Vertical position

(b) Vertical velocity
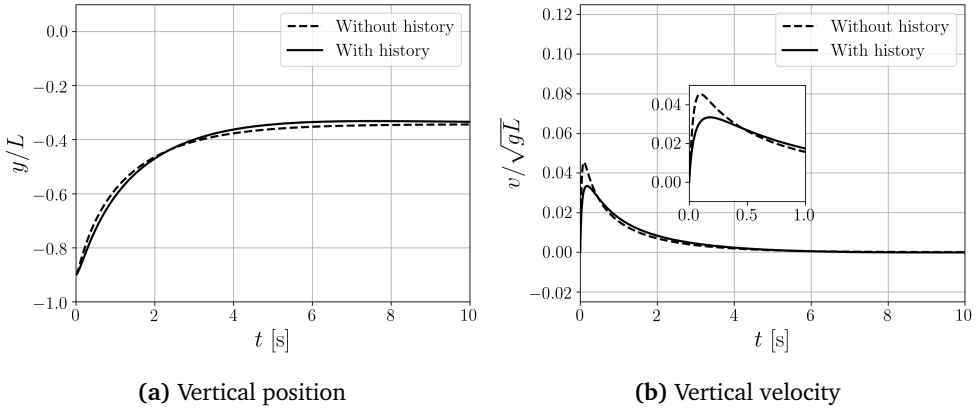
Figure 2.7.: Comparison of the solutions of autonomous system (2.46) and non-autonomous system (2.42) with initial condition $\boldsymbol{Y}_0 = (-0.9L, 0)^T$. The particle diameter is $d_{\mathrm{p}} = 2$ mm.

(a) Vertical position

(b) Vertical velocity
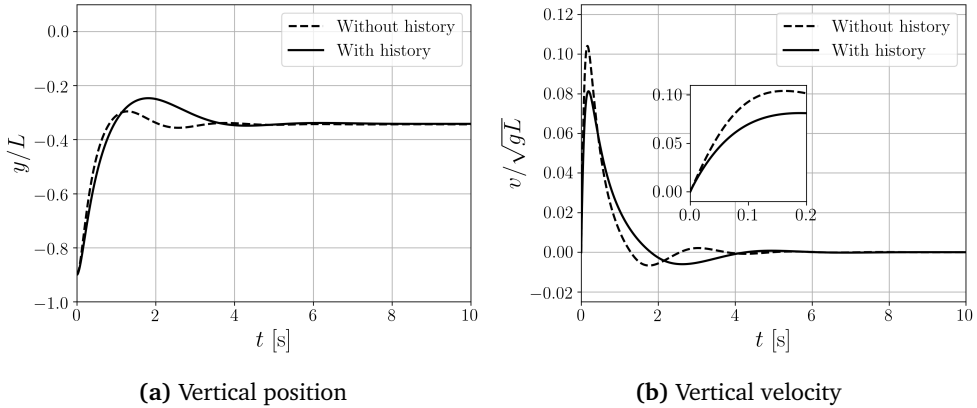
Figure 2.8.: Comparison of the solutions of the autonomous system (2.46) and the non-autonomous system (2.42) with initial condition $\boldsymbol{Y}_0 = (-0.9L, 0)^T$. The particle diameter is $d_{\mathrm{p}} = 6$ mm.

extra damping to the system. As the particle gets closer to the equilibrium point the moving fluid drags the particle and reduces deceleration.

The effect of Basset history force on the motion of a larger particle is shown in figure 2.8 where the particle diameter is increased to 6 mm. Although the history effects do not alter the oscillatory nature of the particle motion, it can be observed that the history force leads to an amplified overshoot near the equilibrium point. This can be interpreted as follows. As the particle approaches its equilibrium position, due to history effects the moving fluid pushes the particle further away from the equilibrium point leading to a larger overshoot. However, the damping introduced by history effects decreases the particle oscillations.

The contribution of the Basset history force to the motion of a particle is further illustrated in figure 2.9, where different hydrodynamic forces acting on the particle are compared for $d_{\mathrm{p}} = 2$ and 6 mm. Note that the forces are normalized by the gravitational force. We observe that for both particle sizes, the added mass force has the smallest relative contribution to the particle motion. For the larger particle, the maximum absolute values for normalized steady drag and Basset history forces are smaller and are attained later. This explains the higher acceleration of the 6-mm particle. Thanks to particle's higher inertia, for the 6-mm particle the relative contribution of the Basset history force is larger compared to the steady drag force. Moreover, for a larger particle, the history force has an appreciable contribution over a larger fraction of the levitation time.

2.5.2. Experimental validation of the mathematical model

In this section, we compare the solutions of systems (2.42) and (2.46) with experimental observations. First, we test our mathematical model against single-particle levitation experiments. Next, we consider two-particle systems where the effect of
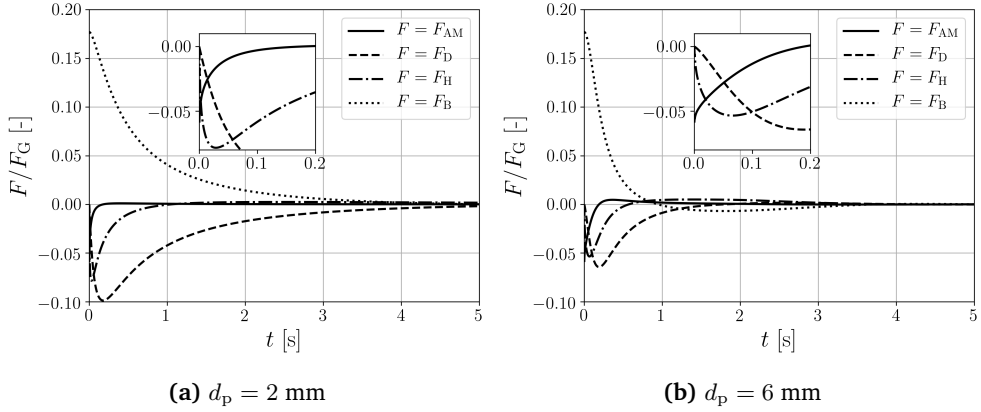
Figure 2.9.: Temporal evolution of the added mass, static drag, Basset history, and buoyancy force normalized by the gravitational force during the motion of a spherical particle with (a) $d_{\mathrm{p}} = 2\,\mathrm{mm}$ and (b) $d_{\mathrm{p}} = 6\,\mathrm{mm}$

collisions is investigated.

2.5.2.1. Single particle systems

For the singe-particle measurements, we consider two PVC-U spherical particles with diameters $d_{\mathrm{p}} = 3$ and $d_{\mathrm{p}} = 5$ mm, and mass density $\rho_{\mathrm{p},1}$. The other problem parameters are kept identical to those given in table 3.2. It was shown numerically in section 2.5.1.2 that neglecting the history effects introduces an error which increases at larger particle sizes. In order to validate this, we compare the experimental recordings of particle vertical position with the results of the numerical simulations obtained with the same initial conditions.

For each particle two sets of experiments are performed, a sinking and a rising experiment. The equilibrium height of the considered PVC-U particles is $y_e = -0.35L$. For the sinking case the particle is released at the top, and for the rising case the particle is released at the bottom of the tank. Figure 2.10 compares the numerical solution of system (2.42) which includes the Basset history force, to that of reduced autonomous system (2.46), and the experimental vertical position of the particles. Each experiment is repeated six times and the results are averaged. The error bars correspond to the standard deviation of these six measurements. The considered history window size for the simulations is $t_{\mathrm{win}} = 0.2$ s. The larger error bars in the experimental results of the 3-mm particle are due to the fact that the slower motion of smaller particles is relatively more sensitive to small disturbances in the flow. A very good agreement is observed between the numerical results with Basset history force and the experimental recordings. The larger contribution of history force to particle motion at larger diameters can be observed by comparing the plots of the 3- and 5-mm particles. It can clearly be seen from figure 2.10 (c) that exclusion of Basset history force leads a to 35% underestimation of the settling time for the falling 5-mm particle (6.22 s versus

(a) Falling 3-mm particle

(b) Rising 3-mm particle

(c) Falling 5-mm particle

(d) Rising 5-mm particle
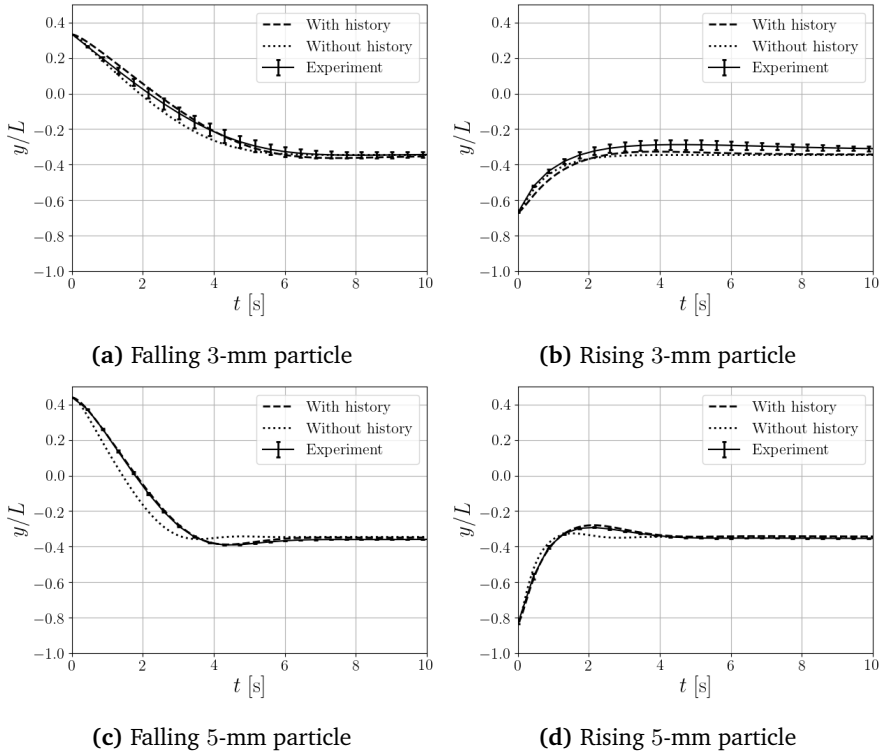
Figure 2.10.: Vertical position of 3- and 5-mm PVC-U particles. The dashed curves correspond to numerical solutions of system (2.42). The dotted lines indicate the particle position obtained form solving reduced system (2.46) and the solid curve corresponds to the experiments.

4.00 s). For the rising 5-mm particle (figure 2.10 (d)) an underestimation as high as 47% is observed (4.98 s versus 2.65 s). These observations prove that system (2.42) can very well describe the vertical motion of a single spherical particle, and that the contribution of Basset history force is crucial for accurate prediction of the motion of single particles in a paramagnetic liquid at larger diameters. The numerical results presented in the rest of the paper are obtained by the numerical model which includes the Basset history force, unless stated otherwise.

2.5.2.2. Effect of collisions: two-particle systems

In a many-particle MDS system, a particle can undergo multiple collisions as it moves towards its equilibrium position. Collisions are expected to hamper the motion of the particle and therefore delay the separation. In this Section, we first present the experimental procedure for obtaining the effective coefficients of friction and tangential restitution. Next, we test our hard-sphere model by comparing the results of numerical simulations with experimental observations in two-particle systems.
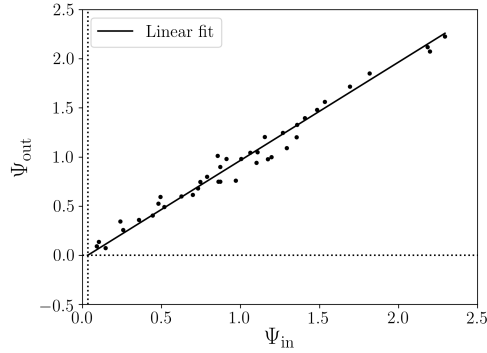
Figure 2.11.: The tangent of rebound angle as a function of the tangent of incident angle for a 5-mm PVC particle colliding with a 5-mm POM particle. Each point represents one collision experiment.

Experimentally, collisions are obtained by releasing two properly selected particles simultaneously from the top and bottom of the tank. The considered particles for the experiments are a 5-mm PVC-U particle with mass density $\rho_{p,1}$ (the sinking particle), and a 5-mm POM particle with mass density $\rho_{p,2}$ (the rising particle). Depending on the offset between the center of the particles, the lateral center distance (LCD), collisions can range from "head-on" to "grazing". We define an impact factor as $\mathcal{I} = \frac{\text{LCD}}{d_p}$, where for $\mathcal{I} = 0$ a collision is head-on and $\mathcal{I} = 1$ corresponds to a grazing collision.

Yang and Hunt [153] found that lubricated contact during collisions with low binary Stokes numbers reduces the dependence of rebound motion on the tangential particle-particle interactions. The dominating hydrodynamic effects of the interstitial fluid on the tangential component of motion during a collision can be captured by incorporating an effective (lubricated) friction coefficient. The two remaining effective collision parameters are obtained by investigating the tangents of incident and rebound at various particle-particle collisions. The binary normal Stokes number for the considered collisions are in the range $0 < \text{St}_n \leq 14$. Considering the zero pre-collision angular velocity and the small particle rotational relaxation time, the angular velocities remain almost zero after the collision. The tangent of rebound is therefore purely based on the translational particle velocity. In figure 2.11 the tangent of rebound angle for 40 different collisions is plotted against the tangent of incident angle. The positive values of ψ_{out} indicate the absence of the sticking regime. This reduces the number of required collision parameters to two, as the tangential restitution coefficient is only needed for capturing sticking collisions. The lubricated friction coefficient, μ_{eff} is found by fitting the line $\psi_{\text{out}} = \psi_{\text{in}} - \frac{7}{2}(1 + e_{n,\text{eff}})\mu_{\text{eff}}$ to the data, where $e_{n,\text{eff}}$ is calculated by (2.36) with $e_{n,\text{dry}} = 0.86$ and $\eta_e = 1.5$ μm. Depending on the value of $e_{n,\text{eff}}$, the lubricated friction coefficient ranges from $\mu_{\text{eff}} = 0.004$ to $\mu_{\text{eff}} = 0.008$. We use an average value of $\mu_{\text{eff}} = 0.005$ in our collision model.

Figure 2.12 compares the vertical position of the particles versus time, obtained from numerical simulations and experimental recordings for three collisions with impact factors $\mathcal{I} = 0.02$, $\mathcal{I} = 0.41$, and $\mathcal{I} = 0.78$. The numerical results are performed with a

Table 2.3.: Parameters used for the many-particle simulations

ρ_f [kg/m^3]	1.4×10^3
μ_f [kg/m/s]	5.54×10^{-3}
χ_f	7×10^{-4}
L [m]	0.075
p [m]	0.2
H_0[kA/m]	637

one-way coupled model using the same initial positions and velocities as in the experiments. To facilitate the comparison, the numerical results are slightly shifted in time to match the numerically and experimentally obtained collision times. A remarkably good agreement is observed between the numerically and experimentally obtained vertical positions of the particles as functions of time. The maximum increase in the levitation time is caused by the collision with $\mathcal{I} = 0.02$. This collision leads to about 15% and 45% increase in the levitation time of the sinking and rising particle respectively (based on experiments).

The horizontal motion of the particles can be seen in movies 1, 2 and 3, which can be found in the online version of the manuscript. In contrast to the vertical direction, some discrepancies are observed between the numerically and experimentally obtained results. These discrepancies are due to the magnetic field non-uniformities in off-centre regions of the experimental setup. The gradient of the magnetic field strength is vertical only in the central region of the tank. Hence, the assumption of vertical magnetic buoyancy force is only valid in this central region. Once particles undergo a collision, they enter regions where the magnetic buoyancy force is not vertical. In these regions, the horizontal gradient in the magnetic field strength pushes the particles back to the centre of the tank. This results in deviations from the numerically obtained post-collision horizontal motion of the particles.

2.5.3. Many-particle systems

In section 2.5.2, we validated our numerical model by comparison with experimental measurements of single- and two-particle systems. In this section, we present the results of the application of this numerical model to many-particle systems. We assume a uniform initial flow field with no disturbances. Particle-induced flow disturbances are taken into account by considering two-way momentum transfer between the fluid and the discrete spherical particles as described in section 2.3.3. A two-magnet configuration is considered where levitation of particles both lighter and heavier than the carrier liquid is possible. The magnetic field is described by (4.26). The computational domain has dimensions $L_x = 4\pi L/3$, $L_y = 2L$, and $L_z = 4\pi L/3$ as depicted in figure 2.13. The properties of the configuration are summarized in table 4.2.

As mentioned in section 2.1, in most recent MDS systems conveyor belts are installed at the top and bottom of the channel. These conveyor belts move with the same speed as the mean streamwise velocity U_0. This circumvents the formation of boundary layers and transition to turbulence near the walls. For such flow configurations, it is

(a) $\mathcal{I} = 0.02$

(b) $\mathcal{I} = 0.41$

(c) $\mathcal{I} = 0.78$
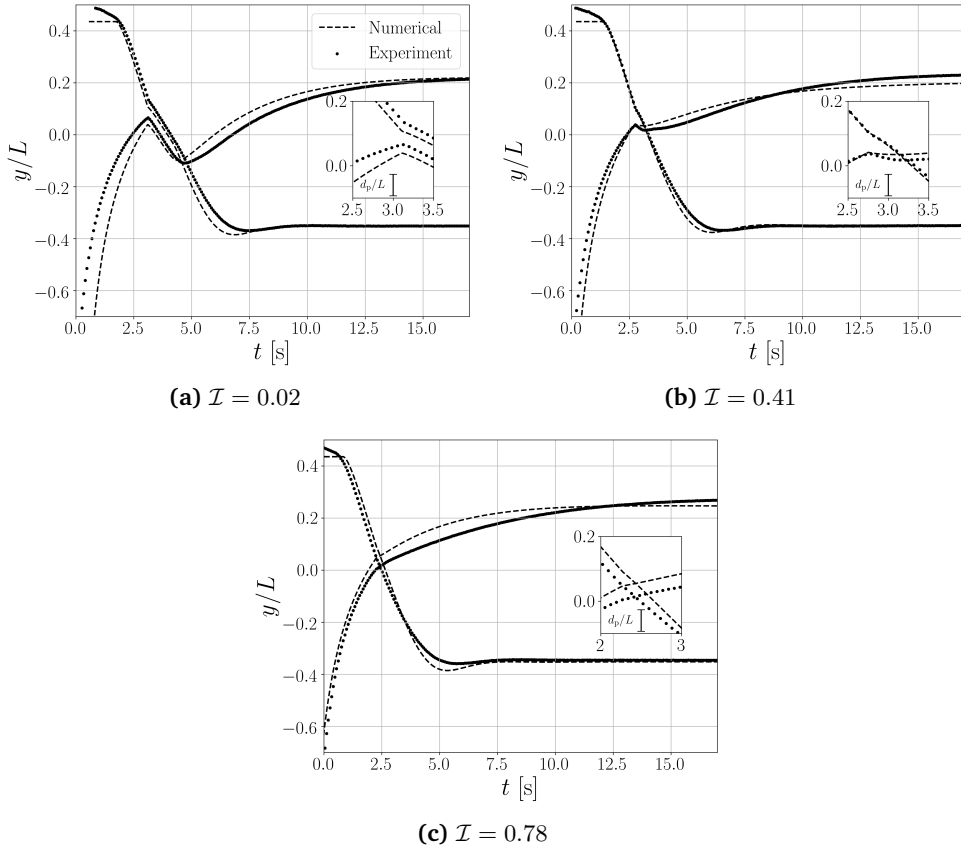
Figure 2.12.: Temporal evolutions of vertical positions of particles during binary collisions between a rising PVC-U particle and a falling POM particle with three different impact factors. The size of the particles are indicated by the vertical bars. Movies of the binary collision experiments and simulations are found at: Link to movie 1, Link to movie 2, Link to movie 3.
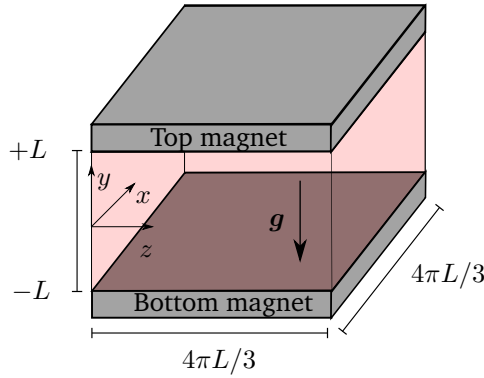
Figure 2.13.: A schematic of the computational domain for the many-particle simula-
tions. In a frame moving with the same velocity as the conveyor belts,
$U_0 \boldsymbol{i}$, the mean streamwise velocity of the fully-developed flow is zero.
In this frame, the walls at $y = \pm L$ are at rest.

convenient to solve the governing equations in a frame moving in x-direction with
the mean streamwise flow velocity U_0. In this frame, the mean velocity of the fully-
developed flow is zero, and the top and bottom walls are at rest. Therefore we impose
no slip and no penetration velocity boundary conditions at $y/L = \pm 1$, where the
surfaces of the two magnets are located. In x- and z-directions periodic boundary
conditions are imposed.

Figure 2.14 (a) depicts the magnitude of the magnetic field, and the corresponding
effective mass density of the magnetic fluid as functions of y. According to (2.21) and
(2.23), this configuration is capable of sorting a mixture $\rho_{\rm p}/\rho_{\rm f} \in [0.6, 1.4]$ ($|\Delta\rho_{\rm f,a}|_{\max} =
0.4\rho_{\rm f}$), with $\max(\frac{d\rho_{\rm f,a}}{dy}) = 0.97\rho_{\rm f}/L$ at the surface of the magnets. Particles with mass
densities in the range of $\rho_{\rm p,k}/\rho_{\rm f} \in [0.7, 1.3]$ are uniformly distributed over ten mass
density groups. These mass densities and their corresponding equilibrium heights are
indicated by dashed lines in figure 2.14 (a). Particles are initially randomly distributed
in two injection zones at the bottom, ($-1 < y/L < -0.75$) and top ($0.75 < y/L < 1$)
of the channel. The injected particles are pre-separated into two groups of light and
heavy particles. Particles heavier than the carrier liquid ($\rho_{\rm p,h}/\rho_{\rm f} \in (1, 1.3]$) are in-
jected at the bottom, and particles lighter than the liquid ($\rho_{\rm p,l}/\rho_{\rm f} \in [0.7, 1]$) are in-
jected at the top of the domain. For a more realistic initial condition, a particle
impurity is considered in each injection zone. The particle impurity is defined as
$\text{Imp} = \frac{N_{\rm p,h}}{N_{\rm p,top}} = \frac{N_{\rm p,l}}{N_{\rm p,bottom}}$, where $N_{\rm p,top}$ and $N_{\rm p,bottom}$ are the total numbers of par-
ticles injected in the top and bottom injection zones. $N_{\rm p,l}$ and $N_{\rm p,h}$ are the number
of light and heavy particles, respectively. In case of a perfect pre-separation $\text{Imp} = 0$,
whereas $\text{Imp} = 0.5$ indicates no pre-separation (fully random particle distribution).
For not pre-separated particles, during a short time interval, the apparent Galileo
number can be in the range $Ga \in [150, 218]$. We ignore deviations from the steady
vertical motion, caused by the transition in the wake of these particles.

The critical particle diameter as a function of particle mass density derived in section
2.5.1.1, is plotted in figure 2.14 (b). The maximum critical particle diameter corre-
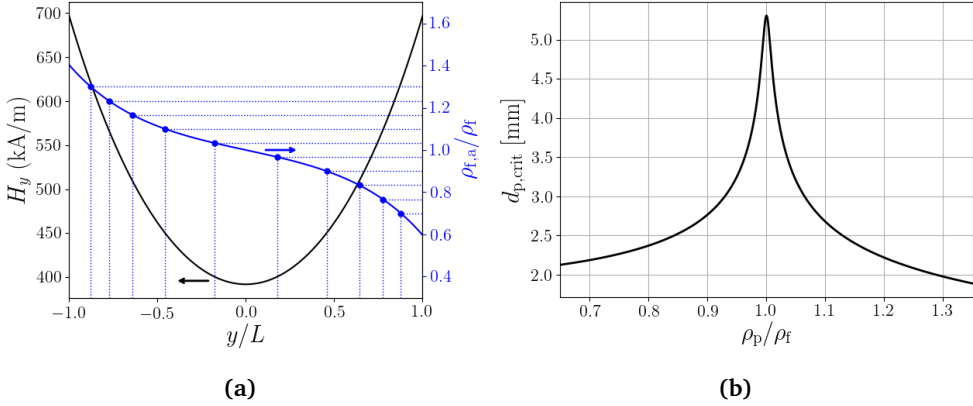
Figure 2.14.: (a) Magnetic field strength profile and the corresponding profile of the effective mass density of the magnetic fluid. The dotted lines indicate mass densities of the particles. The dashed lines correspond to the considered cut mass densities. The corresponding vertical axes are indicated by the horizontal arrows (b) Critical particle diameter as a function of mass density.

sponding to neutrally buoyant particles ($\rho_\mathrm{p}/\rho_\mathrm{f} = 1$) is about 5.3 mm. It is noteworthy that although the magnetic configuration is fully symmetric, the critical particle diameter profile is asymmetric: particles lighter than the magnetic liquid have a larger critical diameter than heavier particles with the same mass density difference.

The time step size is 0.0009 s. The numbers of grid points in stream-wise and span-wise directions are 256, and the wall-normal direction consists of 129 grid points. A window size of $0.01 t_\mathrm{max}$, with $t_\mathrm{max} = 35$ s is considered for the calculation of the Basset history force. The initial particle to fluid relative velocity is assumed to be zero.

In order to investigate the effect of different parameters on the separation performance, we study seven different test cases. Case 1A is considered as the base case. We study the effects of neglecting history force, two-way coupling, and particle-particle interactions on the collective motion of particles in cases 1B, 1C and 1D respectively. In case 2 the effect of the particle size is studied by decreasing the particle size from 4 to 2 mm. Case 3 investigates the effect of a higher particle volume fraction ($\Phi = 0.04$). Finally, case 4 addresses the effect of the initial particle impurity. The parameters of the test cases are summarized in table 2.4.

Inter-particle and wall-particle collisions are treated by the hard-sphere model addressed in Section 2.2.4.2. Based on the results of section 2.5.2.2, we consider an average value of 0.85 for the dry coefficient of normal restitution. The average lubricated friction coefficient is assumed to be 0.005.

We quantify the separation performance by the root mean square of the distances of the particles from their theoretical equilibrium point given in table 2.2. We define the non-dimensional separation error as::

Case	Φ	d_p[mm]	No. particles	Imp	History	Two-way coupl.	Collisions
1A	0.02	4	8835	0.1	yes	yes	yes
1B	0.02	4	8835	0.1	no	yes	yes
1C	0.02	4	8835	0.1	yes	no	yes
1D	0.02	4	8835	0.1	yes	yes	no
2	0.02	2	70685	0.1	yes	yes	yes
3	0.04	4	17671	0.1	yes	yes	yes
4	0.02	4	8835	0.5	yes	yes	yes

Table 2.4.: Summary of test cases.

$$e_\mathrm{m}(t) = \frac{1}{L}\sqrt{\frac{1}{N_p}\sum_{i=1}^{N_p}(y_{p,i}(t) - y_{e,i})^2}, \tag{2.51}$$

where N_p is the number of particles, $y_{p,i}(t)$ is the position of a particle at time t, and $y_{e,i}$ denotes its equilibrium height. The mean separation error defined by (4.27) can be evaluated for all particles to assess the overall temporal performance of the system, but also for each individual mass density group. In the former, N_p is the total number of particles, whereas for the latter N_p is the number of particles in the mass density group.

2.5.3.1. Case 1: Effects of history force, collisions, and two-way coupling

Figure 2.15 shows a cross-section of the velocity field and front view of the particle distribution in the moving frame at $t = 0.01$ s, $t = 0.5$ s, $t = 1.0$ s, $t = 1.5$, $t = 2$ s, and $t = 2.5$ s for case 1A where history effects, two-way coupling and collisions are taken into account. The horizontal colour bar shows the wall-normal component of the fluid velocity. The vertical colour bar corresponds to the particle mass density ratio $\rho_\mathrm{p}/\rho_\mathrm{f}$. It can be seen that after 2.5 s most of the particles have almost reached their equilibrium positions. A higher level of particle dispersion is observed in the central region of the channel than in the vicinity of the walls. First, particles with equilibrium positions in the central region interact more with other particles as they move to their equilibrium height. Second, the lower magnetic field gradient in the central region leads to a slower vertical motion of these particles and therefore a longer separation time.

The effects of history force, two-way coupling and collisions on the system overall separation performance are illustrated in figure 2.16 (a) where the mean separation errors for cases 1A-1D are plotted as functions of time. When history, two-way coupling and collision effects are taken into account the time required to obtain a mean separation error of 0.02 is about 3 s. This effectively means that achieving this separation accuracy at a mean streamwise velocity U_0 requires the length of the separation channel to be at least $3U_0$.

The decay behaviour of the mean separation error is almost identical for cases 1A-1D until $t = 1$ s. After this time, the decay rates for the cases without history force and
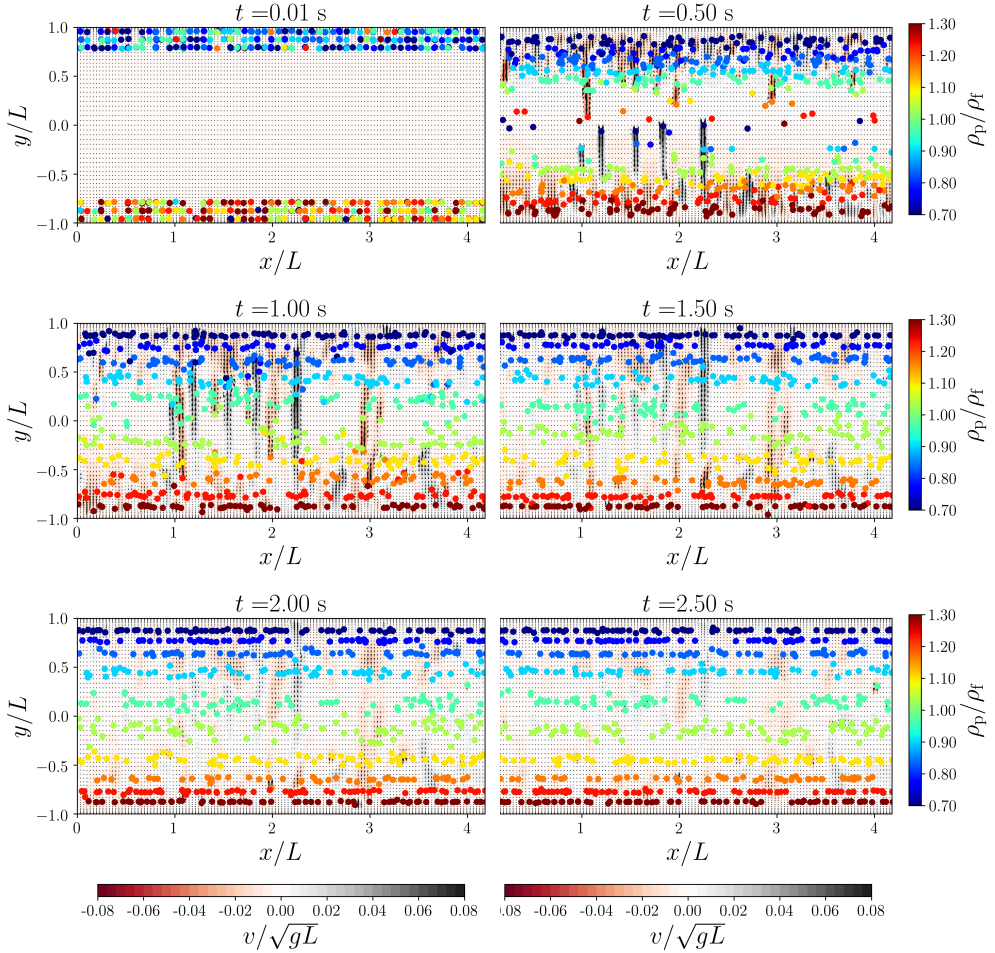
Figure 2.15.: Cross-sections of the velocity field in the moving frame at the plane where $z = \frac{L_z}{2}$, and projections of the particles in the section of the domain where $|z - \frac{L_z}{2}| < 3d_{\mathrm{p}}$ (Case 1A). The particles are coloured based on their relative mass density ρ_p/ρ_f (vertical colour bar). The horizontal colour bar corresponds to the streamwise component of the particle-induced fluid velocity. A movie corresponding to this figure (movie 4), and a 3D animation of the particle separation (movie 5) are found at: Link to movie 4, Link to movie 5.
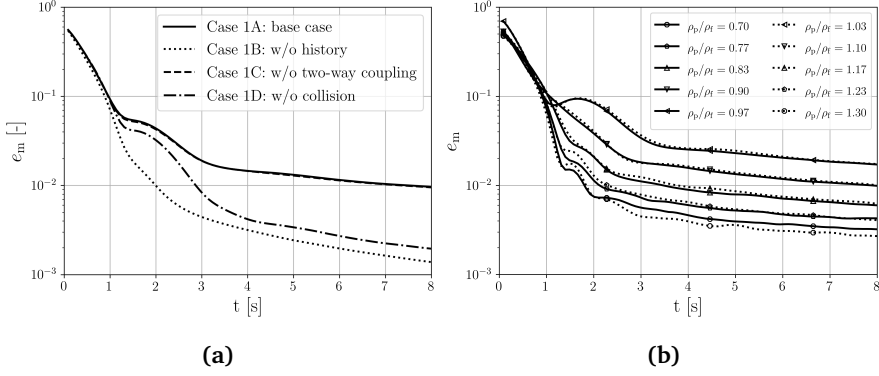
Figure 2.16.: (a) Average separation error versus time for cases 1A, 1B, 1C and 1D. (b) Average separation error per mass density as a function of time for case 1A.

collisions begin to deviate. Two-way coupling appears to have a negligible effect on the overall separation performance. Collisions increase the time required to achieve an average separation error of 0.02 by about 0.5 seconds. The effect of the history force is more drastic. Neglecting the history force leads to an underestimation of about 1.5 s in achieving $e_\mathrm{m} = 0.02$. When history effects are neglected, the average separation error decreases monotonically, whereas, with history force included, the mean separation error reaches a plateau at $t \approx 1.5$ s. History effects introduce additional resistance to particle levitation. Moreover, when a particle reaches its equilibrium point, the history force drags the particle away from it. Both effects lead to a decrease in the decay rate of the average separation error of the system.

Temporal evolutions of average separation errors per mass density group for case 1A are compared in figure 2.16 (b). Until $t \approx 1$ s, all mass density groups show a similar decay behaviour. At a given time $t > 1.3$ s, the larger the absolute fluid-particle mass density difference of a group, the smaller is the average separation error of that group. The distinguishing behaviour of mass density groups with $|1-\rho_\mathrm{p}/\rho_\mathrm{f}| = 0.03$ is interesting. On average, particles in these mass density groups travel the longest distance to reach their equilibrium positions. Due to history effects, these particles overshoot their equilibrium positions. Moreover, compared to other particles, the "restoring" magnetic buoyancy force acting on particles in these groups is smaller in the central region of the channel where the gradient of the magnetic field is low. These two effects lead to a period of increase in the separation error between $t \approx 1.3$ s and $t \approx 1.7$ s. A similar behaviour is observed for groups with $|1 - \rho_\mathrm{p}/\rho_\mathrm{f}| = 0.3$ and $|1 - \rho_\mathrm{p}/\rho_\mathrm{f}| = 0.23$ during the interval $t \in [1.25, 2]$ when the particles which were in the "wrong" injection zone reach their equilibrium positions.

To illustrate the effect of collisions and history force on the temporal evolution of the local distribution of particles, in figure 2.17 the probability density function of the vertical position of particles for cases 1A, 1B and 1C are compared. After only 0.96 s, a clear difference is observed in the distributions of the particles when history effects are neglected. The history force enhances particle dispersion and causes a larger variance in particle positions. The effect of history force becomes more prominent at
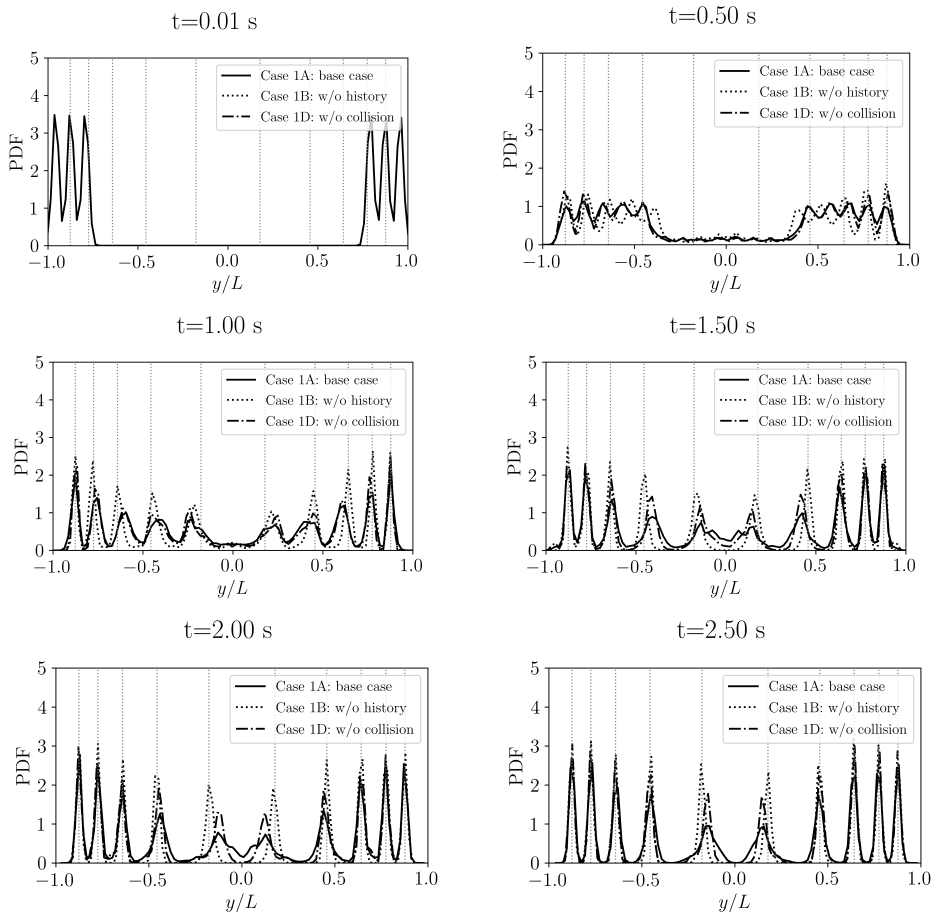
Figure 2.17.: Evolution of probability density function of particle position for cases 1A, 1C, and 1D. The corresponding animation, movie 6 is available at: Link to movie 6 (The movie on the right corresponds to the case 1A).

$t = 2$ s. Without history effects, the distribution of particle positions in the central region deviates both in variance and average value. Collisions, on the other hand, only influence the variance of the particle position. The effect of collisions is stronger for particles with equilibrium positions in the central region, since these particles travel over a larger vertical distance and collide more often.

The results presented in the following subsections include the history force, collisions, and two-way coupling.
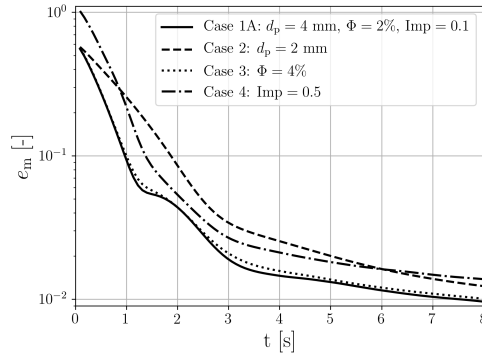
Figure 2.18.: Effects of particle size, initial separation and volume fraction on the mean separation error.

2.5.3.2. Cases 2, 3 and 4: Effects of particle size, pre-separation and volume fraction

We investigate the effect of particle size on the separation performance by changing the particle size from 4 mm to 2 mm while the total volume fraction of particles is kept constant. Figure 2.18 compares the temporal evolution of average separation errors for the two considered particle sizes. The average separation error for 2-mm particles after 5 seconds is 0.3 while this value for 4-mm particles is as low as 0.01. The superior separation performance of case 1A is in line with the findings of section 2.5.1.1. The difference between the decay behaviour stems from the higher magnetic force on the larger particles. Moreover, with a constant volume fraction, smaller particles collide more frequently with other particles which leads to a lower separation performance. As can be seen in figure 2.14, $d_\mathrm{p} = 2$ mm is smaller than the smallest critical particle diameter. Therefore, a 2-mm particle exhibits a non-oscillatory motion towards its equilibrium point, leading to a monotonic decay of the average separation error.

The dash-dotted line in figure 2.18 shows the temporal evolution of the mean separation error for an initial impurity of 0.5. This corresponds to a case where particles are not initially separated into two mass density groups of heavy and light particles but are randomly distributed over both injection regions. This has a negative effect on the separation performance since particles have to travel further to reach their equilibrium position, which also results in a larger number of collisions. Pre-separation decreases the time required to obtain an average separation error of 0.02 by about 33% (3 s versus 4 s).

Increasing the particle volume fraction from 2 to 4 percent slightly increases the separation error. This small increase can be attributed to the larger effect of two-way coupling and the large number of particle collisions, which both increase mixing.

49

2.6. Conclusions and outlook

In this work, we presented a point-particle Euler-Lagrange approach which can accurately capture the collective motion of almost neutrally buoyant particles in the flow of magnetically responsive liquids. Numerical simulations are performed on single and multi-particle systems over the range of apparent Galileo number $0 \leq Ga_a < 220$. This has relevant applications in magnetic density separation systems, which are used for the separation of different types of plastic. The numerical results of single- and two-particle simulations are in good agreement with detailed experimental results on particle position.

It is shown that when history force is neglected, a maximum of five parameters can characterize the buoyancy-driven vertical motion of a spherical particle towards its equilibrium point. We compared the contributions of different hydrodynamic forces to the motion of a single particle and showed that the Basset history force is important for large particles. Is is found that neglecting history force at large particle diameters can lead to a significant underestimation of the levitation time.

We presented a hard-sphere collision modelling strategy which can accurately capture inter-particle interactions in a magnetized paramagnetic liquid. Numerical and experimental investigations of binary collisions considered in this study show that depending on the impact factor a single particle-particle collision can lead to up to approximately 45% increase in the particle levitation time. The separation performance of large MDS systems where up to about 18000 particles are levitated is quantified by evaluating the mean separation error. Particularly, the effects of particle size and particle pre-separation have been studied. The investigations revealed that the effects of history force and collisions are important even at particle volume fractions as low as 2%. Neglecting history force and collisions lead to an erroneously reduced particle dispersion, especially for particles with mass density ratio close to one. Our numerical results showed that a decrease in the particle size from 4 to 2 mm increases the time required to achieve an average separation error of 0.02 by around 40%, indicating the importance of particle size distribution in MDS applications. The method described in this paper is a firm basis for the development of useful design rules for optimization of future magnetic separation technologies.

As a natural starting point for most studies on particle-laden flows, this work was based on the assumption of spherical particle shape. However, it is well known that particle non-sphericity has a significant influence on fluid-particle interactions, and therefore on the dynamics of particles. Furthermore, this work did not consider the effect of background flow disturbances on the motion of particles. Background turbulence can remarkably delay the levitation time as particles in MDS typically have mass density ratios close to one. Such particles have small relaxation times, and their motion is therefore sensitive to a background flow. These two aspects are open to future research.

2.7. Acknowledgements

3. Hydrodynamic forces and torques on low-aspect-ratio spheroidal particles

In the previous chapter, we presented a numerical framework for simulating flows of magnetized liquids laden with spherical particles. In order to extend the applicability of the proposed framework to low-aspect-ratio non-spherical particles, accurate models for hydrodynamic interactions of these particles should be derived. In this chapter[1], a statistical learning approach is presented to derive models for Reynolds-number- and orientation-dependent steady hydrodynamic forces and torques on thin spheroidal particles.

3.1. Introduction

The motion of non-spherical solid particles in viscous fluids has been the subject of research for several decades. Atmospheric particle transport, sediment transport in river beds, material processing and separation, and blood flow are just some examples of flows laden with non-spherical particles. Although the simplifying assumption of a spherical shape is often made, it has been shown that particle non-sphericity can have a significant influence on fluid-particle interactions and thus on particle transport [7, 13, 30, 150].

Accurate knowledge of hydrodynamics forces and torques acting on particles is of great importance in the numerical study of particle-laden flows. Non-spherical particles are often modelled as fibres, cylinders or ellipsoids. The smoothness and symmetry properties of spheroids have made them attractive subjects of analytical and numerical studies.

Two general approaches to model fluid-particle interactions in Euler-Lagrange simulations are particle-resolved and point-particle methods. Particle-resolved methods aim at resolving the flow field around the particle and obtaining the hydrodynamic forces and torques through numerical integration of fluid stresses over the surface of the particle. Particle-resolved methods require a grid resolution high enough to capture the single-particle hydrodynamics. This limits the applicability of such techniques to small fluid-particle systems. Point-particle methods, on the other hand, use empirical or theoretical models for the hydrodynamic interactions between the particle and the fluid. Due to their lower computational costs, point-particle methods have been extensively applied to investigate particle-laden flows [40, 41, 80, 153].

The success of point-particle simulations is directly dependent on the accuracy of the

---

[1]This chapter is based on the article: "Statistical learning method for predicting hydrodynamical drag, lift and pitching torque on spheroidal particles". S. Tajfirooz, M. Hausmann, J.G. Meijer, J.G.M. Kuerten, J.C.H. Zeegers, and J. Fröhlich (2021). *Physical Review E Journal*

incorporated force and torque models. Clift et al. [30] provided a comprehensive review of drag laws for various particle shapes and flow regimes. In the limit of spherical particles, at moderate rotational Reynolds numbers, the coupling between the translational and rotational motion is small. Analytical and empirical expressions have been derived which describe the hydrodynamic interactions of rigid spherical particles within and beyond the creeping flow limit [17]. Such expressions include several fluid-particle interaction mechanisms such as steady-state drag, virtual mass, force due to the undisturbed velocity field, and history effects.

The complexity of the motion of non-spherical particles stems from the strong coupling between the translational and rotational motions at high particle anisotropies. Moreover, unlike for spheres, the non-dimensional numbers cannot be based on a single length scale, making the motion of a non-spherical particle dependent on a larger number of influence parameters [30]. In the Stokes regime, analytical force and torque models for non-spherical particles exist. Oberbeck [102] was among the firsts to investigate the drag force on a low-aspect-ratio spheroidal particle moving along its principal axis in a viscous fluid. Jeffery [70] explored the low-Reynolds number motion of ellipsoidal particles in shear flows and derived expressions for the shear-induced torque on ellipsoids. Under the assumption of creeping (Stokes) flow, Happel and Brenner [60] analytically derived drag and lift coefficients for ellipsoidal particles at different orientations. Their correlation describes the drag coefficient at a given incidence angle by values of drag coefficient at extrema of the incidence angle and a sine-squared function of the incidence angle.

The expressions for force and torque coefficients in creeping flows have been incorporated in Euler-Lagrange simulations of non-spherical particles in laminar and turbulent flows. In such studies it is assumed that the fluid inertial effects are insignificant [45, 92, 150, 155]. However, it has been observed that such correlations can lead to significant errors at high particle Reynolds numbers [2, 6].

Many authors have collected several numerical and experimental data for Reynolds- and orientation-dependent drag, lift and torque coefficients of non-spherical particles at finite Reynolds numbers [47, 51, 62, 63, 72, 87, 107, 108, 112, 116, 120, 121, 154]. In 2008, Loth [87] collected the existing correlations for regular and irregular shapes in the Stokes and Newton regimes and addressed the applicability of combined correlations for intermediate regimes. He found that the sphericity can not be used as the only input parameter for the prediction of drag force outside the Stokes regime and that these correlations lose their accuracy as deviations from a sphere become large. Later Hölzer and Sommerfeld proposed new correlations based on a broad set of numerical and experimental data that involves different projected areas to account for particle orientation [62, 63]. Zastawny et al. [154] used the immersed boundary method (IBM) to investigate different non-spherical particles at different incident angles and Reynolds numbers in the steady flow regime. Based on the work of Rosendahl [116], Zastawny provided shape-specific correlations for drag, lift, and torque on two ellipsoidal particles and a fibre-shaped particle. Due to the limitations of the IBM method, Zastawny et al. [154] used relatively small computational domains for simulations at low Reynolds numbers ($Re \leq 1$), which led to a considerable reduction in the accuracy of their correlations in this regime [108, 120].

Jiang et al. [72] numerically studied a 6:1 prolate spheroid at $45°$ incidence angle

and compared their results with the correlation of Zastawny for a fibre with the same aspect ratio and that of Hölzer and Sommerfeld [63], obtaining very good agreement at low Reynolds numbers. At higher Reynolds numbers deviations up to 29% were observed. More recently, Sanjeevi et al. [120] performed extensive Lattice Boltzmann simulations of the flow around a 2:5 oblate ellipsoid, a 5:2 prolate ellipsoid and a 4:1 fibre up to $Re = 2000$ to extract force and torque coefficients and also derived separate correlations for these three shapes. Due to the wide range of Reynolds number considered by these authors, they were not able to fit their computed data to the original correlations of Zastawny. They instead used a modified version of the sine-squared type correlation. Sanjeevi *et al.* showed that for prolate spheroids of aspect ratio up to 32, the sine-square behaviour of the drag coefficient derived by Happel and Brenner, can be extended to the high-Reynolds number regime. They also observed that due to the stronger wake contribution to the drag force, the drag coefficient of low-aspect-ratio oblate spheroids does not follow the sine-square law. Andersson and Jiang [6] investigated the flow around an inclined 1:6 oblate ellipsoid at low but finite Reynolds numbers and addressed the challenges in simulating flow over bluff bodies at small Reynolds numbers. Their findings also questioned the reliability of finite Reynolds number correlations at Reynolds numbers of order 1.

The shaped-specific force and torque correlations can serve as useful models for point-particle simulations of non-spherical particles. However, it has been shown that the applicability of a correlation to other particle shapes is limited. Furthermore, force or torque correlations for non-spherical particles that cover a broad range of particle Reynolds number or different particle shapes are scarce. A single correlation is not capable of predicting hydrodynamic loads over a wide range of Reynolds numbers, aspect ratios, and incidence angles. Different correlations are commonly considered for multiple distinct ranges of one or more input parameter(s). The main reason for this is the difficulty in finding a proper fitting approach that considers the large input space in the right way and does not introduce unsatisfactory high biases.

In this work, we propose a different approach for predicting the hydrodynamic interactions between non-spherical particles and surrounding fluid. Instead of the conventional curve fitting approach, we use an artificial neural network to correlate the force and torque data generated by resolved numerical simulations to a set of input parameters. Artificial neural networks have been applied in various areas from data classification and image processing to motion prediction, and pattern recognition. Recently, statistical learning has also been used in fluid dynamics and multi-phase flows [23]. For example, Sarghini et al. [122] applied a neural network to predict the Smagorinsky constant in large-eddy simulations, Ling et al. [84] derived a neural network-based Reynolds stress closure for Reynolds averaged Navier-Stokes equations. He and Tafti [61] used a neural network to predict the effect of particle volume fraction and distance to neighbouring cells on drag force on spheres. Lui and Wolf [89] combined NN-based regression with flow modal decomposition to construct reduced order models for fluid flow over bluff bodies, and Buzzicotti et al. [24] studied the application of convolutional neural networks to the reconstruction of fluid turbulence data.

Neural networks, being stochastic tools, are generally difficult to reproduce. Still, the significant advantage of a neural network is the theoretical ability to approximate every Borel measurable input-output relation [57]. However, in the context of pre-

diction of hydrodynamic interactions, NN-based trend prediction has three distinct advantages over conventional curve-fitting approaches.

First, to obtain a conventional curve-fitting-based correlation from simulation data, a functional approach is necessary. The choice of a fitting analytical function (linear, quadratic, sine-square, etc.) can oversimplify an actual complex dependency which might not be captured due to a low number density of data points, inaccuracy of the computational model, or a limited range of data. The forced behaviour of the considered function can lead to high deviations, especially for values lying between or outside the fitting points where interpolation or extrapolation is required. If trained properly, a neural network can predict any dependency without a prior assumption—this way, the difficult task of finding an appropriate fitting function is circumvented.

Second, fitting an analytical function to a partially erroneous dataset can deteriorate the quality of the prediction over a broader input domain. Correlations inherit the errors in the data as intrinsic biases. Such biases generated by conventional curve-fitting approaches can lead to large temporally accumulated errors in results of time-dependent point-particle simulations incorporating such models. In contrast, the variance error typically generated by DNN predictions is averaged out in time, and therefore leads to smaller accumulated errors.

Third, several authors have used different computational methods to derive correlations for hydrodynamic forces and torques. Due to the same reasons mentioned above, for a given problem, the results are usually not identical. This leads to a variety of functional approaches for the same relation. The results of the simulations from different authors can not be used because they are incompatible with the respective correlation approaches. Thus, a large number of valuable data can not be used. A neural network, instead, can process the data of all authors and minimize the effect of the individual errors of every data set.

A few studies have addressed the steady axisymmetric flow over thin oblate ellipsoids [30, 93, 104, 112, 115]. But to the best of the authors' knowledge, orientation- and Reynolds-number-dependent force or torque correlations for low-aspect-ratio spheroids or disks do not exist, so far. We take the incidence angle and the particle Reynolds number as input parameters and employ a statistical approach to predict the coefficients of drag, lift and pitching torque of a 1:10 oblate spheroid.

The considered range of Reynolds number in this work is $1 \leq Re \leq 120$. It is known that in the buoyancy-driven motion of a particle within this regime, the particle has a vertical trajectory and exhibits no appreciable secondary motion [28]. This allows to extract hydrodynamic loads from steady-state body-fixed simulations. We perform a set of resolved simulations to obtain force and torque data. A well-designed feed-forward NN is then trained with a subset of the collected data. We show that the NN-based predictions are at least as accurate as predictions of empirical and theoretical correlations. We test the performance of our model by incorporating it in a point-particle simulation of the buoyancy-driven motion of an oblate spheroid in a liquid with a nonlinear hydrostatic pressure gradient.

The mathematical model and the numerical method employed for the resolved simulations are presented in section 3.2.1. The considered feed-forward network and the training and validation procedures are addressed in section 3.2.2. In section 3.3 the

results are presented and discussed, and the performance of the new model is tested in a point-particle simulation of a particle settling in a magnetic liquid. The concluding remarks and future directions are presented in section 3.4.

3.2. Methodology

In this section, we first introduce the mathematical model and the numerical approach for the resolved simulations. Next, the training and a validation procedure of the considered neural network-based correlations are addressed.

3.2.1. Resolved simulations

3.2.1.1. Mathematical description of the flow

We solve the flow around a spheroidal particle with length b along the axis of symmetry and maximum diameter normal to this axis equal to a. The aspect ratio is defined as $w = b/a$ and fixed to $w = 0.1$ in the present case to yield an oblate spheroid. The particle is located in the centre of the coordinate system, with x the streamwise, y the pitchwise and z the spanwise coordinate. Indeed, the particle is mounted symmetrically to the x-y plane and Φ denotes the pitching angle, i.e. the angle of incidence to the flow. The steady Navier-Stokes equations are solved in a cubic computational domain, as shown in figure 3.1. The fluid motion is described by the system

$$\nabla \cdot (\mathbf{u} \otimes \mathbf{u}) = \frac{1}{\rho_f} \nabla \cdot \boldsymbol{\tau} \quad \text{in } \Omega_f, \tag{3.1}$$

$$\nabla \cdot \mathbf{u} = 0 \quad \text{in } \Omega_f, \tag{3.2}$$

where the hydrodynamic stress tensor is

$$\boldsymbol{\tau} = -p\mathbb{I} + \mu_f \left(\nabla \mathbf{u} + (\nabla \mathbf{u})^T \right). \tag{3.3}$$

Here, $\mathbf{u}$, p, and ρ_f are the fluid velocity, pressure, fluid mass density respectively. The dimensions of the computational domain in stream-wise and the two span-wise directions are L_x and $L_z = L_y$. The distance of the particle centre from the inlet, and the span-wise distances from the walls are $L_x/2$, and $L_z/2 = L_y/2$, respectively.

At the inlet boundary, Γ_{in}, a uniform Dirichlet boundary condition is applied that sets the velocity vector to $\mathbf{u} = (u_0, 0, 0)^T$ with $u_0 = 1 \frac{\text{m}}{\text{s}}$. At the outlet boundary, Γ_{out}, the stress on the outlet boundary is set to zero. In case of a backflow, the outlet pressure is adjusted to prevent fluid from entering the domain through the outlet boundary [32]. A slip condition with zero normal velocity and zero tangential shear stress is imposed at the side boundaries, Γ_{wall}, where

$$\mathbf{u} \cdot \mathbf{n} = 0, \quad \left(-p\mathbf{I} + \mu \left(\nabla \mathbf{u} + (\nabla \mathbf{u})^T \right) \right) \mathbf{n} = \mathbf{0}. \tag{3.4}$$

At the surface of the spheroid, Γ_p, a no-slip boundary condition is imposed i.e. $\mathbf{u} = (0, 0, 0)^T$.
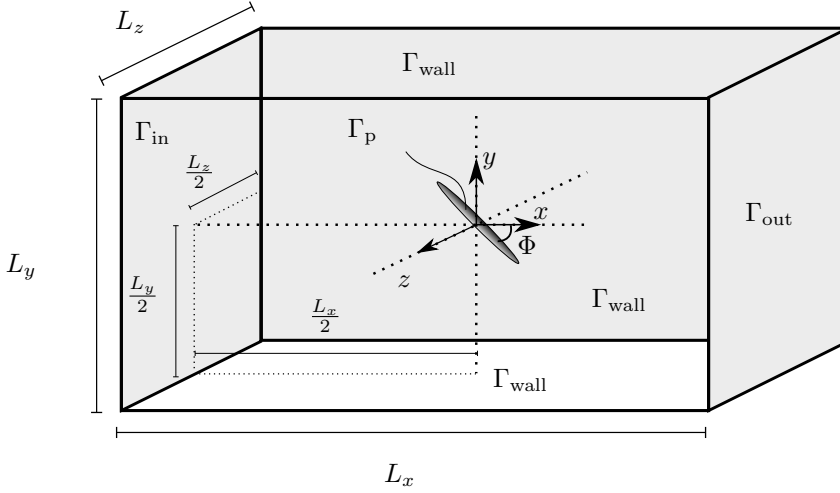
Figure 3.1.: Sketch of the computational domain, Ω_{f} and the particle mounted inside the domain.

The equatorial diameter of the spheroid $d = 2a$ is taken as the length scale for evaluation of the particle Reynolds number $Re = \frac{u_0 \rho_{\mathrm{f}} d}{\mu_{\mathrm{f}}}$. Different Reynolds numbers are achieved by varying the fluids dynamic viscosity μ_{f}. The particle incidence angle Φ is changed by rotating the spheroid around the $z-$axis. Forces and torques acting on the particle are obtained by integration of the total stress and its moment around the surface of the particle:

$$\boldsymbol{F} = \int_{\Gamma_p} \boldsymbol{\tau} \cdot \boldsymbol{n} \, \mathrm{d}A, \tag{3.5}$$

$$\boldsymbol{T} = \int_{\Gamma_p} \boldsymbol{r} \times \boldsymbol{\tau} \cdot \boldsymbol{n} \, \mathrm{d}A, \tag{3.6}$$

with $\boldsymbol{r}$ the distance vector from the centre of mass of the particle to a point on the surface Γ_p

3.2.1.2. Numerical discretization

The stabilized Galerkin finite element method in COMSOL Multipysics is used to solve (3.1) and (3.2) in the weak form. Linear basis functions (P1P1) are used for the velocity and pressure approximations. To ensure numerical stability, the finite element formulation is stabilized by streamline diffusion and crosswind diffusion methods [32]. The weak formulation of (3.1) is linearized by a "damped" Newton method. The system of linear equations resulting from discretization is solved using the generalized minimal residual (GMRES) method [32].
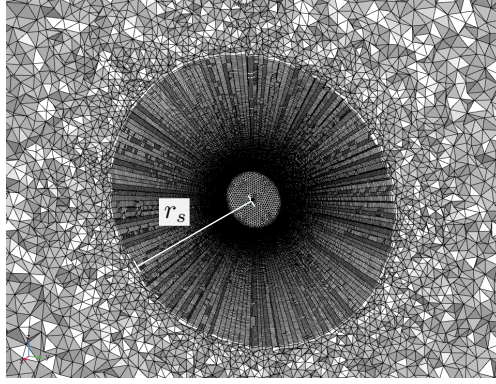
Figure 3.2.: Example of the mesh in the region close to the spheroid. To accurately resolve the flow in the vicinity of the particle, a spherical swept region with radius r_s is considered around the particle.

The surface of the spheroid is discretized using triangular surface elements with a maximum size of $\delta_{\max}$. The volume mesh consists of a combination of tetrahedra and prisms. To accurately capture the boundary layer near the surface of the spheroid and the downstream wake, a swept mesh is considered within the spherical region $x^2 + y^2 + z^2 \leq r_s^2$, where r_s denotes the radius of the swept region. This swept region is discretized by n_s layers of elements. Their maximum-to-minimum element size in radial direction is γ_s. Using a swept region which is fixed to the spheroid, keeps the mesh skewness at different incidence angles constant. An example of the mesh is shown in figure 3.2.

3.2.2. Correlation procedure

3.2.2.1. Data acquisition

A database is collected from 266 simulations performed with 14 different Reynolds numbers and 19 different angles of incidence. The two independent input variables are the Reynolds number, Re, and angle of incidence, Φ. The output parameters are the coefficients of drag, lift and pitching torque defined as

$$c_D = \frac{|F_D|}{\frac{1}{2}\rho_{\mathrm{f}}u_0^2 A},$$ (3.7)

$$c_L = \frac{|F_L|}{\frac{1}{2}\rho_{\mathrm{f}}u_0^2 A},$$ (3.8)

$$c_T = \frac{|T_p|}{\frac{1}{4}\rho_{\mathrm{f}}u_0^2 Ad},$$ (3.9)

respectively, where $A = \pi d^2/4$ is the cross sectional area of the spheroid, and $F_D = \boldsymbol{F} \cdot \boldsymbol{i}$, $F_l = \boldsymbol{F} \cdot \boldsymbol{j}$ and $T_p = \boldsymbol{T} \cdot \boldsymbol{k}$ with $\boldsymbol{i}$, $\boldsymbol{j}$ and $\boldsymbol{k}$ denoting the unit vector in x-, y- and z-direction respectively. Note that since the upstream flow is uniform and the

computational domain is symmetric in the z-direction, the total torque acting on the particle has only one contribution, being the pitching torque.

The parametric study of Chrust et al. [27] on wake transition scenarios of oblate spheroids at $\Phi = 90°$ showed that the transition behaviour for a thin oblate spheroid is very similar to that of a disk ($w = 0$). The authors observed a similar seven-stage transition scenario in the wake of thin oblate spheroids as in that of disks. In the thin-disk-like scenario, for a given aspect ratio, as the Reynolds number increases from zero, the first (primary) bifurcation at the first critical Reynolds number, $Re_{c,1}$ leads to a steady non-axisymmetric wake. At this state, i.e $Re_{c,1} \leq Re \leq Re_{c,2}$, the planar symmetry remains sustained and a steady lift force acts in the wake symmetry plane. As the Reynolds number further increases to the second critical Reynolds number, $Re_{c,2}$, under a Hopf-type bifurcation the wake transits to a periodic state, and the planar symmetry vanishes.

A decrease in the aspect ratio of an oblate spheroid leads to an increase in both the first and the second critical Reynolds numbers. For a disk ($w = 0$) Chrust et al. [27] found the Reynolds number range $117 \leq Re \leq 125.2$ for the stability interval of the steady non-axisymmetric state with planar symmetry. This range for a 1:6 spheroid was found to be $130 \leq Re \leq 137.2$. By interpolating the values for a disk and a 1:6 spheroid, for the steady planar-symmetric wake of a 1:10 spheroid, Chrust et al. estimated the first critical Reynolds number to be $Re_{c,1} \approx 130$. Shenoy and Kleinstreuer [127] observed a value of $Re_{c,1} = 135$ for the first critical Reynolds number of a 1:10 circular disk. Based on these observations, the particle wake is expected to remain steady at all incidence angles within the considered range of Reynolds numbers in this study ($Re \leq 120$). This legitimates the choice of steady-state simulation.

Figure 3.3 illustrates the two-dimensional space of input parameters. Due to the symmetry of the considered geometry, it suffices to consider the incidence angle range $0° \leq \Phi \leq 90°$. The number density of data points at lower Reynolds numbers is increased to make sure that the observed strong input-output dependency in this region mentioned by Clift et al. [30] is accurately captured.

It is well known that the drag, lift and pitching torque coefficients in the Stokes regime depend linearly on Re^{-1} [30]. To reduce the non-linearity of the input-output relation, we choose the output variables to be coefficients of drag, lift, and pitching torque multiplied by the Reynolds number. This way, at least in the Stokes regime, the dependency to be predicted reduces to a constant function.

3.2.2.2. Correlation via neural network

After all resolved simulations have been performed, an input-output correlation has to be found, in the form

$$y = \Theta(x, \theta), \quad (3.10)$$

where x and y are the arrays of input and output, respectively, θ is the array of unknown parameters (weights and biases). Conventional regression (curve fitting) methods make an assumption for the function Θ and find the unknown parameters through a minimization procedure. Finding a proper function (or a combination of functions) which captures all relevant features of the actual input-output relation can
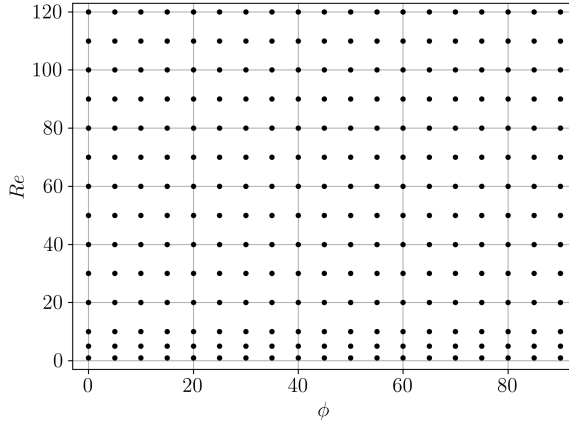
Figure 3.3.: An illustration of the Re-Φ space on which the resolved simulations are performed. Each dot represents one simulation.

be cumbersome. Instead, we use deep learning to find an appropriate function as well as the vector $\boldsymbol{\theta}$.

The basic idea of deep learning is to replicate an unknown complex function from known input and the corresponding output. A complex function is approximated by a combination of simpler functions which results in a so-called deep neural network (DNN). Through a deep learning process, the optimal parameters are found by minimizing (or maximizing) a target function. An example of such a target function is the difference between the output predicted by the neural network and the target value. This is the basic principle of one of the most applied neural network optimization approaches, the gradient descent method.

A DNN consists of multiple layers with several neurons. Every neuron is associated with one piece of information, its activation value. In each layer of a DNN, an input vector undergoes an element-wise nonlinear transformation which consists of a linear transformation through weights and biases followed by a nonlinear activation through the so-called "activation function". The activation values of the neurons in the first layer (input layer) are defined by the input data set. In the output layer, activation values are based on network connections. Neurons belonging to interior layers, or the so-called hidden layers, are connected to the neighbouring layers via the weights and biases corresponding to each neuron. One famous representative of deep learning is the feed-forward DNN, also known as a multilayer perceptron. In a feed-forward DNN, the information propagates from the input layer through the hidden layers to the output layer. The basic architecture of a feed-forward DNN is depicted in figure 3.4. For a network with l hidden layers the activation values of the kth hidden layer read

$$h_j^{(1)} = f^{(1)} \left(\sum_{i=1}^{n_k} \omega_{ij}^{(1)} x_i + b_j^{(1)} \right), \tag{3.11}$$

61
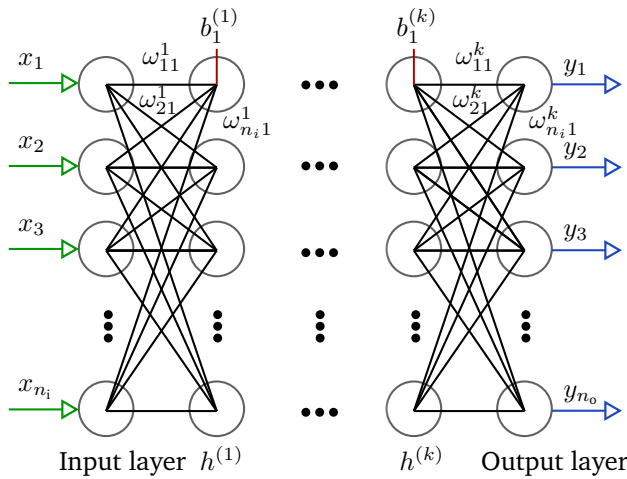
Figure 3.4.: Graphical representation of the architecture of a typical feed forward neural network with n_i inputs, n_o outputs and k hidden layers each consisting of n_k neurons.

for $k = 1$ and

$$h_j^{(k)} = f^{(k)} \left(\sum_{i=1}^{n_k} \omega_{ij}^{(k)} h_i^{(k-1)} + b_j^{(k)} \right), \tag{3.12}$$

for $2 \leq k \leq l - 1$, where $f^{(k)}(x)$ is the activation function, and $\omega_{ij}^{(k)}$ and $b_j^{(k)}$ are the weights and biases of the kth layer. n_k is the number of neurons in the kth layer.

The weights and biases are found through a "training" procedure. During the training process, the weights and biases are changed to achieve an arbitrarily minimal difference between training data and network predictions and thus also a preferably accurate estimation of unknown weight and bias values. A loss function, j, is defined to quantify the quality of the predictions. One possibility for a loss function is the mean squared error between the predictions and the actual output values. The most common ways to minimize this loss are based on the iterative gradient-based optimization algorithm, "Gradient Descent". A vector $\boldsymbol{\theta}$, which represents weights or biases, is updated as follows:

$$\boldsymbol{\theta}_{t+1} = \boldsymbol{\theta}_t - \eta \boldsymbol{\nabla}_{\boldsymbol{\theta}} j \left(\boldsymbol{x}, \boldsymbol{y}_d, \boldsymbol{\theta}_t \right), \tag{3.13}$$

where $\boldsymbol{\nabla}_{\boldsymbol{\theta}} j$ denotes the gradient of the loss function with respect to $\boldsymbol{\theta}$. The gradient itself depends on the input values $\boldsymbol{x}$, the desired outputs $\boldsymbol{y}_d$ and the other parameters $\boldsymbol{\theta}_t$.

The parameter η controls the learning rate by changing the step sizes of the updates. its value should be chosen such that the iterative procedure finds small local minima of the loss function. Too small learning rates yield too slow optimization and the risk of getting stuck in large local minima. Too large learning rates may cause oscillations around a minimum. To avoid this, optimizers are derived that dynamically determine the learning rate [119]. The so-called Adam-Optimizer has been shown to provide

beneficial convergence properties. This algorithm converges faster, and to a lower minimum than competitors like AdaGrad or AdaFom [26]. The Adam optimizer varies the step size based on the history of the gradients and the squared gradients by means of an exponential moving average. A detailed description of the algorithm can be found in the original publication of Kingma and Ba [78].

Besides the optimizer some additional aspects of a DNN have to be considered. First, the weights and biases have to be initialized in a certain way. In the present neural network the weights are initialized as small random values and the biases as zero. A common problem in the training process is so-called overfitting, which occurs when the neural network predicts the training values precisely but loses its accuracy with a new dataset. To avoid this, regularizers are implemented. The initialization, the effect of overfitting and different ways of regularization are described in detail by Goodfellow et al. [57].

Additionally, the activation function, the number of hidden layers and the number of neurons in every hidden layer are application-specific parameters (hyper-parameters), which influence the performance of the network. Especially finding the appropriate activation function without testing it is almost impossible, since its influence is not fully understood yet [57].

In order to validate the trained DNN, out of the total data acquired from 266 simulations, 30 randomly selected simulation data points are excluded from the training data and are reserved for the validation. This way, the neural network is validated with data it has not seen before. The random sampling of the data for validation is repeated to make sure that the network prediction performance is not dependent on the random choice of the training data sample.

The considered neural network in the present study consists of three hidden layers with 300 neurons. That means there are approximately 4×10^5 floating point operations per prediction. This number can be reduced by decreasing the number of neurons. With more experience, this is probably possible without a significant loss of accuracy by careful variation of the hyper-parameters. The neurons of the hidden layers are activated by the so-called rectified linear (ReLU) activation functions. The outputs of the ReLU function are zero for negative inputs and equal the input for positive inputs [57]. Input and output layers have a linear activation function. The mean absolute error between predicted outputs and simulation data is minimized by an Adam optimizer. An L2 parameter norm penalty is used for the regularization. The network is trained 500 epochs with the 236 training data points in mini-batches of size 32. This means that an update is applied after 32 data points until every data point is used 500 times. The training of the DNN is performed by Keras, an extension of the open-source machine learning library Tensorflow [1].

3.3. Results and discussions

3.3.1. Validation of resolved simulations

First, several simulations have been performed to investigate the sensitivity of the numerical results to different simulation parameters. In particular, the effects of the domain size and the grid resolution on the force and torque coefficients have been studied.

Resolving the flow field at $\Phi = 90°$ requires the highest spatial resolution [120]. To ensure that the computational grid can capture all the required details of the flow field, we performed the grid sensitivity analysis at this incidence angle. Furthermore, it is known that the effect of domain size becomes more important when the Reynolds number is decreased [6, 112, 120]. To ensure that confinement effects do not influence the numerical results at low Reynolds numbers, we consider a computational domain with $L = 80d$ for cases with $Re < 20$. For cases with higher Reynolds numbers, a domain size of $L = 40d$ is used. This choice is based on the findings of Andersson and Jiang [6].

We validate the numerical results by comparing the results of the present study with literature data for thin oblate spheroids and disks at $\Phi = 90°$. As mentioned earlier, the number of studies on thin oblate spheroids is limited. Masliyah and Epstein [93] and Pitter et al. [112] performed axisymmetric simulations to investigate the steady axial flow around spheroids with $0.05 \leq w \leq 5$ for Reynolds numbers up to $Re = 100$. Within this range of Reynolds numbers, the assumption of an axisymmetric wake is valid even for infinitely thin disks [27]. Based on the results of Pitter et al. [112], Clift et al. [30] suggested the following correlations for the steady drag coefficient of disks and low-aspect ratio oblate spheroids ($w \leq 0.05$) in the range $0.01 < Re \leq 133$:

$$C_D = \begin{cases} \dfrac{64}{\pi Re} \left[1 + 10^x \right], & \text{if } 0.01 < Re \leq 1.5, \\ \dfrac{64}{\pi Re} \left[1 + 0.138 Re^{0.792} \right], & \text{if } 1.5 < Re \leq 133, \end{cases} \tag{3.14}$$

where $x = -0.883 + 0.906 \log_{10} Re - 0.025 \left(\log_{10} Re \right)^2$. For lower Re, the expression of Oseen can be used:

$$C_D = \frac{64}{\pi Re} \left[1 + \frac{Re}{2\pi} \right] \quad \text{if } Re \leq 0.01. \tag{3.15}$$

In 2006, O'Donnell and Helenbrook [104] performed axisymmetric finite element simulations to extract the drag coefficient of crosswind oblate spheroids within the aspect ratio range $0.1 \leq w \leq 1$ at $0 \leq Re \leq 200$ and derived aspect-ratio-dependent correlations for the drag coefficient. The drag coefficients obtained from the correlation of O'Donnell and Helenbrook [104] for disks are within 2.7% of drag coefficients predicted by Pitter et al. [112].

To compare the results of different authors, we define the normalized deviation from the drag coefficient of a sphere with the same cross-sectional area as $\delta_{C_D} = 1 - \frac{C_{D,w}}{C_{D,1}}$, where $C_{D,w}$ is the drag coefficient of an oblate spheroid of aspect ratio w and $C_{D,1}$ is

Case	L	$\delta_{\max}$	r_{s}	n_{s}	γ_{s}	$n_{\mathrm{e,t}}$
$Re < 20$	$80d$	$0.02d$	$4d$	100	80	2.31e+6
$Re \geq 20$	$40d$	$0.02d$	$4d$	100	160	3.68e+6

Table 3.1.: Parameter values of the computational domains and grids.

the drag coefficient of a sphere. The latter is given by [30] :

$$
C_{D,1} = \begin{cases} \dfrac{24}{Re} \left[1 + 0.1315 Re^a \right], & \text{if } 0 < Re \leq 20, \\[2mm] \dfrac{24}{Re} \left[1 + 0.1935 Re^{0.6305} \right], & \text{if } 20 < Re \leq 260, \end{cases} \tag{3.16}
$$

with $a = 0.82 - 0.05 \log_{10} Re$. Consecutive grid refinements are performed up to the point where the maximum drag coefficient deviation from the results of O'Donnell and Helenbrook [104] is below 2%. TABLE 3.1 summarizes the chosen computational settings of the simulations. Figure 3.5 compares the dependency of δ_{C_D} on Reynolds number for spheroids with $w \leq 0.1$ based on correlations from literature [30, 104], and the results of our simulations in the range $1 \leq Re \leq 120$. Note that the Reynolds number at which the drag coefficient of a sphere equals that of a thin oblate spheroid is $Re \approx 37$. As the Reynolds number increases the relative difference between the drag coefficient of a disk and that of a 1:10 spheroid increases. The lumped force and

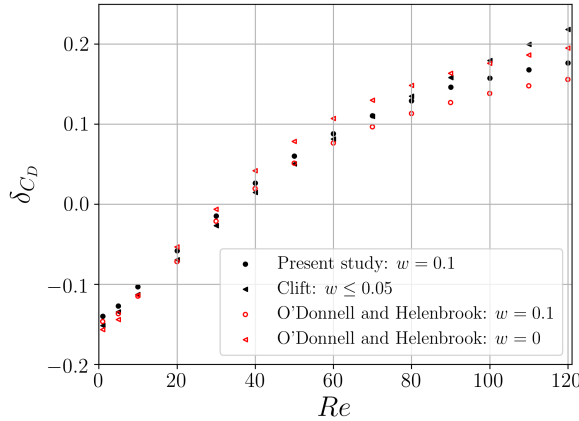**Figure 3.5.:** Deviations of drag coefficients of a 1:10 spheroid and a thin disk at $\Phi = 90°$ from the drag coefficient of a sphere. The results of the present study for a 1:10 spheroid are compared with the correlation of O'Donnell and Helenbrook [104] for a 1:10 spheroid and correlation of Clift et al. [30] for thin disks.

torque coefficients collected from the resolved simulations can be found in appendix A.

3.3.2. Aspect-ratio-specific features

Next, we illustrate the effect of the aspect ratio on the incidence-angle- and Reynolds-number-dependency of drag, lift and torque coefficients of oblate spheroids. The results of our resolved simulations for a 1:10 spheroid are compared with existing correlations for 1:5 and 2:5 spheroids. For the latter two aspect ratios, we use correlations of Zastawny et al. [154] and Sanjeevi et al. [120], respectively. In our comparison, we keep the particle volume constant and therefore define a Reynolds number based on the diameter of a volume-equivalent sphere as $Re_e = \frac{U_0 d_e}{\nu_f}$, where $d_e = w^{1/3} d$ denotes the diameter of a sphere with the same volume, and ν_f is the fluid kinematic viscosity. The volume-equivalent sphere Reynolds number, Re_e is related to the Reynolds number based on the equatorial diameter through $Re_e = w^{1/3} Re$. The obtained equivalent drag coefficient based on the cross-sectional area of the volume-equivalent sphere is $c_{D,e} = c_D w^{-2/3}$. The same relation holds for the coefficients of lift and pitching torque.

3.3.2.1. Incidence-angle dependency

In figure 3.6 the incidence-angle-dependency of the drag coefficient is compared for the three different aspect ratios. We observe that at a fixed Reynolds number within the considered range, regardless of the particle orientation, a 1:10 spheroid always has a larger drag coefficient compared to 1:5 and 2:5 spheroids. The contributions of viscous stress and pressure to the drag force on the 1:10 spheroid are compared in figure 3.7. At low incidence angles, the viscous drag is the dominant contributor to the total drag force. As the incidence angle increases the contribution of pressure increases, and at sufficiently high incidence angles pressure force has the main contribution to the total drag force. The incidence angle at which the viscous and pressure drags are equal decreases from approximately $\Phi \approx 40$ to $\Phi \approx 20$ by increasing the Reynolds number from $Re_e = 0.5$ to $Re_e = 55.7$. The larger surface area of a 1:10 spheroid compared to the one of 1:5 and 2:5 spheroids leads to a higher viscous drag at low incidence angles. At higher incidence angles the larger re-circulation region behind the 1:10 spheroid leads to a more significant pressure drop and therefore, a relatively larger pressure drag resulting in a larger total drag force.

Another issue which distinguishes the behaviour of drag coefficient for the 1:10 spheroid from that of the high-aspect-ratio spheroids is the maximum value of the drag coefficient at $Re_e = 55.7$. For a 1:10 spheroid, the maximum drag coefficient occurs at $\Phi \approx 80°$. This yields two local maxima for the drag coefficient during a $180°$ particle rotation, one at $\Phi \approx 80°$, and one at $\Phi \approx 110°$. This behaviour which is also observed for 1:4 and 2:5 spheroids at $Re_e = 100$ [120, 121], is not observed for the higher-aspect-ratio spheroids.

The effect of aspect ratio on lift and pitching torque coefficients is illustrated in figure 3.8 and figure 3.9, respectively. Both coefficients increase with decreasing the aspect ratio. It can be observed that although at low Reynolds numbers ($Re_1 = 1$) the lift coefficient of a 1:10 spheroid behaves similarly to those of 1:5 and 2:5 spheroids, at larger Reynolds numbers the incidence-angle-dependency of the lift coefficient of a 1:10 spheroid significantly deviates from those of larger aspect ratio spheroids. At

Figure 3.6.: Drag coefficient as a function of incidence angle at (a) $Re_e = 0.5$, (b) $Re_e = 27.8$, and (c) $Re_e = 55.7$.

$Re_e \approx 46$ the lift coefficient profile for a 1:10 spheroid is asymmetric with respect to $\Phi = 45°$. This is due to the fact that the onset of symmetry breaking of the wake occurs at high incidence angles for the 1:10 spheroid when the Reynolds number is lower. In contrast, for 1:5 and 2:5 spheroids, the symmetry seems to be sustained for up to $Re_e = 55.7$. A similar behaviour is observed for the pitching torque coefficient in figure 3.9.

3.3.2.2. Reynolds-number dependency

The Reynolds-number-dependency of drag, lift and torque coefficients at moderate and high incidence angles are compared in figure 3.10. Although the drag coefficient behaviour remains similar, the lift and torque coefficients of a 1:10 spheroid behave differently with Re at high incidence angles. At $\Phi \lesssim 80°$ the lift and torque coefficients of all three spheroids decrease monotonically with increasing Reynolds numbers. At higher incidence angles, however, lift and torque coefficients of a 1:10 spheroid have a local minimum at $Re_e \approx 40$. The two higher-aspect-ratio spheroids do not exhibit this behaviour.
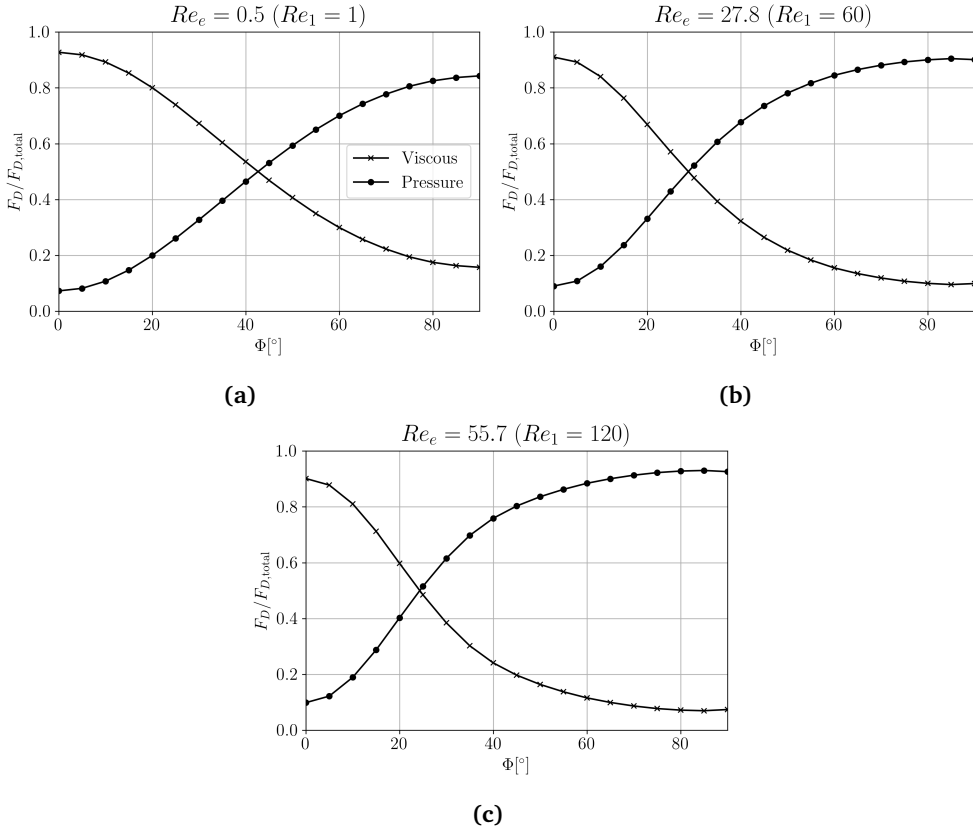
Figure 3.7.: Contributions of pressure and viscous stress to the drag coefficient at (a) $Re_e = 0.5$, (b) $Re_e = 27.8$, and (c) $Re_e = 55.7$.

To illustrate the reason behind this different behaviour at lower aspect ratios, in figure 3.11, we compare the contributions of viscous stress and pressure to the lift force and the pitching torque on a 1:10 spheroid at $\Phi = 85°$. The contribution from the pressure is dominant for both lift and pitching torque. Regardless of the incidence angle and particle Reynolds number, the viscous contribution to the pitching torque remains below 15%. The pressure force is, therefore, the dominant contributor to the pitching torque. Concerning the lift force, at low and moderate incidence angles ($\Phi < 80$), the pressure and viscous stress contributions have counteracting effects. Regardless of the incidence angle, the relative contribution of the pressure force is dominant. At $Re_e = 0.5$, for example, $|F_{L,\text{pressure}}| \approx 1.7|F_{L,\text{viscous}}|$, for all Φ. Furthermore, its contribution increases with Reynolds number up to $Re_e \approx 40$. At $Re_e \approx 40$ the viscous contribution to the lift force changes sign at $\Phi = 85°$. When the Reynolds number is increased further to $Re_e = 55.7$, at $\Phi = 85°$ the relative contribution of the pressure to the lift force is about 80%. These observations imply that the different behaviour of lift and torque coefficients for the 1:10 spheroid mostly stems from the pressure distribution at the surface of the particle.

Figure 3.12 compares the pressure field and the streamlines constructed based on the
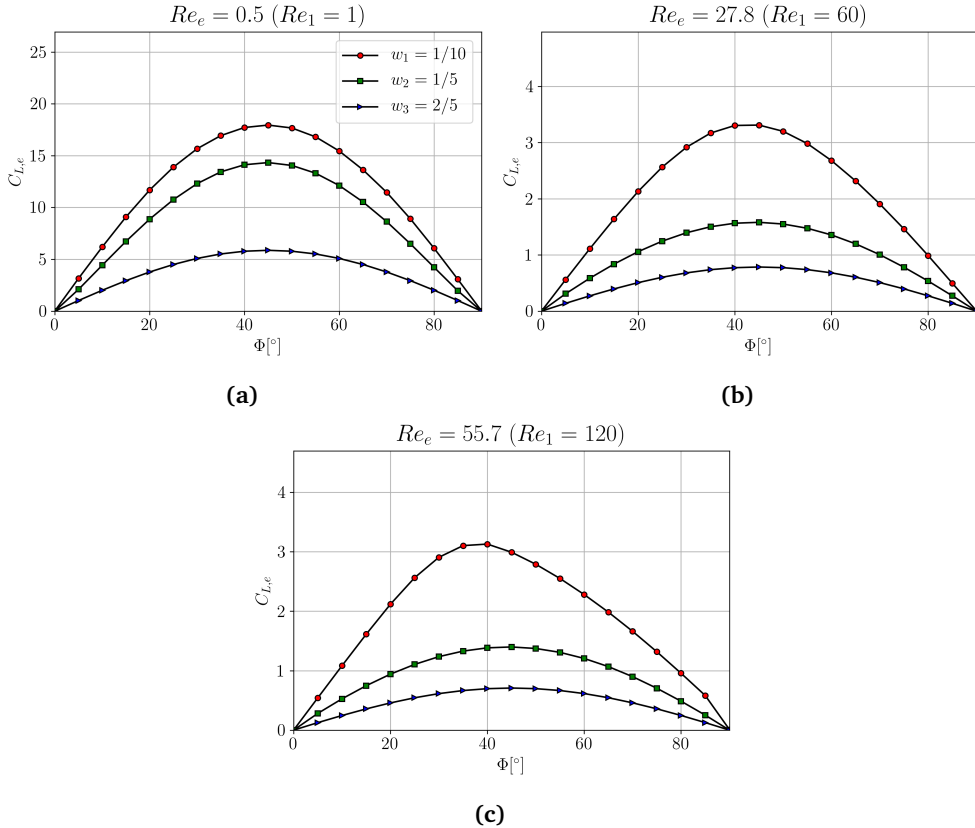
Figure 3.8.: Lift coefficient as a function of incidence angle at three different Reynolds numbers.

$x-$ and $y-$ components of velocity field at $z/d = 0$ for four different combinations of incidence angle and Reynolds number. By comparing figure 3.12 (c) and (d) corresponding to $(Re_e, \Phi) = (37.1, 85°)$ and $(Re_e, \Phi) = (55.7, 85°)$ respectively, one can observe that for these two Reynolds numbers the upstream pressure profiles at the surface of the particle at are very similar and almost symmetric in y, while for the downstream high-pressure regions this is not the case. At $Re_e = 37.1$ the recirculation region is smaller and is located closer to the particle centre. Due to the larger asymmetry of the flow field at $Re_e = 55.7$, the recirculation area is shifted in y direction farther away from the particle centre. Furthermore, the velocity in the wake just behind the particle is dominantly oriented in positive y-direction, leading to a positive viscous force in this direction. These observations explain the existence of local minima for pitching torque and lift coefficients at $\Phi = 85°$.

The different behaviors of drag, lift and pitching torque coefficients of the 1:10 spheroid observed confirm the necessity to derive shape-specific correlations for low-aspect-ratio spheroids. The dependencies for the 1:10 spheroid cannot be easily modeled by the symmetric sine-squared correlations often used in literature at higher aspect ratios. To achieve an accurate analytical correlation, the fitting procedure can be very cum-
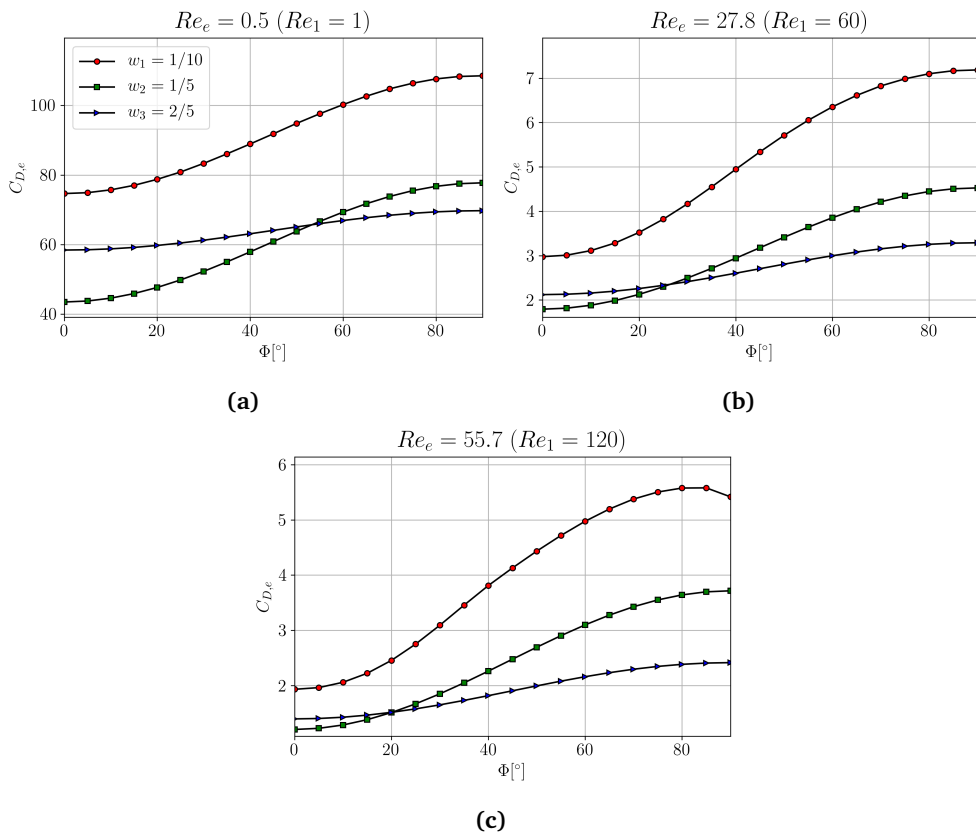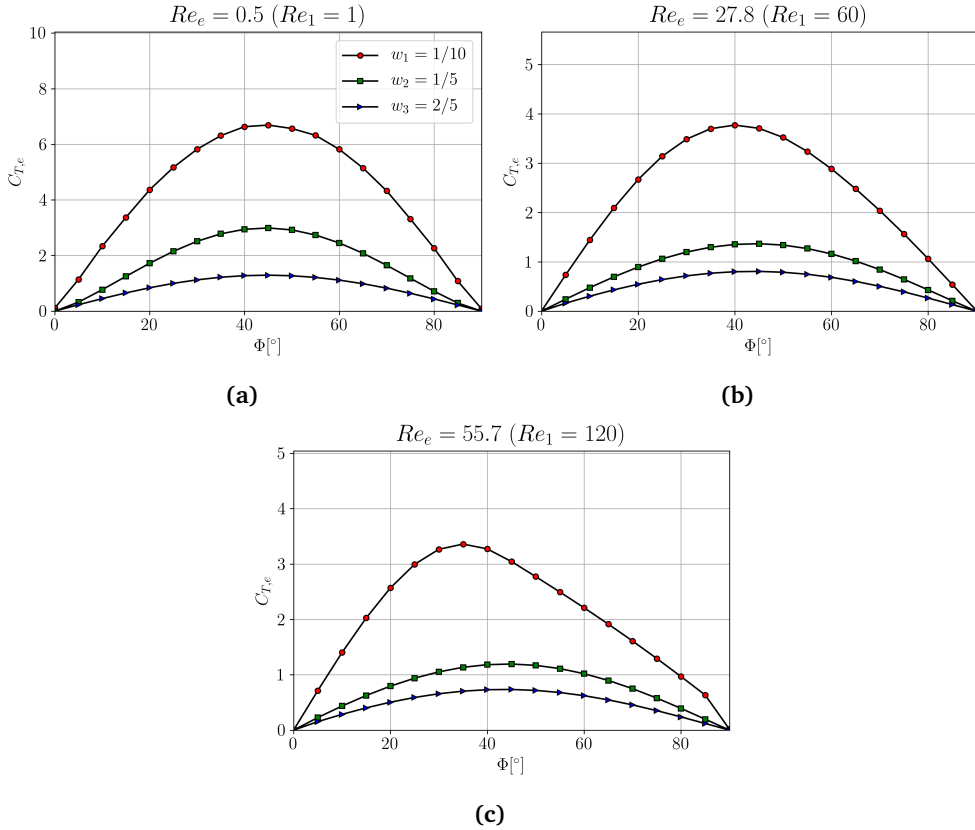
Figure 3.9.: Pitching torque coefficient as a function of incidence angle at (a) $Re_e = 0.5$, (b) $Re_e = 27.8$, and (c) $Re_e = 55.7$.

bersome as it requires introducing several additional coefficients to a correlation (as, for example, [121]). A neural network-based prediction, on the other hand, does not require such *a priori* information as it intrinsically recognizes and learns the different behaviour.

3.3.3. NN validation

The performance of the network in predicting drag, lift and pitching torque coefficients using the validation data set is illustrated in figure 3.13. The overall mean absolute error for the lift force and the pitching torque is $L_{\mathrm{mae}} = 0.0034$. The mean error for the coefficients of lift and pitching torque is below 3%. The mean error for the drag force is as low as 1.5%. Further optimization of the network may reduce these errors even more, but our results are comparable with Sanjeevi *et al.* who reported mean deviations of 1.66%, 3.50%, and 3.43% for their empirical correlations derived for drag, lift and torque coefficient of a 2:5 spheroid, respectively.

3.3.4. Testing the drag coefficient

The weights and biases obtained through the training process can be found in the supplementary material. These weights and biases are used to construct a DNN correlation according to (3.12). In this section, we test the interpolation and extrapolation performance of the DNN correlation for drag coefficient at $\Phi = 90°$ by comparing the DNN predictions with the correlation of Clift et al. [30] for thin disks. In figure 3.14 we compare our results with correlation (3.14) within the Reynolds number range of $Re \in [0, 133]$. Although the lowest Reynolds number used for the training is $Re = 1$, it can be seen that the DNN model can very well capture the Stokes regime ($Re << 1$) behaviour of the drag coefficient described by (3.15).

3.3.5. Application to a settling problem

In this section, we employ the DNN-based drag correlation in a point-particle simulation of the buoyancy-driven motion of a 1:10 disk in a quiescent paramagnetic liquid in a non-uniform magnetic field. The buoyancy-driven motion of disks and ellipsoidal particles in viscous liquids has extensively been explored [12, 43, 152]. It is well known that the buoyancy-driven motion of disk-shaped particles can be fully described by three parameters, namely the mass density ratio ρ_p/ρ_f, the aspect ratio w and the Galileo number $Ga = \sqrt{|1 - \rho_p/\rho_f| g d_p^3}/\nu_f$, where ρ_f and ρ_p denote the mass densities of the fluid and particle respectively, ν_f is the fluid kinematic viscosity, and g is the magnitude of gravitational acceleration [12, 30, 152]. Depending on the combination of these three non-dimensional parameters, four main regimes for the settling motion of a disk are identified. At low Ga numbers, where viscous effects are large enough, a disk falls broadside along a straight vertical path. As inertial effects increase, a disk can display a fluttering motion, and as the inertia further increases, tumbling and even full rotations may occur.

By incorporating a magnetically responsive liquid and a vertical magnetic field gradient, a non-linear pressure is generated inside the liquid. Once released in the liquid at $\Phi = 90°$, a disk with an adequately chosen mass density, stably levitates at the height where the gravity force cancels the net buoyancy force acting on the particle. The existence of a stable equilibrium point in such a configuration, makes the prediction of the time-dependent trajectory of a particle a good benchmark case for testing the DNN correlation within the Reynolds number range of $Re \in [0, 10]$.

The magnetically-induced non-linear pressure field inside the liquid leads to a position-dependent net buoyancy force on an immersed particle. The magnitude of this buoyancy force is dependent on the local gradient of the magnetic field, ∇H, and the magnetization of the liquid, M. In the experiment, the gradient of the generated magnetic field is vertical, $\frac{\partial H}{\partial x} = \frac{\partial H}{\partial z} = 0$, so that the combined gravitational and buoyancy force is

$$F_{\text{BG}} = (\rho_{\text{f,a}} - \rho_{\text{p}})V_i g. \qquad (3.17)$$

Here, $\rho_{\text{f,a}}$ is the so-called "apparent mass density" of the magnetic liquid fluid defined

as

$$\rho_{f,a}(y) = \rho_f - \frac{\mu_0}{gy} \int_0^y M \frac{dH}{dy} dy, \qquad (3.18)$$

where μ_0 is the permeability of vacuum, and g is the magnitude of gravitational acceleration. For a paramagnetic liquid at relatively low magnetic field strengths, the magnitude of the magnetization is a linear function of the magnitude of the magnetic field strength, $M = \chi H$, where χ denotes the magnetic susceptibility of the liquid. For small particles, the integral in (3.18) can be approximated by

$$\rho_{f,a}(y) \approx \rho_f - \left(\frac{\mu_0}{g}\right) M \frac{dH}{dy}. \qquad (3.19)$$

Once a particle with mass density ρ_p is released in the fluid at initial height y_0, it travels to a height at which $\rho_{f,a}(y) = \rho_p$.

We employ a one-way coupled point-particle model where the effect of the particle motion on the fluid is assumed to be negligible. The motion of a the particle is described by solving the translational equation of motion of the particle. An angular momentum equation is not solved for the following reason: In the considered magneto-fluidic system an apparent Galileo number can be defined as $\mathrm{Ga_a} = \sqrt{|1 - \rho_p/\rho_{f,a}|g d_p^3}/\nu_f$. In the present configuration with $\rho_p = 1.434 \times 10^3$ kg/m^3, the maximum apparent Galileo number of a particle remains below 70. The motion of a 1:10 disk with $\rho_p/\rho_f \approx 1$ and $\mathrm{Ga_a} \leq 70$ falling at $\Phi = 90°$ is steady and follows a straight vertical path and the particle does not undergo any rotational motion. Hence, the governing equations of the particle motion reduces to a scalar system of the form

$$\begin{aligned} \frac{dy}{dt} &= v, \\ \frac{dv}{dt} &= \frac{1}{m_p} \sum F, \end{aligned} \qquad (3.20)$$

where $\sum F$ is the sum of all forces stemming from different fluid-particle hydrodynamic interactions and the gravity force. The relevant forces in the motion of almost neutrally buoyant particles in viscous liquids are the steady drag force F_D, the combined buoyancy and gravity force F_{BG}, the history force, F_H and the added mass force, F_A, so that

$$\sum F = F_D + F_{BG} + F_H + F_A. \qquad (3.21)$$

The steady drag force is given by

$$F_D = \frac{1}{2} C_D \rho_p v^2 A_p, \qquad (3.22)$$

where C_D is the steady drag coefficient, and $A_p = \pi d^2/4$ is the cross sectional area of the particle with equatorial diameter d.

For history force and added mass force, we follow the expressions derived by Lai and Mockros [83] for a spheroid moving parallel to its symmetry axis. If we neglect the

finite Reynolds number effects on the history kernel, the history force reads

$$F_{\mathrm{H}} = -6\Delta_{\mathrm{H}}\left(\pi\rho_{\mathrm{f}}\mu\right)^{1/2} a^2 \int_{-\infty}^{t} \frac{\frac{dv}{d\tau}}{(t-\tau)^{1/2}} d\tau, \qquad (3.23)$$

where the history force coefficient, Δ_{H}, for a particle with aspect ratio w reads

$$\Delta_{\mathrm{H}} = \left[\frac{4(1-w^2)}{3\left(\left[(1-2w^2)\arccos\left(w/\sqrt{1-w^2}\right)\right]+w\right)}\right]^2. \qquad (3.24)$$

The added mass force is given by

$$F_{\mathrm{AM}} = -\frac{1}{2}\Delta_{\mathrm{A}}\rho_{\mathrm{f}}V\frac{dv}{dt}, \qquad (3.25)$$

where Δ_{A} is the added mass coefficient given by

$$\Delta_{\mathrm{A}} = \frac{2\left[w\cos^{-1}w - \sqrt{1-w^2}\right]}{w^2\sqrt{1-w^2} - w\cos^{-1}w}. \qquad (3.26)$$

For a spheroid with $w = 0.1$, equations (3.25) and (3.26) yield, respectively, $\Delta_{\mathrm{A}} = 12.4$ and $\Delta_{\mathrm{H}} = 0.7$.

To obtain the temporal evolution of the vertical particle position, system (3.20) is discretized using an explicit Euler scheme. For numerical integration of the Basset history term, we use the method of Van Hinsberg et al. [144], where the history kernel is split into a "window" kernel and a "tail" kernel. The window kernel is approximated by a trapezoidal rule, and the tail kernel is approximated by a sum of exponential functions. We test the NN-based drag model by comparing the particle trajectory based on the DNN-based drag model, $C_D(Re, \Phi = 90°)$ with the experimentally obtained trajectory. An experimental setup was designed which enables the investigation of levitation motion of single non-spherical particles in a paramagnetic liquid subject to a vertical magnetic field gradient. The vertical position of the particle is recorded by a 3D particle tracking velocimetry technique. Measurements are performed in a $15 \times 15 \times 15\ \mathrm{cm}^3$ cubic container filled with a stable aqueous solution of $\mathrm{MnCl_2}$. The container is located on a magnet that generates the desired magnetic field in the form of (3.27). Two cameras record the particle trajectories through two perpendicular sidewalls of the tank. The particle considered for the experiments is a disk made of unplasticized polytetrafluorethylene (PVC-U) $\rho_{\mathrm{p}} = 1434\ \mathrm{kg/m^3}$. A schematic of the experimental setup is shown in figure 3.15.

The considered magnet generates a magnetic field that has a magnitude decaying exponentially with the vertical distance from the magnet surface, y:

$$H(y) = H_0 e^{-\pi y/p}, \qquad (3.27)$$

with $H_0 = 422\ \mathrm{kA/m}$ and pole size $p = 0.118\ \mathrm{m}$. The magnetic field strength and the apparent mass density of the liquid according to (3.19) are plotted as functions of y in figure 3.16. TABLE 3.2 summarizes the parameters of the considered configuration.

Table 3.2.: Physical parameters of the magnetic levitation setup.

ρ_{p} [kg/m^3]	1.434×10^3
d [mm]	5
b [mm]	0.5
ρ_{f} [kg/m^3]	1.403×10^3
μ_{f} [kgm/s]	5.54×10^{-3}
χ_{f}	7×10^{-4}
L [m]	0.15
p [m]	0.1181
H_0[kA/m]	422

A particle with mass density $\rho_p = 1.02\rho_f$ stably levitates at $y = 48.7$ mm. Figure 3.17 compares the numerically and experimentally obtained trajectories of the particle released at $y_0 = 104.2$ mm. The experimental trajectory is obtained by averaging the results of three independent experiments. The error bars correspond to the standard deviation of these three measurements. The maximum particle Reynolds number during the levitation motion is $Re = 7.6$. Very good agreement is observed between the experimental trajectory and the one obtained with the point-particle simulation based on the DNN-based drag correlation. This observation shows the promising performance of the DDN model in predicting the drag coefficient of a 1:10 disk.
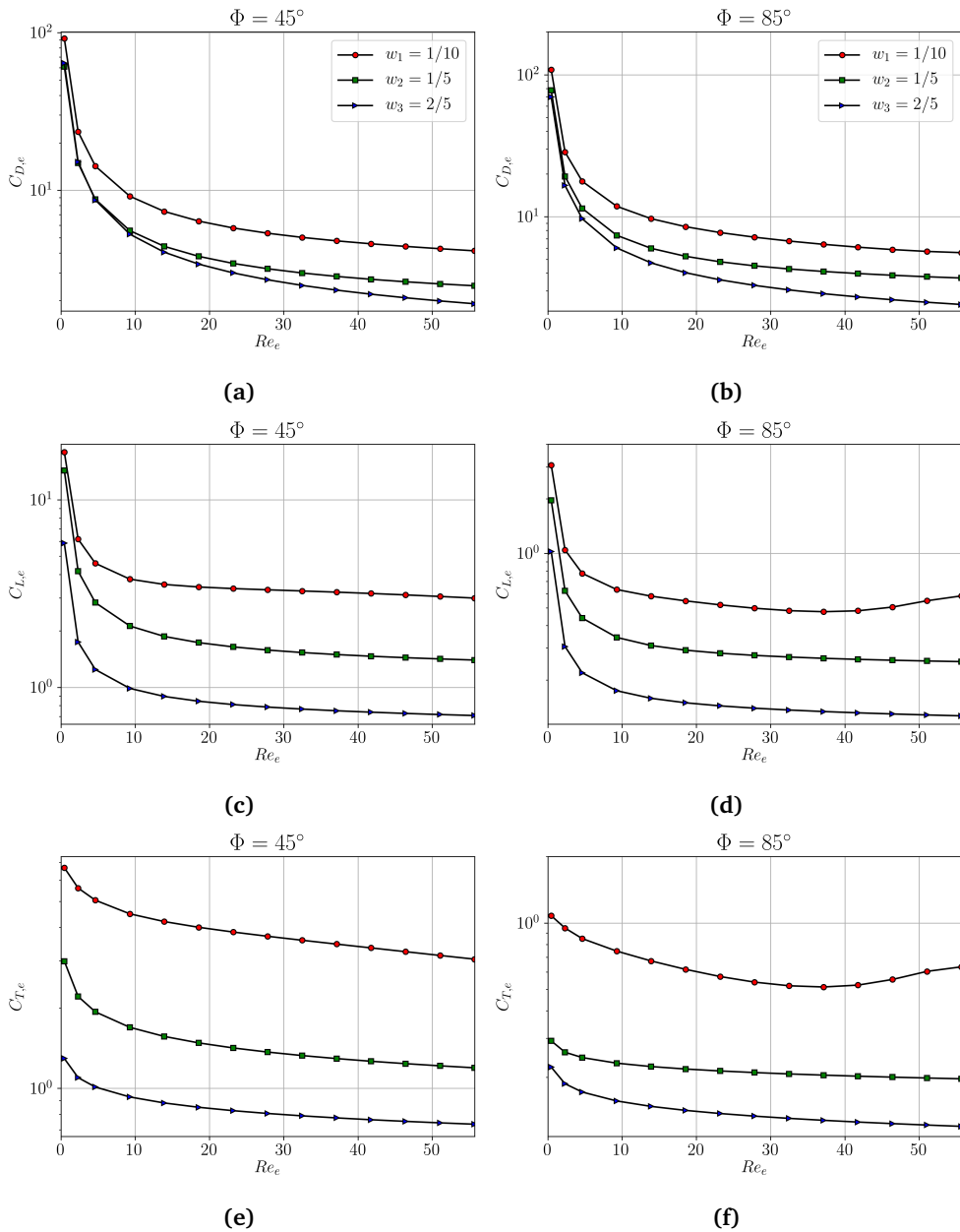
Figure 3.10.: Coefficients of (a), (b) drag, (c), (d) lift and (c), (d) pitching torque as a functions of Reynolds number at moderate (top) and high (bottom) incidence angles.
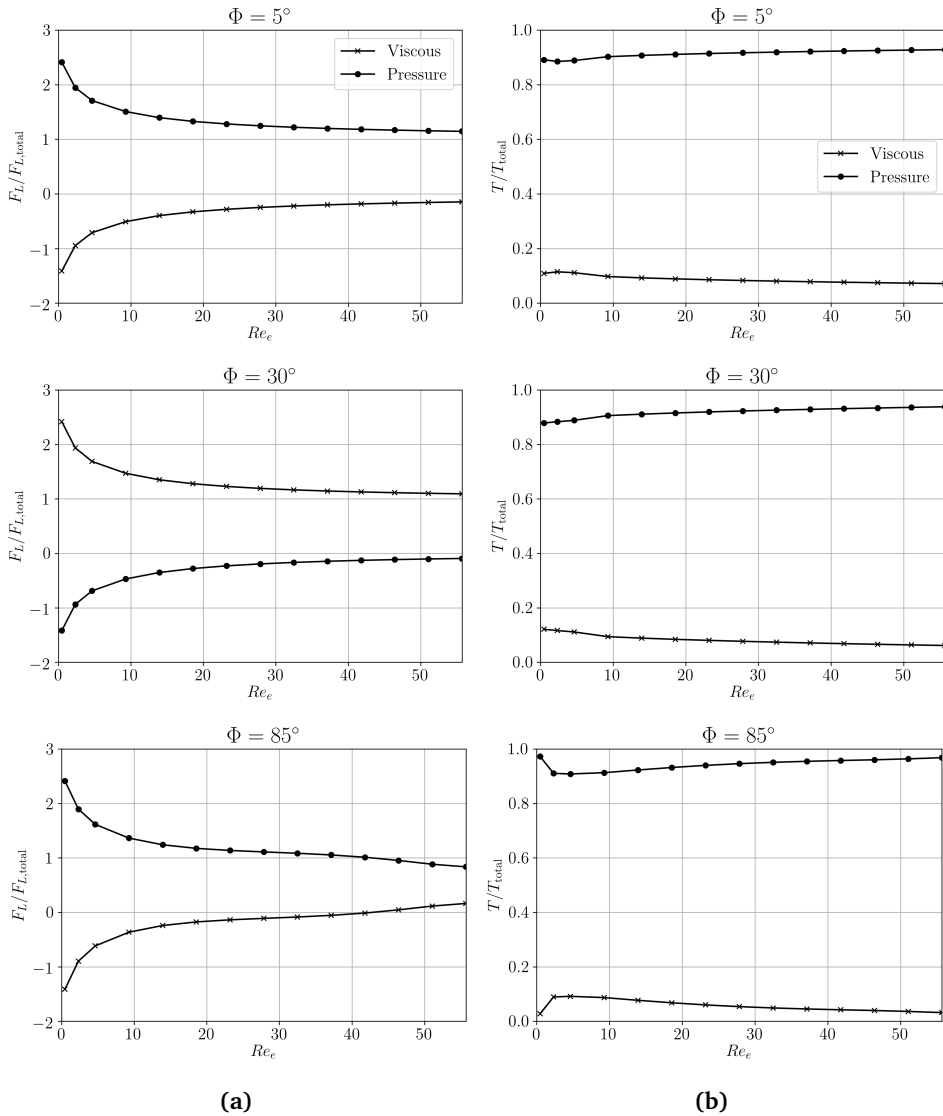
Figure 3.11.: Viscous and pressure contributions to the lift force **(a)** and pitching torque **(b)** on a 1:10 spheroid at (top) $\Phi = 5°$, (middle) $\Phi = 30°$ and (bottom) $\Phi = 85°$.

(a) $(Re_e, \Phi) = (37.1, 45°)$

(b) $(Re_e, \Phi) = (55.7, 45°)$

(c) $(Re_e, \Phi) = (37.1, 85°)$

(d) $(Re_e, \Phi) = (55.7, 85°)$
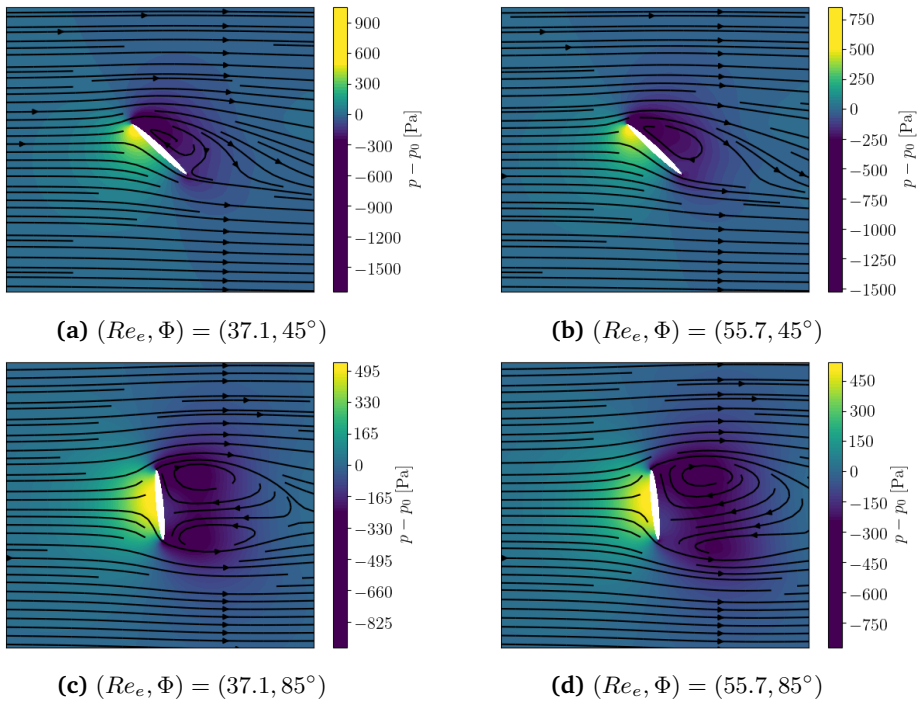
Figure 3.12.: Pressure field and streamline pattern in the centre plane $z = 0$ for the flow around a 1:10 spheroid at different orientations and Reynolds numbers.

(a) Drag

(b) Lift
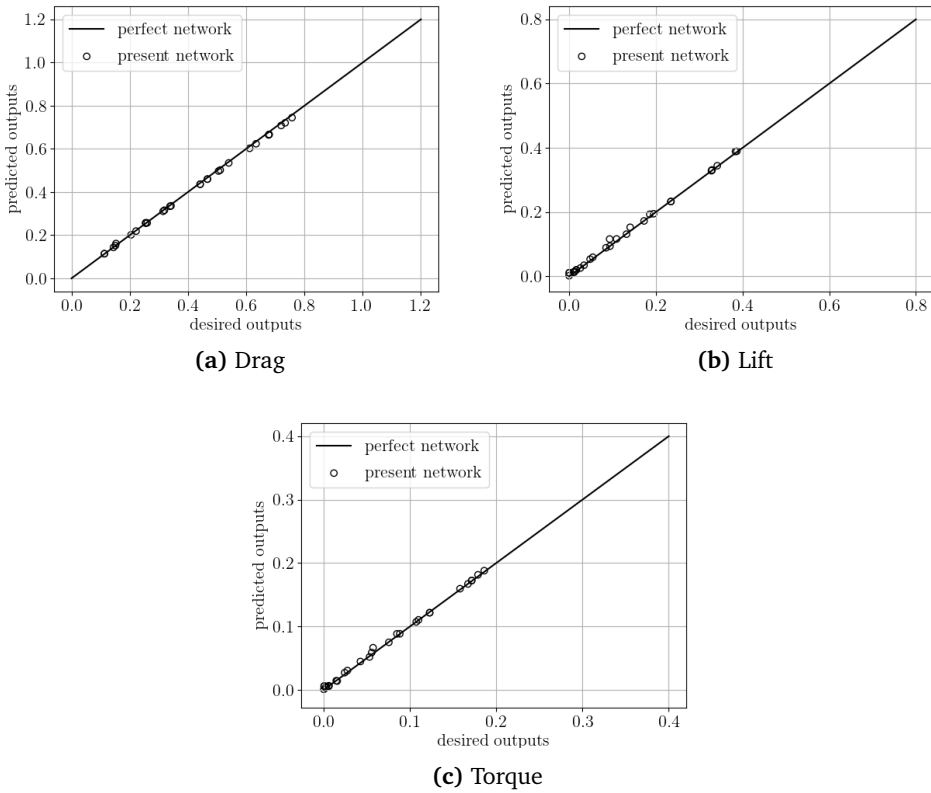
(c) Torque

Figure 3.13.: Validation of the neural network prediction for drag, lift and torque coefficients.
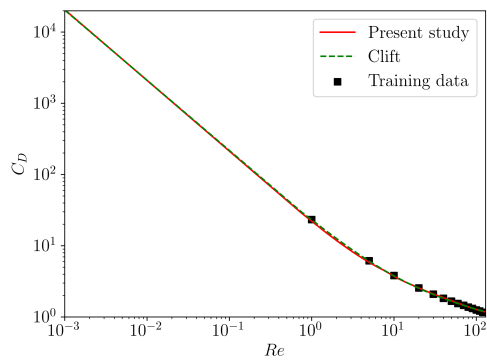
Figure 3.14.: Reynolds-number-dependency of the steady drag coefficient of 1:10 spheroid at $\Phi = 90°$ predicted by the DNN model is compared to correlation (3.14). The dashed line represents the correlation of Clift et al. [30] and ■ indicates the training data points.
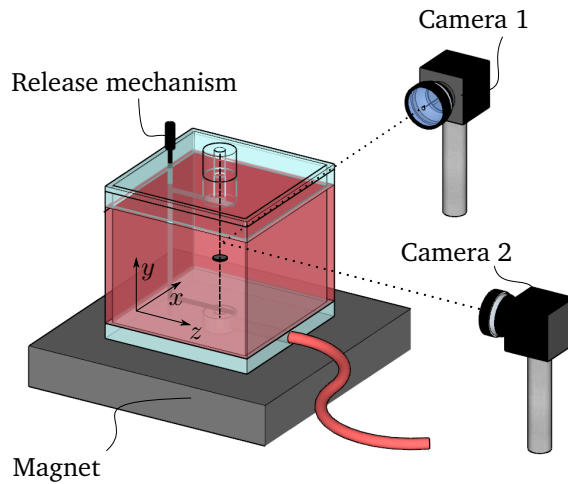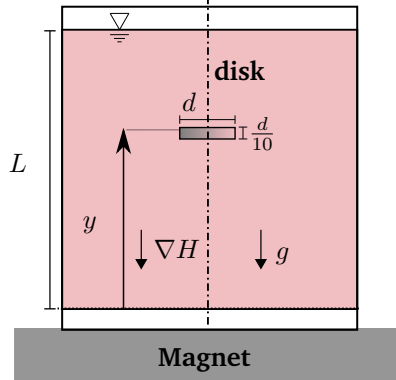
Figure 3.15.: (a) A sketch of the experimental setup. A tank filled with manganese(II) chloride solution is placed on top of a magnet. The particle is released from the top by a rotating release mechanism. Two cameras record the motion of the released particle. (b) Schematic side view.
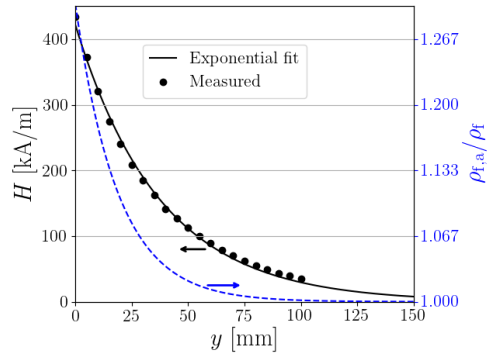
Figure 3.16.: Magnetic field strength and effective mass density on a vertical line passing through the center of the tank. A particle with $\rho_\mathrm{p}/\rho_\mathrm{f} = 1.02$ stably levitates at $y = 48.7$ mm.
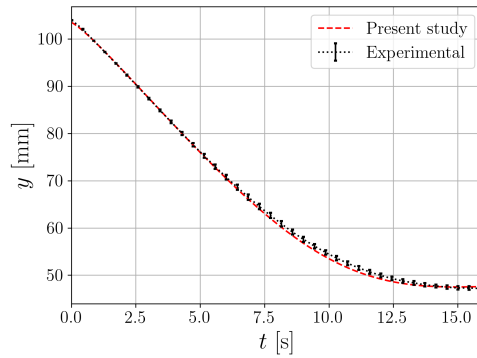
Figure 3.17.: The vertical position of a 1:10 disk in a magnetized paramagnetic liquid as a function time. The dashed line corresponds to the numerical solution of (3.20) with the DNN-based drag coefficient. The experimentally obtained trajectory is indicated by the dotted line.

3.4. Conclusions

Predicting steady hydrodynamic interactions of non-spherical particles becomes more challenging as the particle non-sphericity increases. The complexity of the input-output relations on the one hand and the increased number of input parameters, on the other hand, make the development of empirical force and torque models very difficult. In this study, we showed how statistical learning can serve as a versatile and robust tool for predicting hydrodynamic interactions of non-spherical particles with a viscous liquid. A machine learning approach is proposed to create models for the Reynolds-number- and incidence-angle-dependent steady drag, lift and pitching torque coefficient of a 1:10 oblate spheroid. A feed-forward deep neural network is trained and validated using a data set generated by resolved simulations at 261 different combinations of particle Reynolds number and incidence angle.

The effect of aspect ratio on the dependency of drag, lift and pitching torque on the particle Reynolds number and incidence angle is illustrated, and advantages of a DNN-based correlation method compared to conventional curve-fitting methods are pointed out. It is shown that although the effect of aspect ratio on the behaviour of the drag force is small, the lift and torque coefficient at low aspect ratios behave very differently than at higher aspect ratios. The proposed DNN model automatically "learns" the input-output dependencies and can serve as an accurate meta-model in point-particle simulations. The main advantage of DDN-based models is that the correlation procedure does not require *a priori* information about the dependency of an output variable on an input variable, a necessary condition for curve fitting methods. Furthermore, DNN models are applicable in cases of large parameter space without introducing unsatisfactory high biases.

We tested the performance of the constructed DNN model in a point-particle simulation of a settling problem. The agreement between the numerical and experimental data proved the capability of the DNN model in interpolating and extrapolating a learned relationship.

In this work, we considered a single aspect ratio at $0 \leq Re \leq 120$. Data for other aspect ratio or Reynolds number ranges can be used as input in a straightforward manner to extend the model to other aspect ratios and Reynolds numbers. The DDN-based correlation procedure presented in this study can be used to predict other fluid-particle hydrodynamic interactions such as velocity-gradient induced lift, and transient effects such as history and added mass forces. Once a new database is generated, a model can be extended by just adding additional input neurons and training the network with the new data set.

3.5. Acknowledgments

mus+.

3.A. Tabulated data

The collected lumped data for steady drag, lift and pitching torque coefficients are given in TABLE 3.3, 3.4 and 3.5 respectively. The coefficients are based on the cross sectional area of the volume-equivalent sphere.

Drag	0.46	2.32	4.64	9.28	13.92	18.57	23.21	27.85	32.49	37.13	41.77	46.42	51.06	55.7
0.000	74.660	18.130	10.460	6.250	4.710	3.880	3.350	2.980	2.700	2.480	2.300	2.160	2.040	1.930
5.000	74.920	18.210	10.510	6.300	4.750	3.910	3.380	3.010	2.730	2.510	2.340	2.190	2.070	1.960
10.000	75.730	18.470	10.690	6.430	4.870	4.030	3.490	3.110	2.830	2.610	2.430	2.290	2.170	2.060
15.000	77.020	18.870	10.980	6.640	5.060	4.210	3.660	3.280	3.000	2.780	2.600	2.450	2.330	2.220
20.000	78.760	19.420	11.360	6.940	5.330	4.460	3.910	3.520	3.240	3.010	2.830	2.690	2.560	2.460
25.000	80.850	20.080	11.830	7.300	5.660	4.770	4.210	3.820	3.530	3.310	3.130	2.980	2.860	2.750
30.000	83.340	20.860	12.370	7.720	6.030	5.130	4.560	4.170	3.880	3.650	3.470	3.320	3.200	3.090
35.000	86.080	21.710	12.970	8.180	6.450	5.530	4.950	4.550	4.250	4.020	3.840	3.690	3.560	3.460
40.000	88.920	22.600	13.600	8.670	6.890	5.950	5.360	4.950	4.640	4.410	4.220	4.060	3.920	3.810
45.000	91.850	23.500	14.230	9.170	7.340	6.370	5.760	5.340	5.020	4.780	4.580	4.410	4.260	4.130
50.000	94.840	24.420	14.870	9.660	7.780	6.780	6.150	5.710	5.380	5.120	4.900	4.720	4.570	4.430
55.000	97.620	25.280	15.480	10.130	8.200	7.170	6.510	6.050	5.700	5.430	5.200	5.010	4.850	4.720
60.000	100.240	26.080	16.040	10.560	8.580	7.520	6.840	6.350	5.990	5.700	5.470	5.270	5.110	4.970
65.000	102.660	26.810	16.550	10.940	8.910	7.820	7.110	6.610	6.230	5.930	5.690	5.490	5.330	5.200
70.000	104.780	27.450	16.990	11.270	9.200	8.070	7.350	6.830	6.430	6.120	5.870	5.670	5.510	5.380
75.000	106.400	27.940	17.340	11.530	9.410	8.260	7.520	6.990	6.580	6.250	6.000	5.790	5.630	5.500
80.000	107.630	28.310	17.590	11.720	9.580	8.410	7.650	7.100	6.680	6.340	6.070	5.860	5.700	5.580
85.000	108.330	28.520	17.740	11.840	9.680	8.500	7.730	7.170	6.730	6.390	6.100	5.860	5.690	5.580
90.000	108.530	28.590	17.790	11.870	9.700	8.520	7.750	7.190	6.750	6.390	6.100	5.840	5.620	5.420

Table 3.3.: Coefficient of drag $C_{D,e}$. Left most column: incidence angle, top row: Reynolds number, Re_e, center: values of $C_{D,e}$.

Lift	0.46	2.32	4.64	9.28	13.92	18.57	23.21	27.85	32.49	37.13	41.77	46.42	51.06	55.7
0.000	$1\cdot10^{-2}$	0.000	0.000	0.000	0.000	0.000	0.000	0.000	0.000	0.000	0.000	0.000	0.000	0.000
5.000	3.160	1.100	0.810	0.660	0.610	0.580	0.570	0.560	0.560	0.550	0.550	0.550	0.540	0.540
10.000	6.200	2.150	1.600	1.290	1.200	1.150	1.130	1.110	1.100	1.090	1.090	1.090	1.080	1.080
15.000	9.090	3.150	2.330	1.890	1.760	1.690	1.660	1.640	1.630	1.620	1.620	1.610	1.610	1.610
20.000	11.690	4.050	3.000	2.440	2.270	2.190	2.150	2.130	2.120	2.110	2.110	2.110	2.110	2.120
25.000	13.890	4.800	3.560	2.910	2.720	2.630	2.590	2.570	2.560	2.550	2.550	2.560	2.560	2.560
30.000	15.660	5.410	4.020	3.290	3.070	2.980	2.940	2.920	2.910	2.900	2.900	2.900	2.910	2.910
35.000	16.930	5.840	4.340	3.560	3.340	3.240	3.200	3.170	3.160	3.140	3.140	3.130	3.120	3.100
40.000	17.710	6.100	4.530	3.730	3.500	3.390	3.340	3.310	3.280	3.250	3.220	3.190	3.160	3.130
45.000	17.950	6.170	4.590	3.780	3.540	3.430	3.360	3.310	3.270	3.220	3.170	3.110	3.050	2.990
50.000	17.670	6.060	4.500	3.710	3.470	3.350	3.270	3.200	3.130	3.060	2.990	2.920	2.850	2.790
55.000	16.810	5.750	4.280	3.520	3.290	3.160	3.070	2.980	2.900	2.820	2.740	2.670	2.610	2.550
60.000	15.440	5.280	3.920	3.230	3.000	2.870	2.770	2.680	2.590	2.510	2.440	2.380	2.330	2.280
65.000	13.630	4.650	3.460	2.840	2.630	2.510	2.410	2.320	2.240	2.170	2.110	2.060	2.020	1.980
70.000	11.460	3.900	2.900	2.370	2.190	2.080	1.990	1.910	1.840	1.780	1.740	1.710	1.690	1.660
75.000	8.900	3.030	2.250	1.840	1.690	1.600	1.530	1.460	1.410	1.380	1.350	1.340	1.330	1.320
80.000	6.070	2.060	1.530	1.250	1.150	1.090	1.030	0.990	0.960	0.940	0.930	0.940	0.950	0.960
85.000	3.070	1.040	0.780	0.630	0.580	0.550	0.520	0.500	0.480	0.480	0.480	0.500	0.550	0.580
90.000	$1\cdot10^{-2}$	0.000	0.000	$1\cdot10^{-2}$	0.000	0.000	0.000	0.000	0.000	0.000	0.000	0.000	0.000	0.000

Table 3.4.: Coefficient of lift $C_{L,e}$. Left most column: incidence angle, top row: Reynolds number, Re_e, center: values of $C_{L,e}$.

Torque	0.46	2.32	4.64	9.28	13.92	18.57	23.21	27.85	32.49	37.13	41.77	46.42	51.06	55.7
0.000	$3\cdot10^{-2}$	$1\cdot10^{-2}$	0.000	0.000	0.000	0.000	0.000	0.000	0.000	0.000	0.000	0.000	0.000	0.000
5.000	1.140	0.980	0.890	0.810	0.780	0.760	0.740	0.740	0.730	0.720	0.720	0.720	0.720	0.710
10.000	2.330	1.940	1.760	1.600	1.530	1.490	1.460	1.440	1.430	1.420	1.410	1.410	1.400	1.400
15.000	3.370	2.830	2.570	2.330	2.220	2.160	2.120	2.090	2.070	2.060	2.050	2.040	2.030	2.030
20.000	4.360	3.640	3.300	2.990	2.850	2.760	2.710	2.670	2.640	2.620	2.600	2.590	2.580	2.570
25.000	5.170	4.330	3.920	3.550	3.370	3.270	3.190	3.140	3.100	3.070	3.050	3.030	3.010	2.990
30.000	5.820	4.890	4.420	3.980	3.770	3.640	3.550	3.490	3.430	3.390	3.350	3.320	3.290	3.270
35.000	6.310	5.290	4.780	4.290	4.050	3.900	3.790	3.700	3.630	3.560	3.510	3.460	3.410	3.360
40.000	6.630	5.550	5.000	4.460	4.200	4.020	3.880	3.770	3.680	3.590	3.500	3.420	3.350	3.270
45.000	6.690	5.620	5.060	4.500	4.210	4.000	3.840	3.710	3.580	3.460	3.350	3.250	3.140	3.040
50.000	6.570	5.520	4.970	4.400	4.090	3.870	3.680	3.520	3.370	3.230	3.100	2.980	2.870	2.770
55.000	6.320	5.280	4.730	4.160	3.850	3.610	3.410	3.240	3.070	2.930	2.800	2.680	2.580	2.490
60.000	5.820	4.860	4.340	3.810	3.500	3.260	3.060	2.880	2.720	2.590	2.470	2.370	2.280	2.210
65.000	5.150	4.290	3.830	3.350	3.060	2.830	2.640	2.480	2.340	2.220	2.130	2.050	1.980	1.910
70.000	4.320	3.600	3.210	2.790	2.540	2.340	2.180	2.040	1.930	1.840	1.770	1.710	1.660	1.610
75.000	3.310	2.790	2.490	2.160	1.960	1.800	1.670	1.560	1.490	1.430	1.390	1.360	1.330	1.290
80.000	2.270	1.910	1.700	1.470	1.330	1.220	1.130	1.060	1.010	0.990	0.980	0.980	0.980	0.970
85.000	1.080	0.950	0.850	0.750	0.670	0.620	0.570	0.540	0.520	0.510	0.520	0.550	0.600	0.630
90.000	$8\cdot10^{-2}$	$2\cdot10^{-2}$	$1\cdot10^{-2}$	$2\cdot10^{-2}$	$2\cdot10^{-2}$	$1\cdot10^{-2}$	$1\cdot10^{-2}$	$1\cdot10^{-2}$	$1\cdot10^{-2}$	$1\cdot10^{-2}$	$1\cdot10^{-2}$	$1\cdot10^{-2}$	$1\cdot10^{-2}$	$1\cdot10^{-2}$

Table 3.5.: Coefficient of torque $C_{T,e}$. Left most column: incidence angle, top row: Reynolds number, Re_e, center: values of $C_{T,e}$.

4. Dynamics of spheroidal particles in paramagnetic liquids

In this chapter, we present a PP-DNS approach for modelling the dynamics of ellipsoidal particles in flows of magnetic fluids exposed to a non-uniform magnetic field. The numerical model discussed in this chapter is based on the framework presented in chapter 2.

4.1. Introduction

The buoyancy-driven motion of particles in magnetized liquids is of practical importance in magnetic density separation (MDS) systems. MDS uses a magnetic fluid magnetized by a specifically designed magnetic field to separate a mixture of particles based on the mass densities of its sub-populations. The MDS technique has been successfully applied to separate diamond from gangue minerals [148], and to sort non-magnetic metals [75, 129, 136], toxic wastes [103], and vegetable seeds [35]. More recently, MDS is used as an efficient technique for separating end-of-life electronic and plastic waste [14, 88, 100, 114, 156].

Design optimization of MDS systems requires a thorough understanding of the interaction between a magnetic field and particle-laden flow of an opaque magnetic liquid. Numerical simulations of particle-laden flows of magnetic liquids can serve as versatile tools to optimize of MDS processes. The development of accurate and efficient numerical algorithms for modelling particle-laden flows of magnetically responsive fluids is therefore of great industrial interest. In the numerical investigation of the collective motion of particles in magnetized liquids, one should consider the combination of fluid-magnetic field, fluid-particle, and particle-particle interaction mechanisms, that makes the problem at hand complicated, and the required models complex. In chapter 3, we presented a numerical framework for investigating the magneto-Archimedes separation of spherical particles in paramagnetic liquids. We showed that the incorporation of history effects is important for the prediction of the motion of particles. Moreover, application of the numerical model to large MDS systems showed that particle-particle interactions have a negative effect on the separation performance and cannot be disregarded even at volume fractions as low as 0.02. Two-way coupling effects, on the other hand, were shown to have a small impact on the dynamics of spherical particles.

The assumption of spherical particle shape is a common practice in order to reduce the complexity of the mathematical models to study particle-laden flows. In most of the industrial applications involving non-spherical particles, however, this assumption might result in large errors. It is well-known that particle shape can significantly influence the dynamical behaviour of particles in a flow [11, 29, 99, 149, 150]. The MDS process is not an exception in this respect. In most of the practical MDS applications, particles are not spheres. In MDS of end-of-life plastic, for example, input particles

are produced through a shredding process which results in highly anisotropic, flake-shaped particles [14]. This necessitates the development of a more complex numerical framework to model the motion of non-spherical particles in MDS systems.

The treatment of non-spherical particles is mathematically much more complicated because of multiple reasons. First, as shown in Chapter 2, particle non-sphericity complicates the interactions between the particles and the surrounding fluid and introduces new influence parameters in models for these interactions. As the particle nonsphericity increases, the coupling between the linear and angular motions of particles becomes stronger. Second, the particle-particle collision response and its influence on the post-collision motion of a particle is strongly influenced by the particle shape. Moreover, compared to spheres, detection of contact points and the time of impact of non-spherical particles is much more computationally demanding [10, 68, 98, 142]. Therefore, efficient and accurate models should be incorporated for collision detection as well as for the collision response of non-spherical particles in many-particle systems. Third, in studying the motion of particles in magnetized liquids, particle non-sphericity can introduce new magnetically induced fluid-particle interactions which are absent in case of spherical particles, since the moment of the magnetic buoyancy force can be nonzero for immersed non-spherical particles. This further complicates the coupled rotational and translational motion of non-spherical particles in MDS systems.

Jeffery [70] and Brenner [20, 21] derived expressions for drag forces and torques on ellipsoidal particles under the creeping flow condition. Later Gallily and Cohen [48] studied the effect of particle rotation on sedimentation of ellipsoidal particles in a gravitational field. Most of the point-particle simulations of non-spherical particles in laminar and turbulent flows use such creeping flow force and torque models to describe the motion of the particles (see, for example, [5, 99, 133, 155]). The small size of the particles compared to the smallest flow scales justifies the incorporation of such models. For larger particle sizes or larger Reynolds numbers, incorporation of such models introduces large errors due to the significance of inertial effects. More recently shape-specific correlations are derived for Reynolds-number- and orientation-dependent force and torque coefficients of nonspherical particles beyond the Stokes regime [47, 106, 109, 121, 154]. These correlations are used in simulations where the creeping flow assumption does not hold [2, 140, 147]. These studies, however, mostly address gas-solid flows where unsteady interactions and rotational resistance torques are disregarded. In fluid-solid flows in MDS applications, such interactions can be are generally more important [91].

In this chapter, we present an Euler-Lagrange framework to model flows of magnetized liquids laden with non-spherical particles. Our numerical framework is based on the point-particle approach of Tajfirooz et al. [139] for spherical particles presented in chapter 2. The kinematics and dynamics of the motion of ellipsoidal particles in magnetically responsive liquids are described in a Lagrangian manner, and new collision detection and response models are incorporated to capture the inter-particle and particle-wall interactions of ellipsoidal particles. Force and torque models derived for spheroidal particles are incorporated to describe the steady hydrodynamic interactions of the particles [121, 138, 154]. Unsteady particle–fluid hydrodynamic forces are approximated by models derived for volume-equivalent spheres [94], as models for non-spherical particles do not yet exist. The magnetically induced torque is com-

puted through the surface integration of the hydrostatic pressure over the surface of the particles [117]. Furthermore, we present a new momentum coupling strategy for taking into account both the linear and angular momentum transfer between the fluid and the dispersed non-spherical particles. First, the proposed model is experimentally validated in single- and two-particle systems. Next, many-particle MDS systems are simulated where mono-dispersed mixtures of spheroidal particles are separated. We investigate the effects of particle shape and collisions on the separation efficiency of the MDS system by considering different aspect ratios and switching the collisions off, respectively.

The rest of the chapter is organized as follows. In section 4.2, we introduce the mathematical model for the kinematics and dynamics of the motion of ellipsoidal particles in a magnetized liquid. The governing equations of fluid and particles, and the momentum coupling strategy are presented. Numerical discretization methods and the experimental setup are discussed in sections 4.3 and 4.4, respectively. In section 4.5, we first experimentally validate the numerical model in single and two-particle systems and investigate the effect of particle shape on single-particle levitation dynamics. Next results of simulations of many-particle MDS systems are presented and discussed. Concluding remarks are made, and future research directions are addressed in section 4.6.

4.2. Mathematical description

In this section, we present the mathematical model for the motion of dispersed particles and the magnetic fluid. First, the motion of spheroidal particles in a magnetised fluid is described. Next, the governing equations of the fluid motion are presented. The third subsection addresses the fluid-particle momentum coupling strategy.

4.2.1. Particles

4.2.1.1. Kinematics

To describe the translational and rotational motion of spheroidal particles, three coordinate systems are introduced. A global inertial frame, a co-rotating frame attached to the particle, and a co-moving, non-rotating frame attached to the center of the particle. A vector indicated by $\boldsymbol{x}$ in the inertial global frame (xyz) is indicated by $\boldsymbol{x}'$ in the particle-fixed frame, $(x'y'z')$, and in the non-rotating frame attached to the particle center of mass $(x''y''z'')$, this vector is denoted as $\boldsymbol{x}''$. The three considered frames are illustrated in figure 4.1 **(a)**. The orientation of an axisymmetric particle with symmetry axis denoted by the unit vector $\boldsymbol{e}_{y'}$ can be described by the Euler angle representation, which consists of three angles each about a particular coordinate axis [141] (see figure 4.1 **(b)**). We can specify the Euler angles and the axes of sequential rotations using the convention $(\psi)_3, (\theta)_1, (\phi)_3$, which denotes a rotation of $(x''y''z'')$ through angle ψ about the z'' axis, resulting in the intermediate orientation, $(\hat{x}\hat{y}\hat{z})$, followed by a rotation through angle θ about the $\hat{x}$ axis, resulting in $(\hat{\hat{x}}\hat{\hat{y}}\hat{\hat{z}})$, and a final
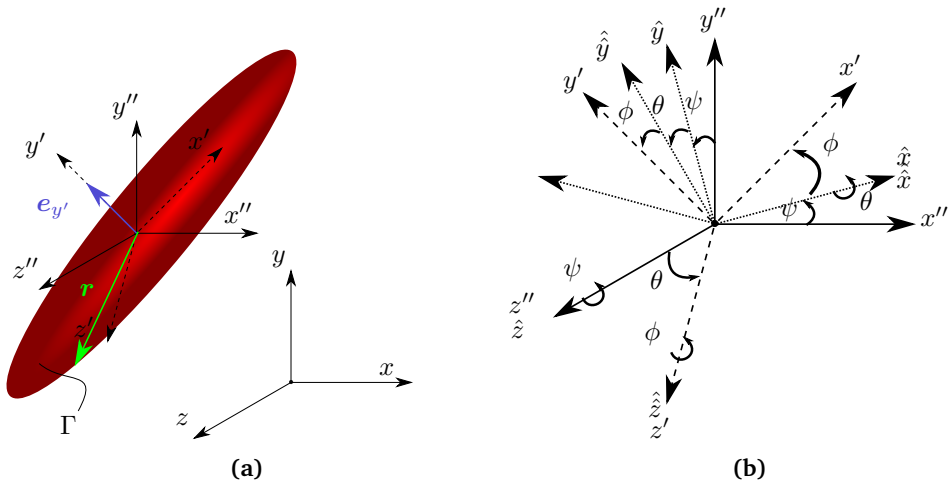
Figure 4.1.: (a) The three coordinates systems defined to describe the motion of an ellipsoidal particle. $\boldsymbol{e}_{y'}$ is the particle orientation vector and Γ denotes the surface of the particle. $\boldsymbol{r}$ is a vector that connects the centre of the particle to a point on the particle surface. **(b)** The Euler angle representation of the particle frame using the convention $(\psi)_3, (\theta)_1, (\phi)_3$.

rotation through angle ϕ about the $\hat{\hat{z}}$ axis, to produce the new orientation $(x'y'z')$. One should note that the rotations in the Euler angle representation are not commutative. The Euler angle representation of particle orientation using the convention $(\psi)_3, (\theta)_1, (\phi)_3$ is shown in figure 4.1 **(b)**.

To avoid the so-called *gibmal lock* effect stemming form the singular representation of Euler angles [82, 141], instead of Euler angle representation, we describe the particle orientation by the unit quaternion $\boldsymbol{q}_i = (q_1, q_2, q_3, q_4)^T \in \mathbb{S}^3$, where $\mathbb{S}^3$ is the space of unit quarternioins. The quaternion components are related to the angle of rotation Φ and its axis $\boldsymbol{e}$ through $(q_1, q_2, q_3)^T = \boldsymbol{e} \sin(\Phi/2)$ and $q_4 = \cos(\Phi/2)$. The transformation form the global frame to the particle frame $(x'y'z')$ is achieved through the orthogonal rotation matrix, C:

$$\boldsymbol{x}' = C(\boldsymbol{q}) \cdot \boldsymbol{x}''. \tag{4.1}$$

The rotation matrix can be expressed in terms of quaternions as

$$\mathrm{C}(\boldsymbol{q}) = \begin{pmatrix} q_1^2 - q_2^2 - q_3^2 + q_4^2 & 2(q_1q_2 + q_3q_4) & 2(q_1q_3 - q_2q_4) \\ 2(q_1q_2 - q_3q_4) & -q_1^2 + q_2^2 - q_3^2 + q_4^2 & 2(q_2q_3 + q_1q_4) \\ 2(q_1q_3 + q_2q_4) & 2(q_2q_3 - q_1q_4) & -q_1^2 - q_2^2 + q_3^2 + q_4^2 \end{pmatrix}. \tag{4.2}$$

The time-derivative of the particle quaternion is related to the angular velocity in the particle frame $\boldsymbol{\Omega}'$ through

$$\begin{pmatrix} \mathrm{d}q_1/\mathrm{d}t \\ \mathrm{d}q_2/\mathrm{d}t \\ \mathrm{d}q_3/\mathrm{d}t \\ \mathrm{d}q_4/\mathrm{d}t \end{pmatrix} = \frac{1}{2} \begin{pmatrix} q_4\omega_x' - q_3\omega_y' + q_2\omega_z' \\ q_3\omega_x' + q_4\omega_y' - q_1\omega_z' \\ -q_2\omega_x' + q_1\omega_y' + q_4\omega_z \\ -q_1\omega_{\dot{x}}' - q_2\omega_y' - q_3\omega_z' \end{pmatrix}, \tag{4.3}$$

where t is the time, and ω'_x, ω'_y and ω'_z are the three components of the particle angular velocity in the particle-fixed frame. Using the (zyx) convention, the Euler angles read $((\psi)_3, (\theta)_1, (\phi)_3) = \left(\tan^{-1} \frac{c_{23}}{c_{33}}, -\sin^{-1} c_{13}, \tan^{-1} \frac{c_{12}}{c_{11}} \right)$, where c_{ij} are the elements of particle rotation matrix C.

The translational displacement of the particle follows

$$\frac{\mathrm{d}\boldsymbol{x}_i}{\mathrm{d}t} = \boldsymbol{v}_i, \tag{4.4}$$

where $\boldsymbol{v}_i$ and $\boldsymbol{x}_i$ denote the translational velocity and position of the particle centre of mass respectively.

4.2.1.2. Dynamics

For an ellipsoidal particle moving in a uniform flow, the translational motion in the global inertial frame is described by

$$\frac{d\boldsymbol{v}_i}{dt} = \frac{1}{m_i} \left(\sum \boldsymbol{F}_i + \boldsymbol{F}_i^{(c)} \right), \tag{4.5}$$

where $\sum \boldsymbol{F}_i$ is the summation of forces due to hydrodynamic fluid-particle interactions, and $\boldsymbol{F}_i^{(c)}$ is the force acting on a particle because of collisions with other particles or walls. Similar to the equation of motion of spherical particles discussed in chapter 2, we include the force due to the undisturbed flow field $\boldsymbol{F}_{\mathrm{U},i}$, the steady drag $\boldsymbol{F}_{\mathrm{D},i}$, the buoyancy $\boldsymbol{F}_{\mathrm{B},i}$, the gravity $\boldsymbol{F}_{\mathrm{G},i}$, the added mass $\boldsymbol{F}_{\mathrm{AM},i}$ and the Basset history force $\boldsymbol{F}_{\mathrm{H},i}$ as the relevant hydrodynamic forces in the equation of motion of spheroidal particles. Additionally, since depending on the orientation of the particle relative to the direction of fluid-particle relative velocity, a non-zero lift force can act on a non-spherical particle, the pitching lift force $\boldsymbol{F}_{\mathrm{PL},i}$ is also included in the model. Considering the above mentioned fluid-particle interaction mechanisms, the summation $\sum \boldsymbol{F}_i$ reads

$$
\begin{aligned}
\sum \boldsymbol{F}_i = {}& \underbrace{\rho_{\mathrm{f}} V_i \frac{D\boldsymbol{u}_i}{Dt}}_{\boldsymbol{F}_{\mathrm{U},i}} + \underbrace{\frac{1}{8} C_D \rho_{\mathrm{p},i} d_{\mathrm{p}}^2 ||\boldsymbol{u}_i - \boldsymbol{v}_i|| \, (\boldsymbol{u}_i - \boldsymbol{v}_i)}_{\boldsymbol{F}_{\mathrm{D},i}} \\
& + \underbrace{\frac{3}{2} \Delta_{\mathrm{H}} \left(\pi \rho_{\mathrm{f}} \mu \right)^{1/2} d_{\mathrm{p,e}}^2 \left[\int_{-\infty}^t \frac{\frac{d}{d\tau} (\boldsymbol{u}_i - \boldsymbol{v}_i)}{(t - \tau)^{1/2}} d\tau \right]}_{\boldsymbol{F}_{\mathrm{H},i}} \\
& + \underbrace{\frac{1}{2} \Delta_{\mathrm{A}} \rho_{\mathrm{f}} V_i \left(\frac{D\boldsymbol{u}_i}{Dt} - \frac{d\boldsymbol{v}_i}{dt} \right)}_{\boldsymbol{F}_{\mathrm{AM},i}} - \underbrace{\rho_{\mathrm{p},i} V_i g \boldsymbol{e}_y}_{\boldsymbol{F}_{\mathrm{G},i}} + \underbrace{\rho_{\mathrm{f,a}} V_i g \boldsymbol{e}_y}_{\boldsymbol{F}_{\mathrm{B},i}} \\
& + \underbrace{\frac{1}{8} C_L \rho_{\mathrm{p},i} d_p^2 ||\boldsymbol{u}_i - \boldsymbol{v}_i||^2 \boldsymbol{e}_{\mathrm{PL}}}_{\boldsymbol{F}_{\mathrm{PL},i}},
\end{aligned} \tag{4.6}
$$

where $\boldsymbol{u}_i$ is the undisturbed fluid velocity at the position of the particle, ρ_{p} and V_i are the particle mass density and volume, and μ is the fluid dynamics viscosity. Coefficients Δ_{H} and Δ_{A} are the history and added mass coefficients. To the best knowledge of the authors, orientation-dependent correlations for these coefficients for non-spherical particles do not exist yet. In the present work, we take the diameter of the volume-equivalent sphere as the length scale for evaluating the added mass force and the Basset history force. In this case, $\Delta_{\mathrm{A}} = \Delta_{\mathrm{H}} = 1$. For coefficients of steady drag and pitching lift, depending on the particle shape, we follow shape-specific correlations of Sanjeevi and Padding [121] for a 2:5 oblate spheroid and the neural network correlation of Tajfirooz et al. [138] for 1:10 spheroids in chapter 3. In the last term in (4.6), $\boldsymbol{e}_{\mathrm{PL}}$ is the lift force orientation unit vector given by [95]

$$\boldsymbol{e}_{\mathrm{PL}} = \frac{\boldsymbol{e}_{y'} \cdot (\boldsymbol{u}_i - \boldsymbol{v}_i)}{\|\boldsymbol{e}_{y'} \cdot (\boldsymbol{u}_i - \boldsymbol{v}_i)\|} \frac{(\boldsymbol{e}_{y'} \times (\boldsymbol{u}_i - \boldsymbol{v}_i)) \times (\boldsymbol{u}_i - \boldsymbol{v}_i)}{\|(\boldsymbol{e}_{y'} \times (\boldsymbol{u}_i - \boldsymbol{v}_i)) \times (\boldsymbol{u}_i - \boldsymbol{v}_i)\|}, \tag{4.7}$$

where $\boldsymbol{e}_{y'}$ is the particle orientation vector parallel to the particle symmetry axis as shown in figure 4.1. When the relative particle-fluid velocity undergoes a step change (e.g. during collisions) a special treatment of the Basset history term is required. For details of this treatment, the reader is referred to chapter 2 [76, 139].

The angular motion of the particle is described in the particle frame. In this frame, the angular velocity of the particle follows

$$\boldsymbol{I}'_{\mathrm{i}} \cdot \frac{\mathrm{d}\boldsymbol{\Omega}'_{\mathrm{i}}}{\mathrm{d}t} + \boldsymbol{\Omega}'_{\mathrm{i}} \times \boldsymbol{I}'_{\mathrm{i}} \cdot \boldsymbol{\Omega}'_{\mathrm{i}} = \sum \boldsymbol{T}'_{\mathrm{i}} + \boldsymbol{T}'^{(c)}_{i}, \tag{4.8}$$

where $\boldsymbol{I}'_i = \mathrm{diag}(I_1, I_2, I_3)$ is the particle tensor of inertia about the particle principal axis (x', y', z'). $\sum \boldsymbol{T}'_i$ denotes the summation of torques due to the fluid-particle interactions and $\boldsymbol{T}'^{(c)}_{i}$ is the torque due to the collisions with other particles or walls. For the angular fluid-particle interactions in a uniform flow of a magnetised fluid, we consider three torque contributions. These contributions are the pitching torque $\boldsymbol{T}_{\mathrm{P}}$, the rotational resistant torque $\boldsymbol{T}_{\mathrm{R}}$, and the torque due to the magnetic buoyancy $\boldsymbol{T}_{\mathrm{MB}}$. The last contribution stems from the non-linear pressure distribution on the surface of a particle immersed in a magnetised fluid [117]. The sum of these contributions in the global frame reads

$$\sum \boldsymbol{T}_{\mathrm{i}} = \underbrace{\frac{1}{2} C_{T,\mathrm{p}} \rho_f \frac{\pi}{8} d_{\mathrm{p}}^3 \|\boldsymbol{u}_i - \boldsymbol{v}_i\|^2 \boldsymbol{e}_{\mathrm{PT}}}_{\boldsymbol{T}_{\mathrm{P},i}}$$
$$+ \underbrace{\int_{\Gamma} \boldsymbol{r} \times (p_{\mathrm{static,M}} \mathbb{I} \cdot \boldsymbol{N}) \mathrm{d}S}_{\boldsymbol{T}_{\mathrm{MB},i}} + \underbrace{\frac{1}{64} \rho \mathrm{C}_R \left(\frac{1}{2}\boldsymbol{\omega}_i - \boldsymbol{\Omega}_i\right) \left\|\frac{1}{2}\boldsymbol{\omega}_i - \boldsymbol{\Omega}_i\right\| d_p^5}_{\boldsymbol{T}_{\mathrm{R},i}} \tag{4.9}$$

where $\boldsymbol{r}$ denotes the outward pointing surface vector in the particle frame (see figure 4.1), and $p_{\mathrm{static,M}}$ is the magnetic contribution to the hydrostatic pressure given by

$$p_{\mathrm{static,M}} = \mu_0 \int_0^H M dH. \tag{4.10}$$

Note that the gravitational contribution to the static pressure does not induce any torque on the particle. e_{PT} is the orientation unit vector of the pitching torque given by [95]

$$e_{\text{PT}} = \frac{e_{y'} \cdot (u_i - v_i)}{|e_{y'} \cdot (u_i - v_i)|} \frac{(e_{y'} \times (u_i - v_i)) \times (u_i - v_i)}{\|(e_{y'} \times (u_i - v_i)) \times (u_i - v_i)\|}. \tag{4.11}$$

The pitching torque coefficient is described by the shape-specific correlations of Zastawny et al. [154] and Sanjeevi and Padding [121] and the neural network correlation of Tajfirooz et al. [138] derived in chapter 3. Moreover, we neglect the rotation of particles around the particle symmetry axis, y'.

In the motion of ellipsoidal particles in viscous liquids, the rotational resistance torque can have a significant contribution to the particle motion. To the best knowledge of the authors, except for the expression of Jeffery [70] for ellipsoids in the Stokes regime, and shape-specific correlations of Zastawny et al. [154], correlations for rotational torque coefficient of ellipsoidal particles beyond the Stokes regime have not yet been derived. Hence, for 1:2 oblate spheroids considered in this chapter, we use the correlation of Zastawny et al. [154] for a 5:2 prolate spheroid to describe the rotational resistance torque. For 1:10 spheroids the correlation of Zastawny et al. [154] for 1:5 oblate spheroids is used . All the incorporated models for the force and torque coefficients are summarised in Appendix 4.A.

4.2.1.3. Collisions

For the inter-particle and particle-wall collisions we follow the constraint-based method of Mirtich and Canny [98], Guendelman et al. [58] and Bender and Schmitt [18]. Tschisgale et al. [142] used the same strategy to model collisions of Cosserat-type rods. Similar to the collision model presented for spherical particles in chapter 2, the method proposed in this section consists of two main steps: First, possible contacts between particle pairs are detected and sorted based on their collision time. Next, the collision response is calculated for the colliding pairs in a consecutive manner. Inter-particle and particle-wall contacts are detected by computing the minimum distance between particle pairs. To compute the minimum distance, we follow the iterative approach of Jain et al. [68], which exploits the principle that the shortest line connecting the surfaces of two ellipsoids lies along the common normal line of the two ellipsoids. A collision is detected when the minimum distance between two particles is less than a threshold ϵ, i.e. $\|d\| < \epsilon$, with d denoting the minimum distance vector connecting particle a to particle b as shown in figure 4.2 **(a)**. We consider a threshold of $\epsilon = 0.01 d_{\text{major}}$ where d_{major} is the equatorial diameter of a spheroid.

To minimise the number of particles that have to be searched for a collision, the neighbour list strategy of Hoomans et al. [64] is employed in which the computational domain is split into several "collision blocks". When searching for a collision partner of a particle, only the particles in the same and neighbouring collision blocks are scanned. Multiple contact instances are treated as sequences of single binary collisions between pairs of two particles. Within a collision block, for each particle, the possible collision pairs are sorted based on their time of impact (TOI). The collisions with the shortest
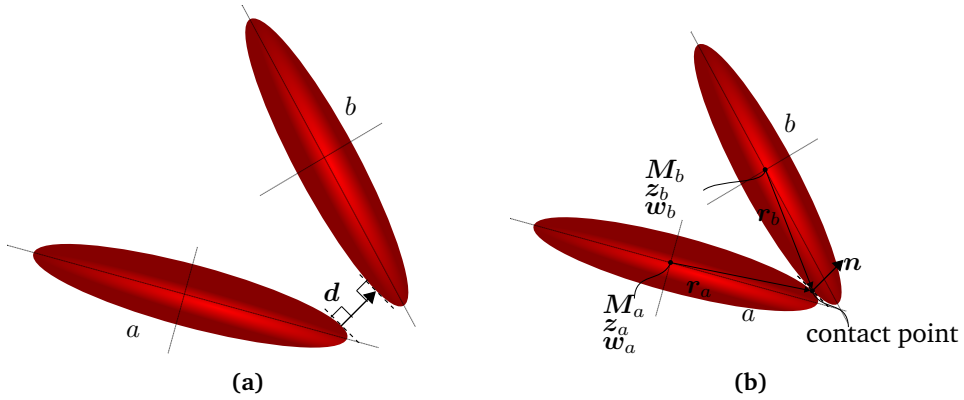
Figure 4.2.: (a) The minimum distance vector $\boldsymbol{d}$ between two approaching particles. **(b)** A binary collision between two particles a and b. The orientation of the collision impulse is defined by the normal vector $\boldsymbol{n}$ pointing from particle a to particle b. The vector $\boldsymbol{r}$ points from the particle centre to the contact point. The motion of each particle is defined by the particle inertia matrix $\boldsymbol{M}$, the particle twist $\boldsymbol{z}$, and the particle wrench $\boldsymbol{w}$.

TOI are treated first. Calculating TOI for spherical particles is straightforward: If a collision occurs, the distance between the two centres of the particles is equal to the sum of the two radii, and the time of impact can be found analytically by solving a quadratic equation [4, 64]. For ellipsoidal particles, however, TOI depends on the orientation of the particles as well as their angular velocity. For systems involving many particles, calculating TOI is very time-consuming. In this work, TOI is approximated by using a bisection method in combination with the minimum distance algorithm of Jain et al. [68]. Similar to the algorithm used for the detection of collisions between spheres, within a time step dt, the linear and angular velocities of the particles are assumed to change only due to collisions. For each relevant particle pair, a pseudo time step $dt_{s_i}^{n} = \min(dt, \mathrm{TOI}^n)$ is taken, and the minimum distance between the two particles within this pseudo time step is calculated. Here TOI^n is the time of impact of a particle at the beginning of the nth actual solver time step dt, and i denotes a bisection step. If a contact is detected, the pseudo time step is halved and over the half time interval where the impact occurs, the procedure is repeated with $dt_s^{i+1} = dt_s^{i}/2$ until a certain accuracy for the collision time is achieved, i.e. $|\mathrm{TOI}^{i+1} - \mathrm{TOI}^i| < \epsilon_t$ with ϵ_t the threshold for the bisection method. We consider a value of $0.001 dt$ for this threshold.

The collision response model is based on three assumptions [142]:

1. Infinitesimal collision time: The time scale of the collisions between the particles is assumed to be much smaller than the time scale of the motion of the particles. Based on this assumption, the position and orientation of the particles remain constant, and the collision forces are impulsive in nature (sustained contacts are treated by sequences of collisions).

2. Poisson's hypothesis: The behaviour of particles during a collision is described by a compression phase and a restitution phase. The normal relative velocity

at the contact point before and after a binary collision are related through the restitution coefficient, e.

3. Coulomb friction model: The motion of particles in the tangential direction during the collision is described by static and dynamic coefficients of friction. The friction force in the tangential direction is proportional to the normal contact force.

To describe the dynamics of a binary collision between particle a and b, as shown in figure 4.2, for each particle a twist is defined as $\boldsymbol{z} = [\boldsymbol{v}, \boldsymbol{\Omega}]^\top$, where $\boldsymbol{v}$ and $\boldsymbol{\Omega}$ are the particle linear and angular velocities respectively. The post- and pre-collision linear and angular particle velocities are related through

$$
\begin{aligned}
\boldsymbol{z}_a^+ &= \boldsymbol{z}_a^- - \boldsymbol{M}_a^{-1}\mathcal{C}_a^\top \boldsymbol{J}, \\
\boldsymbol{z}_b^+ &= \boldsymbol{z}_b^- + \boldsymbol{M}_b^{-1}\mathcal{C}_b^\top \boldsymbol{J},
\end{aligned}
\tag{4.12}
$$

where $+$ and $-$ indicate the post- and pre-collision particle quantities. $\boldsymbol{M}$ is the particle inertia matrix defined as $\boldsymbol{M} = m\mathbb{I}\oplus \boldsymbol{I}$, where $\boldsymbol{I}$ is the tensor of inertia in the inertial frame. Matrix $\mathcal{C}$ is defined as $\mathcal{C} = (\mathbb{I}, -[\boldsymbol{r}]_\times)$, where $\boldsymbol{r}$ is the vector pointing from the particle centre to the contact point, and $[\boldsymbol{r}]_\times$ is the cross-product matrix corresponding to $\boldsymbol{r}$. $\boldsymbol{J}$ denotes the impulse vector. If we let $v_{ab,n} = \mathcal{C}\boldsymbol{z}\cdot \boldsymbol{n}$ denote the normal relative velocity at the contact point, Poisson's hypothesis states

$$
v_{ab,n}^+ = -e_{\text{eff}} v_{ab,n}^-,
\tag{4.13}
$$

where $e_{\text{eff}} \in [0,1]$ is the effective coefficient of restitution for an immersed collision. The normal unit vector at the contact point $\boldsymbol{n}$ is the unit vector normal to both particles at the contact point and pointing to particle b (see figure 4.2 **(b)**). A collision is distinguished as being either "sticking" or "sliding". According to Coulomb's friction model, a collision is sticking if $J_t \leq \mu_{\text{fric}} J_n$ and it is sliding otherwise, where $J_t = \boldsymbol{J}\cdot \boldsymbol{t}$ and $J_n = \boldsymbol{J}\cdot \boldsymbol{n}$ are the tangential and normal components of the impulse vector and μ_{fric} is the friction coefficient. The tangential vector at the contact point is $\boldsymbol{t} = -\boldsymbol{v}_{ab,t}/|\boldsymbol{v}_{ab,t}|$ with the tangential relative velocity at the contact point given by $\boldsymbol{v}_{ab,t} = \boldsymbol{v}_{ab} - \boldsymbol{v}_{ab,n}$. We assume that the effect of external loads during a collision is negligible. The algorithm initially assumes a sticking collision and calculates the collision impulse according to

$$
\boldsymbol{J} = -\boldsymbol{K}^{-1}\Delta \boldsymbol{v}_{ab}
\tag{4.14}
$$

where $\boldsymbol{K} = \mathcal{C}_b \boldsymbol{M}_b^{-1}\mathcal{C}_b^T + \mathcal{C}_a \boldsymbol{M}_a^{-1}\mathcal{C}_a^T$ and $\Delta \boldsymbol{v}_{ab} = \boldsymbol{v}_{ab}^- - \boldsymbol{v}_{ab}^+ = \boldsymbol{v}_{ab}^- + e_{\text{eff}}(\boldsymbol{v}_{ab}^- \cdot \boldsymbol{n})\boldsymbol{n}$. Next, the criterion for a sliding collision is checked and the impulse vector is overwritten if the collision turns out to be sliding, i.e.:

$$
\boldsymbol{J} = \begin{cases} \boldsymbol{J} & \text{if } \|\boldsymbol{J} - \boldsymbol{J}\cdot \boldsymbol{n}\| \leq \mu_{\text{fric}}\boldsymbol{J}\cdot \boldsymbol{n} \text{ (sticking)}, \\ \frac{\boldsymbol{K}\boldsymbol{J}\cdot \boldsymbol{n}}{\boldsymbol{K}(\boldsymbol{n}+\mu_{\text{k}}\boldsymbol{t})\cdot \boldsymbol{n}} (\boldsymbol{n}+\mu_{\text{fric}}\boldsymbol{t}) & \text{otherwise} \quad \text{(sliding)}, \end{cases}
\tag{4.15}
$$

In this work, we do not distinguish between the static and dynamic coefficients of friction. For a spherical particle, this collision model reduces to the hard-sphere model presented in chapter 2.

4.2.2. Continuous phase

The motion of the fluid phase is described in the same way as presented in chapter 2. The governing equations of the incompressible flow of a Newtonian magnetically responsive fluid are described in the global frame as [118]

$$\rho_{\text{f}} \left(\frac{\partial \boldsymbol{u}}{\partial t} + (\boldsymbol{u} \cdot \boldsymbol{\nabla}) \boldsymbol{u} \right) = -\boldsymbol{\nabla} p^* + \mu \nabla^2 \boldsymbol{u} + \mathfrak{F}^{\text{inter}}, \tag{4.16}$$

$$\boldsymbol{\nabla} \cdot \boldsymbol{u} = 0, \tag{4.17}$$

where $\boldsymbol{u}$ is the fluid velocity, μ and ρ_{f} are the fluid dynamic viscosity and mass density respectively. p^* is the reduced pressure. If we assume that the gravity acts in the direction of $-\boldsymbol{e}_y$:

$$p^* = p - p_{\text{static}} = p + \rho_{\text{f}} g y - \mu_0 \int_0^H M dH, \tag{4.18}$$

where $M = |\boldsymbol{M}|$ is the magnitude of the fluid magnetization, $H = |\boldsymbol{H}|$ is the magnetic field strength, and μ_0 denotes the vacuum permeability. The term $\mathfrak{F}^{\text{inter}}$ in (4.16) is the fluid-particle momentum coupling term. Equations (4.16) and (4.17) are solved in a cubic domain with dimensions $L_x \times L_y \times L_z$, where x, y, and z denote the stream-wise, wall-normal, and span-wise directions respectively.

In this study, we consider an aqueous paramagnetic fluid ($MnCl_2$ salt solution) with a linear magnetization behavior [9, 118]:

$$\boldsymbol{M} = \chi \boldsymbol{H}. \tag{4.19}$$

where χ is the magnetic susceptibility of the liquid.

4.2.3. Momentum coupling

In this section, we present a momentum coupling strategy that takes into account both linear and angular momentum transfer between the continuous fluid and nonspherical particles. For linear momentum coupling we employ an approach similar to the one presented in chapter 2. The local particle feedback force is defined as

$$\mathfrak{F}^{\text{inter}} (\boldsymbol{x}) \equiv -\sum_{n=1}^{N_{\text{p}}} \mathcal{P} \left(\boldsymbol{x} - \boldsymbol{x}_{\text{p}}^{(n)} \right) \boldsymbol{F}_{2\text{w}}^{(n)} \tag{4.20}$$

where N_{p} denotes the total number of particles and $\boldsymbol{F}_{2\text{w}}^{(n)}$ is the particle feedback force defined as $\boldsymbol{F}_{2\text{w}}^{(n)} = \boldsymbol{F}_{\text{U}} + \boldsymbol{F}_{\text{D}} + \boldsymbol{F}_{\text{H}} + \boldsymbol{F}_{\text{AM}}$, and $\mathcal{P} \left(\boldsymbol{x} - \boldsymbol{x}_{\text{p}}^{(n)} \right)$ is a top-hat filter that uniformly distributes the feedback force to the Eulerian grid points according to

$$\mathcal{P}(\boldsymbol{x} - \boldsymbol{x}_{\text{p}}) = \begin{cases} \dfrac{1}{\sigma_1 \sigma_2 \sigma_3}, & \text{if } |x_k - x_{\text{p},k}| < \sigma_k/2 \ (k = 1, 2, 3), \\ 0, & \text{otherwise.} \end{cases} \tag{4.21}$$
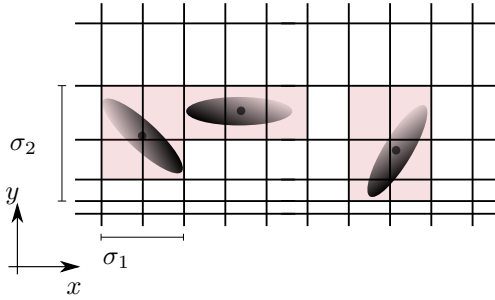
Figure 4.3.: The volume considered for the linear momentum transfer between the fluid and the particle is an encompassing rectangular block around each particle. The size and shape of this block is dynamically adjusted during the motion of the particle.

σ_k, $k = 1, 2, 3$ is the width of the coupling volume in each direction. The coupling algorithm is extended to take into account the effects of particle shape and orientation on the volume over which the two-way coupling force is distributed. This coupling volume is a rectangular block with a volume closest to the volume of the smallest encompassing box around the particle. The shape of this block changes dynamically according to the particle orientation and position. A 2D schematic of the filter used for the linear momentum transfer is shown in figure 4.3.

Furthermore, as the particle nonsphericity increases, the rotational momentum transfer between the particles and the continuous phase becomes more important [150]. Andersson et al. [8] introduced a procedure for implementing the two-way angular momentum coupling in point-particle simulations of small non-spherical particles. Their proposed strategy is based on the concept of "particle stress tensor" which was earlier introduced for micro-polar fluids [Eringen 1966]; The angular momentum coupling is achieved by locally imposing the contribution of the anti-symmetric particle stress tensor to the fluid equation of motion. The application of this strategy is feasible for particles that are much smaller than the Eulerian grid spacing. When the particle size is in the same order as the grid spacing, which is the case in this study, this point-torque approach loses its justification. Therefore, in this work, the two-way angular momentum transfer is achieved by introducing point-forces to the fluid momentum equation: First, the particle feedback torque is modelled as

$$\boldsymbol{T}_{\mathrm{2w}} = \boldsymbol{T}_{\mathrm{P},i} + \boldsymbol{T}_{\mathrm{R},i}, \tag{4.22}$$

where $\boldsymbol{T}_{\mathrm{P},i}$ and $\boldsymbol{T}_{\mathrm{R},i}$ are the pitching and rotational resistance torques respectively. Next, the coupling torque $\boldsymbol{T}_{\mathrm{2w}}$ is transformed to a set of point forces that act on the Eulerian grid points which surround the particle centre (see figure 4.4 **(a)**). These point-forces should satisfy three conditions:

1. The sum of the forces should not contribute to the linear momentum of the fluid.

2. The moment of the forces should be equal to the particle feedback torque $\boldsymbol{T}_{\mathrm{2w}}$.

3. To be consistent with the linear momentum coupling approach, the moment should preferably be uniformly distributed over the torque coupling volume.
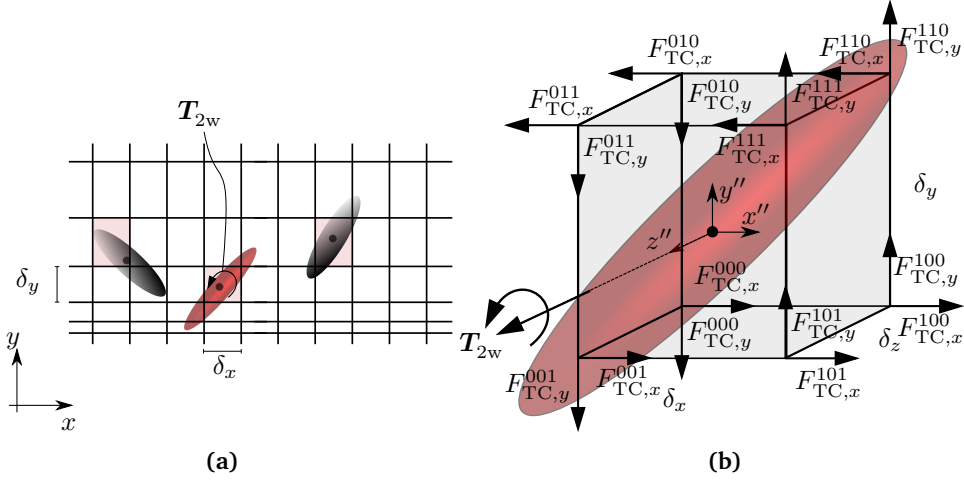
Figure 4.4.: A schematic illustration of the particle-to-fluid torque coupling strategy. **(a)** A torque T_{2w} acting on the fluid from the particle in positive z- direction is uniformly distributed over the Eulerian grid cell in which the particle center is located. **(b)** The angular momentum coupling strategy: A feedback torque T_{2w} acting in positive z- direction is transformed to point-forces acting on the eight grid points surrounding the particle centre. Note that only point-forces in x- and y- directions can contribute to a torque in z- direction.

For each particle, we impose eight point-forces, each on one surrounding grid point of the particle centre. If we let F^{ijk} denote the point force on grid point ijk as shown in Figure 4.4 **(b)**. It can be shown that the mapping

$$
\boldsymbol{F}_{\mathrm{TC}}^{ijk} = \mathcal{L}(\boldsymbol{T}_{2w}) = \frac{1}{8V_{\mathrm{TC}}}
\begin{pmatrix}
(-1)^{j+1}T_{2w,z}/\delta_y + (-1)^k T_{2w,y}/\delta_z \\
(-1)^{k+1}T_{2w,x}/\delta_z + (-1)^i T_{2w,z}/\delta_x \\
(-1)^{i+1}T_{2w,y}/\delta_x + (-1)^j T_{2w,x}/\delta_y
\end{pmatrix}
\cdot
\begin{pmatrix}
\boldsymbol{i} \\
\boldsymbol{j} \\
\boldsymbol{k}
\end{pmatrix},
\quad i,j,k \in \{0,1\}
$$

(4.23)

results in a force set that satisfies the above three conditions. Here, V_{TC} is the volume of the grid cell in which the particle centre is located, and δ_x, δ_y and δ_z are the cell sizes in x-, y-, and z- directions, respectively. For the sake of clarity, this torque-to-force transformation is schematically illustrated in figure 4.4 **(b)** for a case where T_{2w} is in the positive z- direction. One should note that in this work, one grid cell is considered as the volume over which angular momentum transfer is distributed for each particle. This approach can be extended to coupling volumes larger than one grid cell, in a similar way as for the transfer of linear momentum.

4.3. Numerical discretization

To obtain the particle trajectories, equations (4.3) to (4.5), and (4.8) are solved using a forward Euler scheme. The incorporated Euler scheme uses each stage of the Runge-Kutta discretisation scheme for the fluid as a time step. To avoid the amplification of discretisation errors in predicting the particle orientation according to (4.3), the particle quaternion is normalised according to

$$\hat{q} = \frac{q}{\sqrt{q_0^2 + q_1^2 + q_2^2 + q_3^2}}, \qquad (4.24)$$

where $\hat{q}$ is the normalised quaternion at the end of each time step taken by the particle solver.

The numerical cost of the evaluation of the Basset history contribution to (4.5) is reduced by using the windowing method of Van Hinsberg et al. [144], where the history kernel is split into a window kernel and a tail kernel. The window kernel (recent history) is approximated by an ordinary trapezoidal rule over the interval $[t - t_{\text{win}}, t]$ that consists of N_{w} previous time steps. The tail kernel (old history) over the time interval $(-\infty, t - t_{\text{win}})$ is approximated by a sum of exponential functions. The integral corresponding to the magnetic torque in (4.9) is computed numerically using a first-order integration scheme.

The governing equations of the continuous phase, (4.16) and (4.17) are first reduced to a fourth-order equation for the wall-normal velocity component and a second-order equation for the wall-normal component of vorticity. Next, the equations are spatially discretised by a pseudo-spectral method. For details of the numerical discretisation method, the reader is referred to Kim et al. [77], Kuerten et al. [81].

4.4. Experimental setup

To validate the numerical framework presented in section 4.2, the experimental setup introduced in chapter 2 (see figure 4.5) is used to perform single-particle levitation experiments using non-spherical particles. The particle tracking velocimetry method is extended to capture both position and orientation of non-spherical particles. We consider three particle shapes for the levitation experiments: 1:2 oblate spheroids, a 1:5 disk, and a 1:10 disk, as shown in Figure 4.6. The particles are made of either unplasticized polytetrafluoroethylene (PVC-U) or polyoxymethylene (POM) with mass densities $\rho_{\text{p}} = 1434 \text{ kg/m}^3$, and $\rho_{\text{p}} = 1407 \text{ kg/m}^3$, respectively. The mass density of the paramagnetic liquid is $\rho_{\text{p}} = 1403 \text{ kg/m}^3$ The relevant properties of the particles used in the experiments are summarized in Table 4.1.
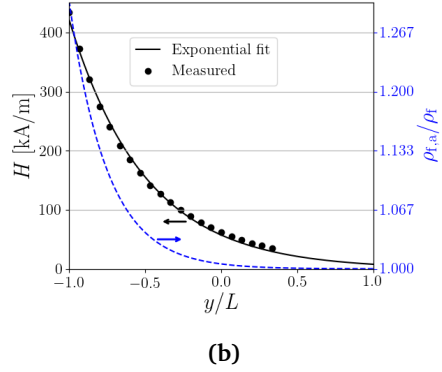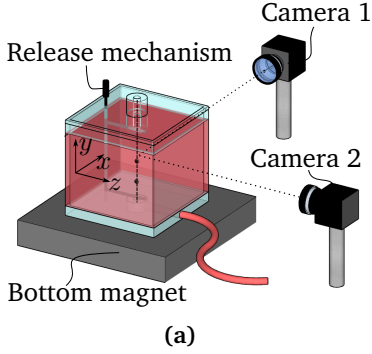
Figure 4.5.: (a) A sketch of the experimental setup used for single- and two-particle levitation experiments. (b) Magnetic field strength on the vertical line at the centre of the tank (black circles): $H = H_0 e^{-\pi(L+y)/p}$ where $H_0 = 422$ kA/m and $p = 0.118$ m. The blue dashed line indicates the apparent mass density of the magnetic fluid with $\chi = 7 \times 10^{-4}$ is indicated by the blue dashed line. (The horizontal arrows indicate the corresponding axes).

Figure 4.6.: Particles used for single-particle levitation experiments. From left to right a 1:2 oblate spheroid (p_1), a 1:5 disk (p_2), and a 1:10 disk (p_3). All three particles are made of PVC-U.

	d_{major} [mm]	d_{minor} [mm]	w	V [mm^3]	ρ_{p} [kg/m^3]
Oblate Spheroid (p_1)	5	2.5	0.5	32.73	1434
Disc 1 (p_2)	5	1	0.2	19.63	1434
Disc 2 (p_3)	5	0.5	0.1	9.82	1434
Oblate Spheroid (p_4)	5	2.5	0.5	32.73	1407

Table 4.1.: Physical properties of the particles considered in the experiments.

4.5. Results and discussions

4.5.1. Single particle dynamics

4.5.1.1. Experimental validation of the model

In this section, we investigate the levitation dynamics of single non-spherical particles. It is well known that in the settling motion of an oblate spheroidal particle immersed in a quiescent nonmagnetic fluid, the stable particle orientation is at $\phi = \arccos\left((\boldsymbol{v} - \boldsymbol{u}) \cdot \boldsymbol{e}_{y'}\right) = 90°$ [30]. This stable orientation can be influenced by the magnetic buoyancy torque once a particle is immersed in a magnetized liquid. However, in the magneto-fluidic configurations considered in this work $\frac{\partial H}{\partial x} = \frac{\partial H}{\partial z} = 0$, i.e. the magnetic buoyancy and gravity forces are collinear. Hence, the stable broadside orientation is not influenced by the presence of the magnetic field. In single-particle systems where particle-particle interactions are absent, the dominant particle orientation is, therefore, $\phi = 90°$. At this orientation, at sufficiently low Reynolds numbers a particle does not undergo a pitching lift. Similar to the analysis for single spherical particles, also in this section we neglect the influence of the particle on the fluid (one-way coupling assumption) in the numerical simulation method. Under these assumptions, the governing equation of the motion reduces to the scalar system

$$
\begin{aligned}
\frac{dy}{dt} &= v, \\
\frac{dv}{dt} &= \frac{\rho_\mathrm{p}}{\rho_\mathrm{p} + 0.5\rho_\mathrm{f}} \left[-\frac{1}{8} C_D \rho_{\mathrm{p},i} d_\mathrm{p}^2 |v| v - \frac{3}{2} \left(\pi \rho_\mathrm{f} \mu\right)^{1/2} d_e^2 \int_0^t \frac{1}{(t-\tau)^{1/2}} \frac{dv}{d\tau} d\tau \right. \\
&\quad \left. + \left(\frac{\rho_\mathrm{f,a}}{\rho_\mathrm{p}} - 1\right) g \right].
\end{aligned}
\tag{4.25}
$$

We compare the experimental trajectories of sinking and rising particles with solutions of (4.25) obtained with the same initial conditions. Sinking and rising levitation experiments are performed using particles p_1, p_2 and p_3. For the disk-shaped particle, p_2 with $w = 0.2$, the steady drag correlation of Zastawny et al. [154] is used. For the spheroid p_1 with aspect ratio $w = 0.5$, we use the correlation of Sanjeevi and Padding [121] which is derived for 2:5 oblate spheroids. The steady drag coefficient for the 1:10 disk, p_3 is based on the correlation of Tajfirooz et al. [138] derived for 1:10 spheroids in Chapter 4. All the particles are released with the broadside orientation with zero initial angular and linear velocities.

Figure 4.7 compares the experimentally obtained vertical particle positions versus time with the numerical results corresponding to solutions of system (4.25). An excellent agreement is observed between the numerical and experimental results for both the rising and falling particles. The particle levitation time of the 1:2 spheroid, $p1$ is about 70% and 30% smaller than those of the 1:5 disk, p_2 and the 1:10 disk, p_3 respectively. Note that the differences in the particle levitation times are due to the differences both in the size and in shape of the particles. To explore the effect of particle shape on the levitation dynamics, in the following section, the numerically obtained levitation dynamics of particles with identical volumes at different aspect ratios are compared.
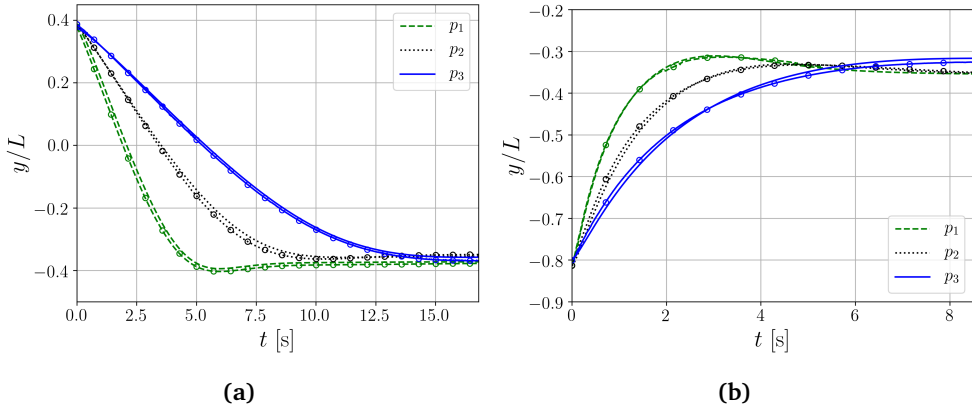
Figure 4.7.: Vertical positions of particles p_1, p_2 and p_3 as functions of time during the (a) falling and (b) rising motions. The curves without markers correspond to numerical results and those with markers indicate the experimental data. Properties of the particles are summarized in Table 4.1

4.5.1.2. Effect of non-sphericity on single-particle levitation dynamics

The effect of aspect ratio on the particle levitation motion is investigated by comparing the levitation motion of oblate spheroids of the same volume and different aspect ratios. In figure 4.8, the temporal evolutions of vertical position and velocity of four particles with $w = 1$, 0.4, 0.2 and 0.1 are plotted. The particle volume and initial position and orientation is kept identical for all particles. The volume-equivalent diameter of all particles is $d_{\mathrm{p},e} = 4$ mm. The initial condition for all the particles is $(y_0, v_0) = (L/3, 0)^T$, and the mass density is fixed at $\rho_{\mathrm{p}} = 1434$ kg/m^3. It can be observed that as the aspect ratio decreases form $w = 1$ to $w = 0.1$, the particle levitation time increases, due to the increase in steady particle drag. Compared to the levitation time of a sphere, the levitation time of an oblate spheroid with the same volume increases by approximately 53%, 90% and 146% for $w = 0.4$, $w = 0.2$ and $w = 0.1$, respectively.

The relative contributions of the different forces to the motion of the particles with $w = 1$ and $w = 0.1$ are compared in figure 4.9. Note that the forces are made non-dimensional by $((\rho_{\mathrm{p}} - \rho_{\mathrm{f}})V_{\mathrm{p}}g)$. As the particle aspect ratio decreases from 1 to 0.1, the relative contribution of the history force to the total force acting on the particle becomes smaller. However, the history force remains an important contributor to the particle motion even at $w = 0.1$.

4.5.2. Two-particle systems

To investigate the effect of a binary collision on the levitation dynamics of spheroidal particles, we consider particles with aspect ratio $w = 0.5$. Collisions are obtained by simultaneously releasing a heavy sinking particle at the top of the tank, and a light rising particle at the bottom: Particle p_1 with $\rho_{\mathrm{p},1} = 1436$ kg/m^3 is released

(a)

(b)
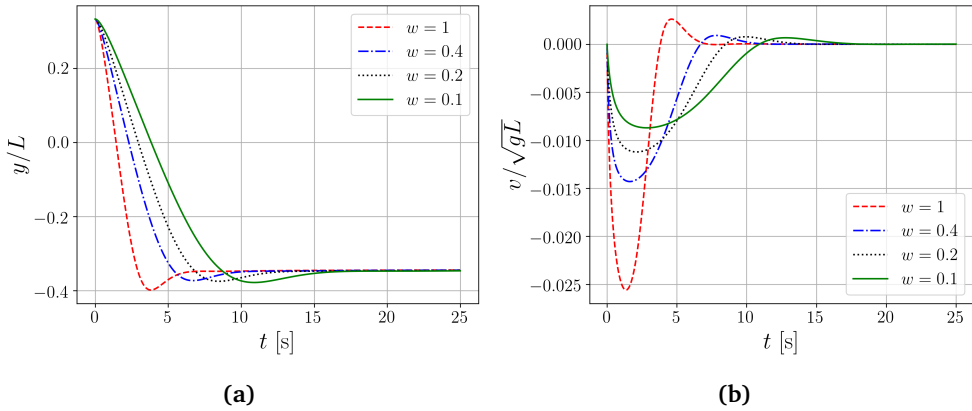
Figure 4.8.: Effect of aspect ratio on the temporal evolution of a spheroidal particle (a) position and (b) velocity. All particles have an equivalent diameter of $d_{p,e} = 4 \, \text{mm}$ and mass density $\rho_p = 1434 \, [\text{kg/m}^3]$.

(a) $w = 1$

(b) $w = 0.1$

Figure 4.9.: Temporal evolution of non-dimensional added mass, static drag, Basset history, and combined gravity and buoyancy force during the sinking motion of a spheroidal particle with (a) $w = 1$ (sphere) and (b) $w = 0.1$. Forces are normalized according to $F^* = F / ((\rho_p - \rho_f)V_p g)$.

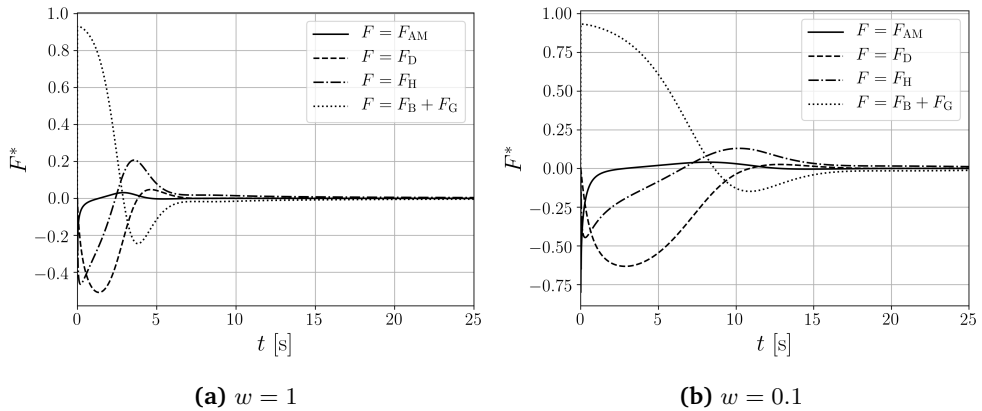at the top of the tank, and particle p_4 with $\rho_{\mathrm{p},4} = 1407$ kg/m^3 is released at the bottom. To characterize the collisions, we define the impact factor as $\mathcal{I} = \frac{\mathrm{LCD}}{d_{\mathrm{major}}}$, where $\mathrm{LCD} = \|\boldsymbol{x}_{14} - \boldsymbol{x}_{14} \cdot \boldsymbol{e}_y\|$ is the lateral distance between the centres of the two particles, where $\boldsymbol{x}_{14} = \boldsymbol{x}_1 - \boldsymbol{x}_4$ is the distance vector between the two particles and d_{major} is the equatorial diameter of the particles. Due to the low particle volume fraction, the two-way momentum coupling in the numerical model is switched off. Moreover, considering the fact that the binary normal Stokes number during immersed collisions in the MnCl_2 solution remains below 10 (see Chapter 2), the effective coefficient of normal restitution for 1:2 particles is set to a constant value of $e_{\mathrm{eff}} = 0.1$ [67, 68]. Simulations are performed with three values of the lubricated friction coefficient of $\mu_{\mathrm{fric}} = 0.005$, $\mu_{\mathrm{fric}} = 0.05$ and $\mu_{\mathrm{fric}} = 0.2$. The best agreement with the experimental results is obtained if $\mu_{\mathrm{fric}} = 0.05$. Several collision experiments are performed to obtain collisions with different impact factors in the range $0 < \mathcal{I} < 1$. For visualization purposes, three collision scenarios with initial particle distance vectors in $x-$ direction are presented here. In figure 4.10, the numerically-obtained vertical particle positions obtained with $\mu_{\mathrm{fric}} = 0.05$ are compared with the experimental results. We observe that the numerical model can predict the experimentally observed particle trajectories in these three collision scenarios. The experimentally-obtained post-collision particle velocities are, however, slightly lower than those in the experiments. The reason for these differences can be explained from the particle snapshots for the case with For $\mathcal{I} = 0.06$ shown in figures 4.11 and 4.12.

As can be seen in the experimental snapshots in figure 4.11, in the scenario with $\mathcal{I} = 0.06$, once the particles reach each other, for a short while ($3.46 < t < 3.81$), they tend to stick and rotate together around the z-axis. The rotational motion of the rising particle is more pronounced than of the sinking particle. At $t = 4.53$, the rising particle has undergone a rotation of more than $90°$, whereas the sinking particle has started to recover its initial broadside orientation. In the numerical predictions, the rotation of the particles due to the collisions is less strong. Especially for the rising POM particle, the difference in the dynamics of the rotational motion can be clearly seen. The rotation of the rising particle around the z- axis remains below $90°$, and at $t \approx 4.90$ the two particles leave each other with almost the same orientations. The differences in the rotational motion of the particles between the numerical and experimental results lead to differences in the post-collision linear motions. The numerically-obtained results for the collision scenario with $\mathcal{I} = 0.32$ are shown in figure 4.12. For this scenario, we observe a better agreement between the numerical and experimental results, indicating the better performance of the numerical model at smaller impact factors. The discrepancies between the numerically and experimentally-obtained rotational motions can be attributed to multiple reasons. First, as observed in the binary collision experiments of spherical particles, the non-uniformity of the magnetic field in the off-centre region of the tank leads to magnetically-induced lateral forces and torques (for non-spherical particles) which are not captured in the numerical model. Second, any small disturbance in the fluid affects the fluid-particle interactions, and therefore the motion of particles in the experiments (especially in regions with low magnetic field gradient), making control and reproduction of the collision experiments very difficult. Third, the discrepancy in the results can also be due to the inaccuracy of the rotational resistance torque model. The model is derived for 5:2 prolate spheroids which are expected to have a larger average rotational resistance than 1:2 particles [154]. This leads to a less pronounced rotation of the particles in the numerical results. Application of more
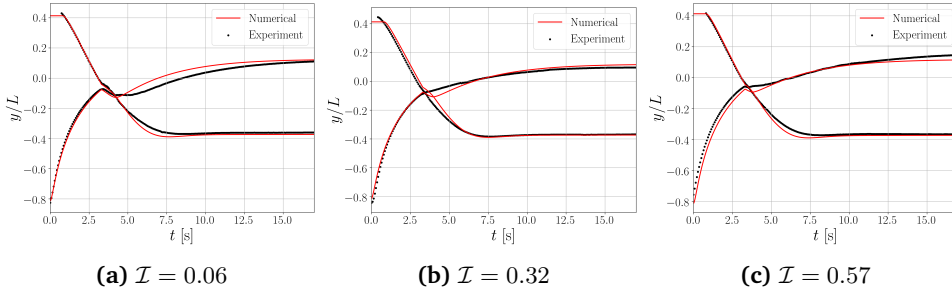
(a) $\mathcal{I} = 0.06$ **(b)** $\mathcal{I} = 0.32$ **(c)** $\mathcal{I} = 0.57$

Figure 4.10.: Temporal evolutions of vertical positions of 1:2 spheroids during binary collisions between a rising PVC-U particle and a falling POM particle with three different impact factors. Experimentally and numerically-obtained snapshots of the particles for cases **(a)** and **(b)** are shown in figures 4.11 and 4.12 respectively.

accurate shape-specific correlations for 1:2 spheroids is expected to improve the numerical predictions, but presently they are not available and need to be derived. Last but not least, our numerical model neglects lubrication effects, which are important during the contact time of two non-spherical particles [68].

Comparing the experimental results of binary collisions between 1:2 spheroids to those of spheres addressed in Chapter 2 reveals that compared to spherical particles, the delay time due to a collision between 1:2 spheroids behaves differently with the impact factor. On average, the hampering effect of collisions on the levitation motion of spheroidal particles is less severe. Binary collisions between two spheres with $\mathcal{I} \in [0,1]$, yield an average increase of about 15% in the levitation time of the sinking particle. For the rising particle, this average increase is as high as approximately 33%. For 1:2 spheroids, the average experimentally observed delays for $\mathcal{I} \in [0,1]$ are roughly -7% and 33% for the sinking and rising particle, respectively. This indicates that Binary collisions of 1:2 spheroidal particles can even yield a net reduction in the levitation time. At high impact factors, i.e. $\mathcal{I} \in [0.6, 1]$ the delay time of both sinking and rising particles is positive and decreases with the impact factor. At low impact factors, i.e. $\mathcal{I} \in [0, 0.6)$, the same behaviour is observed for the rising particle. However, for the sinking particle, the average delay time is negative. The drag reduction due to particle rotation is responsible for the net acceleration at low impact factors for the sinking particle.

4.5.3. Many-particle systems

In this section, we apply the numerical model to study many-particle systems in which mixtures of spheroidal particles are separated. We consider a two-magnet magnetofluidic configuration similar to the one presented in Chapter 4 for studying the separation of spherical particles: A rectangular channel with height $2L$ and two walls at $y/L = \pm 1$ which move with mean streamwise flow velocity $U_0 \boldsymbol{i}$ (see figure 4.13 **(a)**). Two equal ideal Halbach arrays are mounted at the top and the bottom of the channel with their strong sides facing each other. The magnetic field for this configuration is described

Figure 4.11.: Experimentally and numerically-obtained snapshots of two colliding spheroidal particles with $\mathcal{I} = 0.06$ (initial offset is in x-direction). The sinking PVC-U (grey) particle has mass density $\rho_{\mathrm{p},1} = 1436\ \mathrm{kg/m^3}$ and the mass density of the rising POM (black) particle is $\rho_{\mathrm{p},1} = 1407\ \mathrm{kg/m^3}$. Once the two spheroidal particles touch each other, they rotate around one another in $-\boldsymbol{k}$ direction. The rotation of the rising particle is more pronounced. This particle has rotated over $180°$ at $t \approx 4.3$ s. The changes in orientation lead to a reduced drag force and therefore higher acceleration in y- direction after the collision, a phenomenon which does not occur for spherical particles.
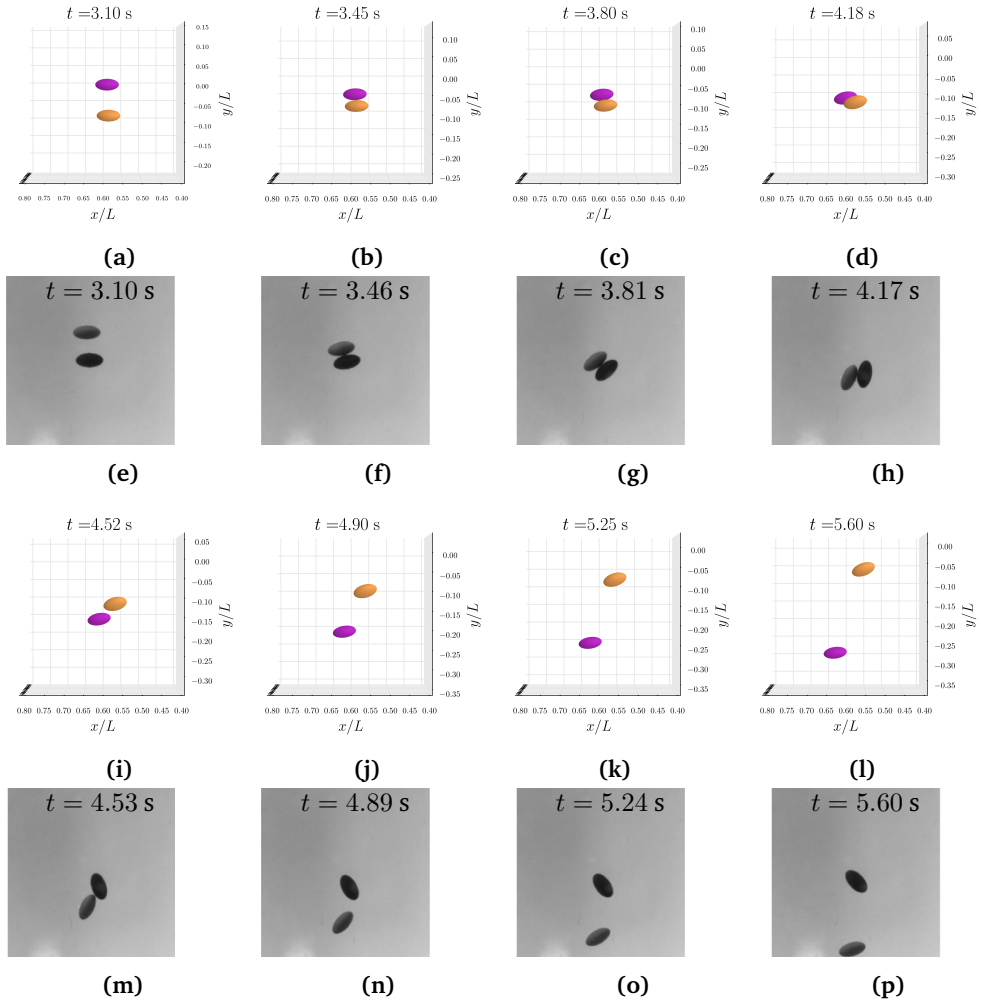
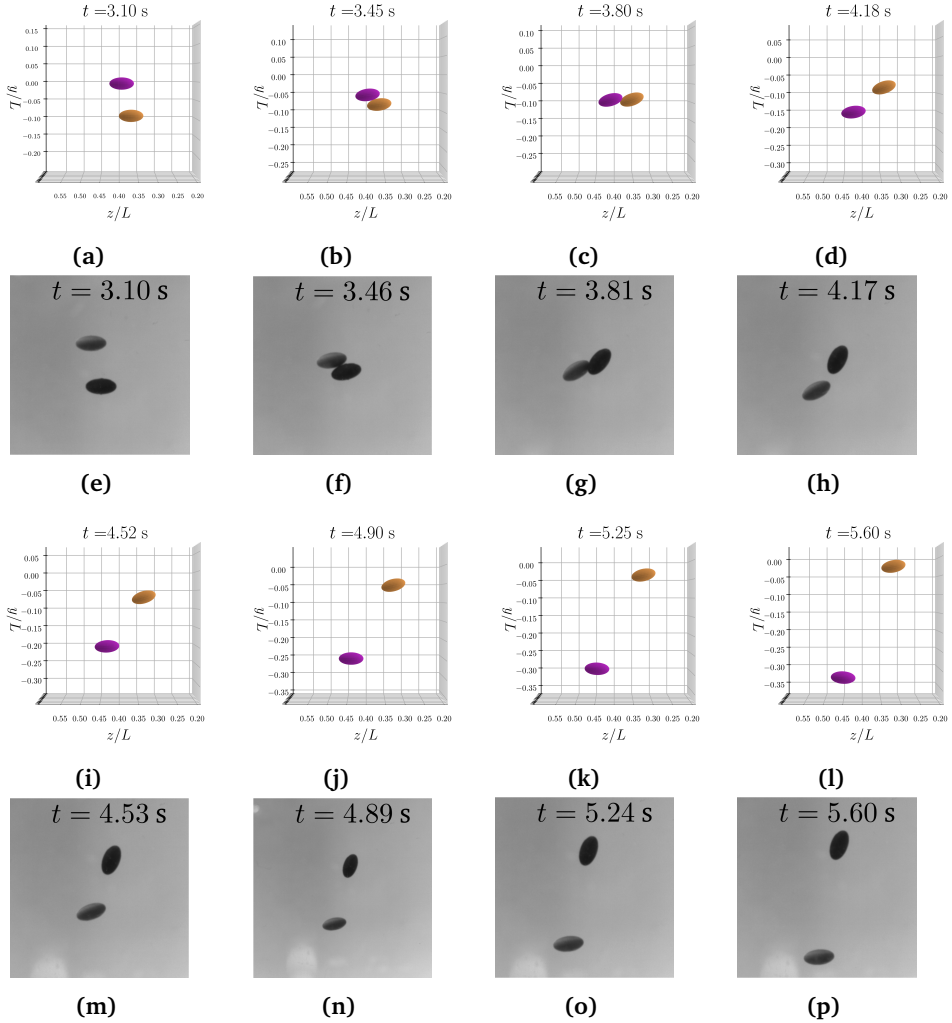**Figure 4.12.:** Experimentally and numerically-obtained snapshots of two colliding spheroidal particles with $\mathcal{I} = 0.32$ ($\boldsymbol{x}_{14}/d_{\mathrm{major}} = -0.1\boldsymbol{e}_x - 0.3\boldsymbol{e}_z$). At this impact parameter, discrepancies between the the numerically and experimentally-obtained particle orientations are smaller due to the weaker particle-particle interaction.

ρ_{f} [kg/m^3]	1.4×10^3
μ_{f} [kg/m/s]	5.54×10^{-3}
χ_{f}	7×10^{-4}
L [m]	0.075
p [m]	0.2
H_0[kA/m]	637
e_{eff}	0.1

Table 4.2.: Parameters used for the many-particle simulations

by

$$H(y) = H_0 \left(e^{-\pi(L+y)/p} + e^{-\pi(L-y)/p} \right), \quad y \in [-L, L], \qquad (4.26)$$

where p is the pole size of the magnets, and H_0 is magnetic field strength at the surface of the strong side of a single magnet. The physical parameters of the system are summarized in table 4.2. The profiles of the induced magnetic field strength and the corresponding apparent mass density of the fluid are shown in figure 4.13 (b).

We assume a uniform initial flow field without any disturbance. The linear and angular momentum transfer between the particles and the fluid are taken into account by considering the two-way momentum coupling strategy described in section 4.2.3. The equations of motion of the fluid and the particles are solved in a frame moving with constant velocity $U_{\mathrm{frame}} = U_0 i$. In this frame, the walls are at rest, and the mean streamwise flow velocity is zero. No-slip boundary conditions are imposed at $y/L = \pm 1$, and in the streamwise and spanwise directions periodic boundary conditions are considered. For a more realistic initial particle distribution, similar to the cases considered in Chapter 2, particles are initially split into two groups of light and heavy particles. Particles lighter than the fluid are injected at $0.75 < y/L < 1$ and particles heavier than the fluid are injected at $-1 < y/L < -0.75$. In addition, an initial impurity of 10% is considered in each particle group. This means that 10% of the particles in the "light" group are heavy and vice versa. All particles are initially released with broadside orientation with zero initial linear and angular velocities.

The volumetric particle concentration is fixed at 1%, which results in a total of 1104 particles in the considered computational domain. Based on the results of the section 4.5.2, the average effective coefficient of normal restitution is set to $e_{\mathrm{eff}} = 0.1$, and the average lubricated friction coefficient to $\mu_{\mathrm{fric}} = 0.05$. We investigate the effect of non-sphericity on the time-dependent behaviour of particle distribution by considering monodispersed spheroidal particles with three different aspect ratios i.e. $w = 1$, $w = 0.5$, and $w = 0.1$. To isolate the effects of particle shape and collisions, we keep the volume of a single particle and the volumetric particle concentration in the domain equal. The diameter of the volume-equivalent spherical particle is $d_{\mathrm{e}} = 4$ mm. This yields equatorial diameters of $d_{\mathrm{major}} = 5.04$ mm and $d_{\mathrm{major}} = 8.61$ mm for the 1:2 and 1:10 spheroids respectively.

Five cases are considered in total. In case 1, particles are spheres. In cases 3 the particle aspect ratio is reduced to $w = 0.5$. To investigate the effect of collisions on the separation performance, in cases 2 and 4 we perform the simulations without particle-
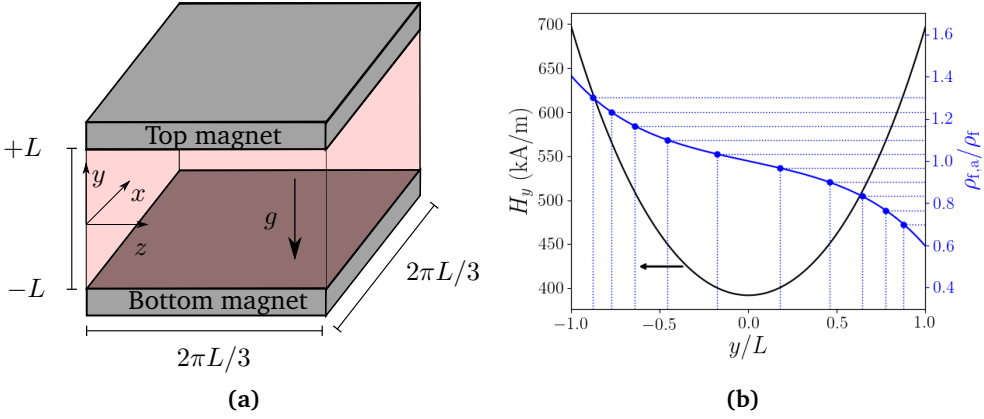
(a)   **(b)**

Figure 4.13.: (a) A schematic of the computational domain for the many-particle sim-
ulations. In a frame moving with the same velocity as the conveyor
belts, $U_0\boldsymbol{i}$, the mean streamwise velocity of the fully-developed flow is
zero. In this frame, the walls at $y = \pm L$ are at rest. **(b)** Magnetic field
strength profile and the corresponding profile of the effective mass den-
sity of the magnetic fluid. The dotted lines indicate mass densities of
the particles. The dashed lines correspond to the considered cut mass
densities.

Case	Φ	d_{e}[mm]	d_{major}[mm]	No. of particles	w	Im	collisions
1	0.01	4	4.00	1104	1.0	0.1	yes
2	0.01	4	5.04	1104	1.0	0.1	no
3	0.01	4	5.04	1104	0.5	0.1	yes
4	0.01	4	5.04	1104	0.5	0.1	no
5	0.01	4	8.61	1104	0.1	0.1	no

Table 4.3.: Summary of physical parameters for all test cases.

particle collisions. As the particle aspect ratio decreases, resolving particle-particle
collisions becomes more challenging, because the collision detection and collision se-
quence algorithms presented in section 4.2.1.3 not always converge for some specific
collision scenarios. Non-converged solutions of the collision detection algorithm in
many-particle systems can lead to nonphysical particle properties and eventually, a
simulation crash. To avoid such problems for the case with $w = 0.1$, we performed
only one simulation without inter-particle interactions. Improvements to the binary
collision detection and TOI algorithms will be studied in future to make them appli-
cable to such highly anisotropic particles. The physical quantities of the considered
cases are summarized in table 4.3.

4.5.3.1. Particle distribution

Figure 4.14 shows the front views of particles at $t \in \{0.01, 0.5, 1, 1.5, 2, 2.5\}$ for case
3. The vertical colour bars indicate the particle mass density ratio, $\rho_{\mathrm{p}}/\rho_{\mathrm{f}}$. As the

particles travel to their equilibrium positions, they rotate due to interactions with the surrounding fluid and other particles. Changes in the orientation of particles, in turn, influence their interactions with the fluid and their levitation dynamics.

To gain more quantitative insight into the differences in the local particle distributions, in Figure 4.15 the probability density function of vertical particle position for the considered five cases are compared at different times. As the particle aspect ratio decreases the particle dispersion in y- direction increases. This effect is stronger in the central region of the channel where the magnetic buoyancy force is weaker. After 2 seconds, only mass density groups with equilibrium positions located closest to the walls ($|1 - \rho_{\mathrm{p}}/\rho_{\mathrm{f}}| = 0.3$) have a similar separation performance for different aspect ratio. This is to be expected, as first, the initial vertical position of particles in theses groups are closest to their equilibrium positions. Second, the stabilizing magnetic buoyancy force in the vicinity of the walls is stronger. Therefore, theses particle groups have the shortest separation time scale. For particles in mass density range $|1 - \rho_{\mathrm{p}}/\rho_{\mathrm{f}}| = 0.7$ only after 1 second a clear difference is observed in both the average vertical position and its variance for 1:1 and 1:2 particles. This difference is much larger for 1:10 particles which indicates the inferior separation performance of low-aspect-ratio particles. One should note that this holds even though collisions are neglected in case 5. Including the effects of collisions is expected to deteriorate the separation performance further. As due to the larger contact areas, such flat particles tend to stick to each other during the collisions causing larger hindrance. Based on these observations, one can conclude that injecting the particles in the central region of the channel instead of in the vicinity of walls can lead to more uniform separation time scales among different mass density groups and particle shapes.

The influence of two-way coupling on particle rotational dynamics can clearly be observed in case 5, where particle-particle interactions are neglected. Figure 4.16 **(a)** shows the particle-induced velocity field in a cross-section of the domain in case 5 at $t \in \{1.5, 2.5, 5.99\}$. Although the particles do not directly "feel" each other through collisions, they indirectly influence each other through the particle-induced velocity disturbances. The flow-induced rotation of the particles can seen in figure 4.16 **(b)**.

4.5.3.2. System separation performance

We evaluate the overall separation performance of a system by computing a mean separation error defined as

$$e_{\mathrm{m}}(t) = \frac{1}{L}\sqrt{\frac{1}{N_{\mathrm{p}}}\sum_{i=1}^{N_{\mathrm{p}}}(y_{\mathrm{p},i}(t) - y_{e,i})^2}, \qquad (4.27)$$

where N_{p} is the total number of particles, $y_{\mathrm{p},i}(t)$ the position of particle i at time t, and $y_{e,i}$ is its equilibrium height. The temporal evolution of the mean separation errors are compared in figure 4.17.

At a given time, the smaller the aspect ratio, the larger is the mean separation error. Because of the larger average drag force acting on non-spherical particles in broadside orientation, decreasing the aspect ratio from 1 to 0.1 decreases the reduction rate of
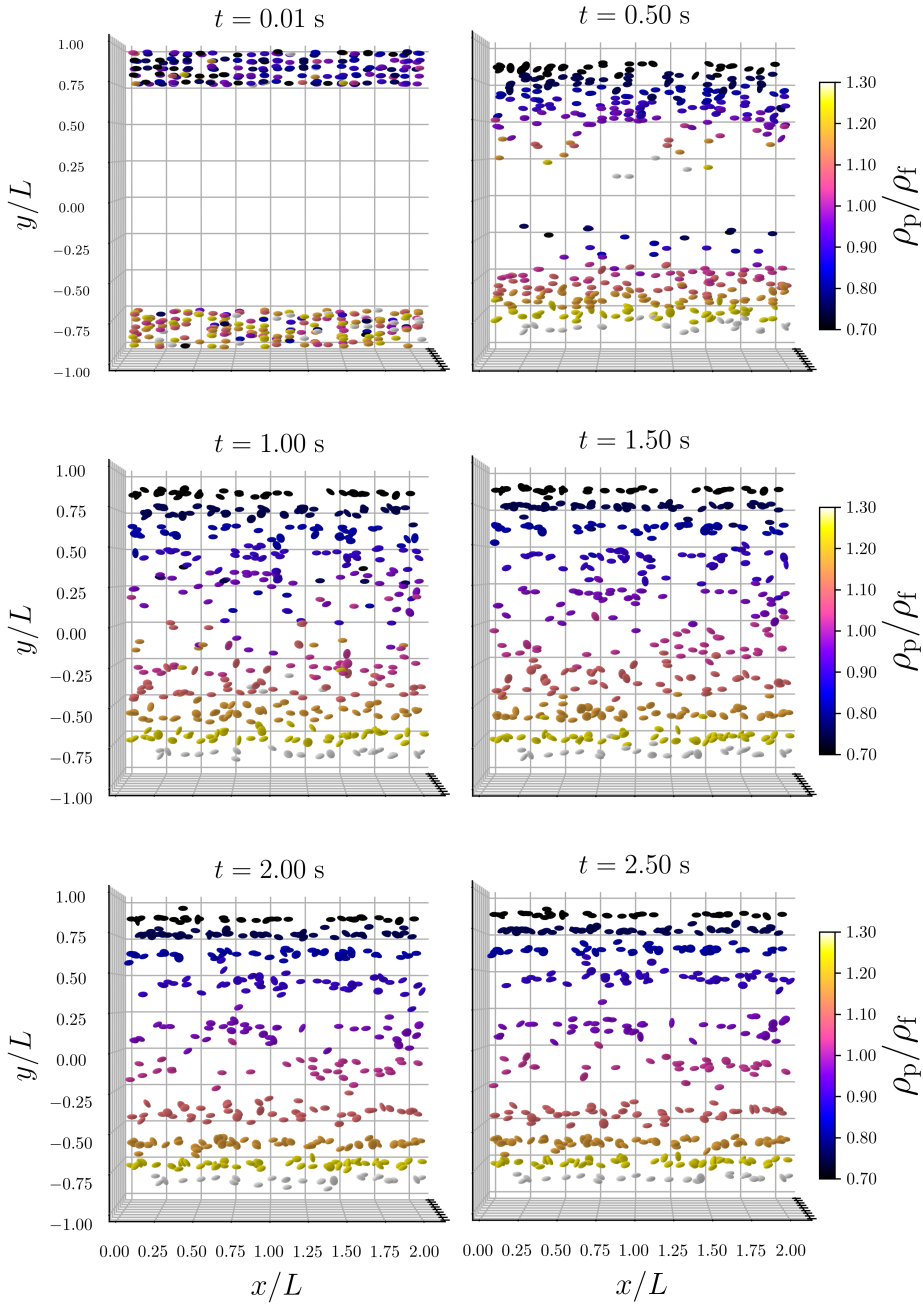
Figure 4.14.: Projections of the particles in the region $|z - \frac{L_z}{2}| < 3d_{\mathrm{p},e}$ (Case 3). The vertical colour bars indicate to the particle mass density ratio $\rho_{\mathrm{p},e}/\rho_{\mathrm{f}}$.

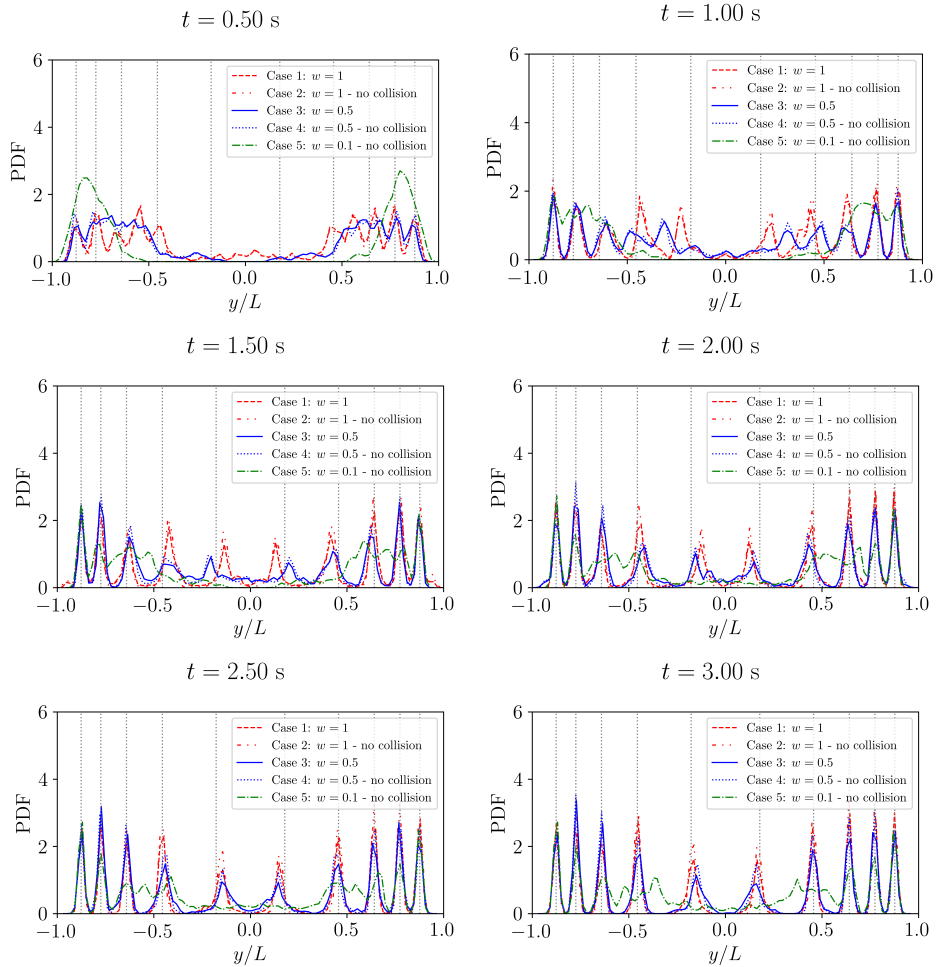**Figure 4.15.:** Evolution of probability density function of particle position for cases 1, 2, 3, 4 and 5 at various time instances.
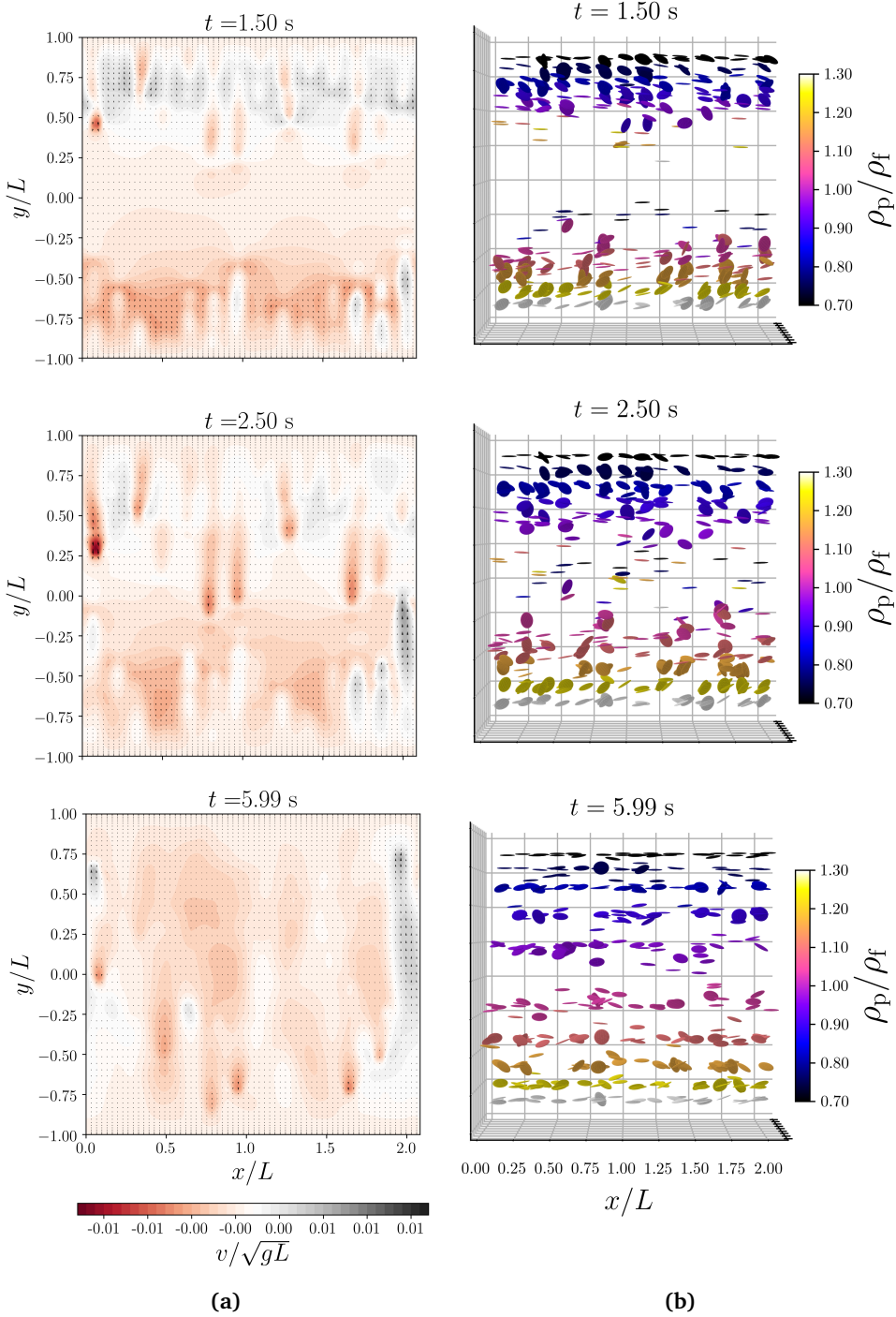
Figure 4.16.: (a) Cross-sections of the velocity field in the moving frame at $z = \frac{L_z}{2}$. The horizontal colour bar corresponds to the wall-normal component of the particle-induced fluid velocity.**b** Projections of the particles in the region $|z - \frac{L_z}{2}| < d_{p,e}$ for case 5.
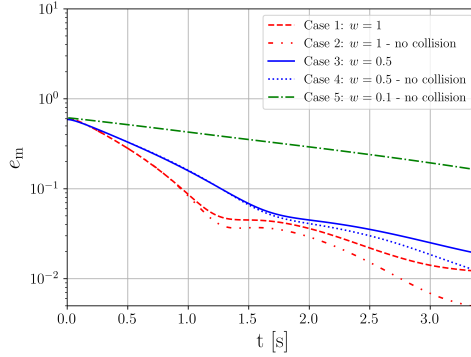
Figure 4.17.: The effects of collisions and particle aspect ratio on the temporal be-
haviour of the mean separation error.

the average separation error during the time interval $0 \leq t \leq 1$ s. After $t = 1$ s the
reduction rate of the separation error decreases for spheres, due to the stronger over-
shoot of the particle equilibrium position by the history force for spherical particles.
This leads to a similar separation performance during the interval $1.5 \leq t \leq 2$. At
later times, i.e. $t > 3$, as the particles approach their equilibrium positions, the decay
behaviour of the average separation error for 1:1 and 1:2 spheroids is similar. This is
due to the reduction of the sensitivity of average drag coefficient to the particle aspect
ratio at low Reynolds numbers (see chapter 3).

When collisions are neglected, the mean separation error for 1:1, 1:2 and 1:10 parti-
cles are respectively 0.006, 0.018 and 0.193 at $t \approx 3$. Furthermore, we observe that the
influence of collisions on the system separation performance is more pronounced for
spherical particles. After 3 s, neglecting inter-particle interactions yields 51% under-
estimation of the average separation error for spherical particles, but this underesti-
mation reduces to 26% for 1:2 spheroids. We attribute this difference to two reasons;
firstly, the collisions have a larger hampering effect on the faster spherical particles.
Second, as observed in binary collisions presented in section 4.5.2, changes in the ori-
entation of non-spherical particles due to the collisions can lead to a reduction in the
average drag force on a particle. This effect reduces the hindering effect of collisions
for non-spherical particles.

4.6. Conclusions and outlook

In this chapter, we presented and employed a numerical framework for modelling
flows of magnetized liquids laden with ellipsoidal particles. The presented point-
particle Euler-Lagrange approach incorporates the relevant force and torque models
for interactions of ellipsoidal particles with a magnetized paramagnetic liquid. The
model considers two-way angular and linear momentum transfer between the parti-
cles and the fluid. Moreover, a hard-sphere collision model is incorporated to capture
the inter-particle interactions between ellipsoidal particles. We validated our numeri-
cal model by particle tracking experiments performed in a magnetized paramagnetic

fluid. The good agreement between the numerical and experimental results of the particle tranlational motion proves the promising capability of the presented numerical framework in modelling the dynamics of non-spherical particles in magnetic density separator systems. However, to accurately capture the rotation of particles, this framework should be equipped with more accurate torque models.

The effect of nonsphericity on particle levitation dynamics in single-, two- and many-particle is investigated. In the single-particle systems, it is shown that decreasing the particle aspect ratio from 1 to 10 can lead to up to 146% increase in the levitation time of a spheroid moving at the broadside orientation. The effect of particle nonsphericity on particle-particle interactions is studied by comparing the numerical results of binary collisions between 1:2 spheroids with experimental observations.

Because of the changes in the orientation of 1:2 spheroids during collisions, it is found that compared to spheres, the hampering effect of a binary collision with the same impact factor is smaller for 1:2 spheroids. Due to the challenges in experimentally obtaining controlled collision scenarios, however, one-to-one comparison of the numerical and experimental results turned out to be very challenging. The collision model has shown to be capable of reproducing the experimentally observed translational motion of 1:2 spheroids during binary collisions. Differences are, nevertheless, observed in the experimentally and numerically obtained rotational motion of particles during and after the collisions.

Results of the many-particle simulations revealed that the separation efficiency of spheroidal particles decreases as the particle anisotropy increases. Moreover, the separation performance of 1:2 spheroids was shown to be less affected by inter-particle interactions.

Results of the present chapter shows that particle nonsphericity further complicates the magneto-hydrodynamic interactions between the particles and the magnetized fluid. As the isotropy of the particles decreases, the coupling between the linear and angular motions of the particle increases. Hence, accurately predicting the rotational motion of particles is of great importance at low aspect ratios. In improving the numerical predictions for the rotational motion of particles deriving more accurate shape-specific models for rotational resistance torque is recommended as a direction for future research. Furthermore, incorporation of the model presented in this work in non-uniform time-dependent flows may require considering the effects of local velocity gradients, and time-dependent rotational effects (e.g. rotational history and added mass) in the numerical model. Models for shear-induced or transient hydrodynamic interactions of anisotropic particles are very scarce. Besides, the applicability of the existing models is limit ted to creeping-flow regimes. Developing new models for such interactions can be considered as another direction of future research.

4.A. Force and torque correlations

In this appendix, shape-specific correlations for force and torque coefficients used in the numerical model are presented.

	w = 0.4			w = 0.2			w = 2.5	w = 0.2
	Drag	Lift	Pitch. torque	Drag	Lift	Pitch. torque	Rot. torque	Rot. torque
	(4.29)(4.30)	(4.31)	(4.32)	(4.34)(4.35)	(4.36)	(4.37)	(4.38)	(4.38)
	$a_1 = 24.66$	$b_1 = 5.28$	$c_1 = 3.643$	$a_0 = 1.96$	$b_1 = 12.11$	$c_1 = 3.872$	Mode 1	Mode 1
	$a_2 = 4.059$	$b_2 = 8.96$	$c_2 = 0.178$	$a_1 = 5.82$	$b_2 = 1.036$	$c_2 = 0.237$	$r_1 = 0.23$	$r_1 = 3.82$
	$a_3 = 0.349$	$b_3 = 0.2348$	$c_3 = -1.252$	$a_2 = 0.44$	$b_3 = 3.887$	$c_3 = 2.351$	$r_2 = -0.116$	$r_2 = -0.13$
	$a_4 = 0.0007$	$b_4 = -8.095$	$c_4 = 0.319$	$a_3 = 15.56$	$b_4 = 0.109$	$c_4 = 0.236$	$r_3 = 96.378$	$r_3 = 283.3$
	$a_5 = 0.278$	$b_5 = 0.325$	$c_5 = -0.018$	$a_4 = 1.068$	$b_5 = 0.812$	$c_5 = -0.394$	$r_4 = 1.0$	$r_4 = 1.0$
	$a_6 = 30.18$	$b_6 = -0.004$	$c_6 = 0.387$	$a_5 = 35.41$	$b_6 = 0.249$	$c_6 = 1.615$	Mode 2	Mode 2
	$a_7 = 4.396$	$b_7 = 0.352$	$c_7 = 0.004$	$a_6 = 0.96$	$b_7 = -0.198$	$c_7 = -0.044$	$r_1 = 71.03$	$r_1 = 13.31$
	$a_8 = 0.156$	$b_8 = -0.002$	$c_8 = 0.349$	$a_7 = 3.63$	$b_8 = 5.821$	$c_8 = -0.537$	$r_2 = 0.069$	$r_2 = 0.189$
	$a_9 = 0.0073$	$b_9 = 0.273$	-	$a_8 = 0.05$	$b_9 = -4.717$	$c_9 = 1.805$	$r_3 = 773.04$	$r_3 = 783.05$
	$a_9 = 1.469$	-	-	-	$b_{10} = 0.007$	$c_{10} = -0.037$	$r_4 = 0.67$	$r_4 = 0.628$

Table 4.4.: Coefficients in correlations of Zastawny et al. [154] and Sanjeevi et al. [120] for force and torque coefficients.

Drag, lift and pitching torque coefficients of 1:2 and 2:5 oblate spheroids follow the correlation proposed by Sanjeevi et al. [120] for 2:5 spheroids. The drag coefficient reads:

$$C_{D,\phi} = C_{D,\phi=0^\circ} + (C_{D,\phi=90^\circ} - C_{D,\phi=0^\circ})\sin^2(\phi), \tag{4.28}$$

where

$$C_{D,\phi=0^\circ} = \left(\frac{a_1}{Re} + \frac{a_2}{Re^{a_3}}\right)e^{-a_4 Re} + a_5\left(1 - e^{-a_4 Re}\right), \tag{4.29}$$

$$C_{D,\phi=90^\circ} = \left(\frac{a_6}{Re} + \frac{a_7}{Re^{a_8}}\right)e^{-a_9 Re} + a_{10}\left(1 - e^{-a_9 Re}\right). \tag{4.30}$$

The lift coefficient follows

$$C_{L,\phi} = \left(\frac{b_1}{Re} + \frac{b_2}{Re^{b_2}} + \frac{b_4}{Re^{b_5}}\right)\sin(\phi)^{\left(1 + b_5 Re^{b_7}\right)}\cos(\phi)^{\left(1 + b_8 Re^{b_9}\right)}, \tag{4.31}$$

and the pitching torque coefficient follows

$$C_{T,\phi} = \left(\frac{c_1}{Re^{c_2}} + \frac{c_3}{Re^{c_4}}\right)\sin(\phi)^{\left(1 + c_5 Re^{c_5}\right)}\cos(\phi)^{\left(1 + c_7 Re^{c_8}\right)}. \tag{4.32}$$

Coefficients a_1-a_5, b_1-b_9 and c_1-c_8 are provided in table 4.4.

The drag, lift and pitching torque coefficients of 1:5 oblate spheroids follow the correlations of Zastawny et al. [154]. The drag coefficient reads

$$C_{D,\phi} = C_{D,\phi=0^\circ} + (C_{D,\phi=90^\circ} - C_{D,\phi=0^\circ})\sin^{a_0}\phi, \tag{4.33}$$

where

$$C_{D,\phi=0^\circ} = \left(\frac{a_1}{Re^{a_1}} + \frac{a_3}{Re^{a_4}}\right), \tag{4.34}$$

$$C_{D,\phi=90^\circ} = \left(\frac{a_5}{Re^{a_6}} + \frac{a_7}{Re^{a_8}}\right). \tag{4.35}$$

The lift coefficient reads:

$$C_{L,\phi} = \left(\frac{b_1}{Re} + \frac{b_2}{Re^{b_2}} + \frac{b_4}{Re^{b_5}}\right)\sin(\phi)^{\left(1 + b_5 Re^{b_7}\right)}\cos(\phi)^{\left(1 + b_8 Re^{b_9}\right)}, \tag{4.36}$$

and the torque coefficient reads:

$$C_{T,\phi} = \left(\frac{c_1}{Re^{c_2}} + \frac{c_3}{Re^{c_4}} \right) \sin(\phi)^{(C_5 + c_6 Re^{c_7})} \cos(\phi)^{(c_8 + c_9 Re^{c_{10}})}. \qquad (4.37)$$

The rotation resistance torque coefficients of 1:2 and 1:10 oblate spheroids follow the correlations of Zastawny et al. [154] for 5:2 prolate spheroids 2:10 oblate spheroids respectively. These correlations read:

$$C_R = r_1 Re_r^{r_2} + \frac{r_3}{Re_r^{r_4}}, \qquad (4.38)$$

where Re_r is the rotational Reynolds number defined in section 4.2, and coefficients r_1-r_4 are provided in Table 4.4. Zastawny et al. [154] identified two different modes for the rotational torque. In mode 1, the rotation takes place around the spheroids major axis, and in the second mode, rotation occurs around an axis perpendicular to the particle axis of symmetry. Rotations in mode 1, i.e. rotations around the symmetry-axis are not considered in this study.

For steady drag, lift, and pitching torque on 1:10 spheroids the DNN-based correlation of Tajfirooz et al. [138] is used.

5. Conclusions and recommendations

Mechanical recycling is the representative approach to recover plastics. Obtaining a high-quality single polymer stream from plastic waste is predominantly dependent on the performance of separation techniques. Magnetic density separation is a high-resolution mass-density-based sorting process which is realised by incorporating a combination of a magnetic liquid and a properly designed magnetic field. MDS exploits the magneto-Archimedes principle in magnetised fluids to fractionate a mixture of material based on minimal differences in the mass density of sub-populations. In adapting the MDS strategy, special care should be taken to interactions of dispersed particles with each other as well as with the background flow. Optimisation of MDS processes, therefore, requires a fundamental understanding of such interactions. This work aimed at the development and application of an efficient numerical framework for studying the buoyancy-driven motion of particles in a flow of magnetised liquid, a phenomenon common in industrial MDS systems. We combined point-particle Euler-Lagrange (PP-DNS) numerical simulations with experimental observations to obtain a fundamental understanding of the collective motion of particles in flows of magnetic fluids exposed to a steady non-uniform magnetic field. This chapter summarises the most important conclusions that are drawn in this dissertation.

5.1. Conclusions

First and foremost, this dissertation provides a profound understanding of the underlying fluid-structure mechanisms to describe the motion of almost neutrally-buoyant particles in magnetised fluids. We demonstrated that the buoyancy-driven motion of a particle in magnetic liquid can be described by a non-autonomous system, the critical point of which corresponds to the equilibrium position of the particle. Through an eigenvalue analysis, we parameterised the motion of a single spherical particle in the absence of history effects. We showed how a single particle can exhibit either a monotonic or oscillating behaviour as it travels toward its equilibrium point. By comparing the numerical and experimental results, we determined that the Basset history force plays an essential role in the motion of almost neutrally buoyant spherical particles at large diameters. We quantified the effect of binary collisions on levitation dynamics of spheres and illustrated that disregarding collisions can lead to a spuriously low particle dispersion in the numerical results of large MDS systems. Disregarding history force was shown to result in a significant under-prediction of the time to achieve a certain level of separation. Moreover, the numerical results showed that at the volume fractions considered in this work, particle-induced flow disturbances do not have a remarkable effect on the separation performance of spherical particles.

The fidelity of the point-particle Euler-Lagrange (PP-DNS) simulations is highly dependent on the accuracy of incorporated models for the hydrodynamic interaction of particles with the surrounding fluid. Due to the complexity and non-linearity of these interactions for non-spherical particles at high Reynolds numbers, models for these interactions are scarce. Especially at high particle anisotropies, predicting forces and

torques acting on a particle during the arbitrary motion in a viscouse fluid becomes more challenging. In Chapter 3, we employed a statistical learning approach to develop for the first time, correlations for the steady hydrodynamic interaction of 1:10 oblate spheroids. Not only is the proposed methodology not prone to undesired biases introduced by using conventional curve-fitting approaches, but it also does not require a priori knowledge of the type of correlating functions. Our results prove the capability of a well-trained deep neural network (DNN) architecture in predicting hydrodynamic interactions of anisotropic particles.

Extending the applicability of the PP-DNS framework to MDS of non-spherical particles is discussed in Chapter 4. We presented a new strategy for the two-way torque-coupling between ellipsoidal particles and the continuous phase where the particle size and the Eulerian grid size are in the same order. Inspired by the immersed boundary approach, the proposed method converts the particle torque on the fluid to a set of point forces which act on the grid points in the neighbourhood of the particle centre. Furthermore, we combined a hard-ellipsoid collision model with an iterative contact detection algorithm to capture the immersed particle-particle interactions. Our PP-DNS framework uses the DNN correlations derived in Chapter 3 and other existing shape-specific models to capture the hydrodynamic interactions of spheroidal particles. Results of the application of the model to oblate spheroids with different aspect ratios showed that the levitation time of single particles is inversely proportional to the aspect ratio. The history force is shown to remain an essential contributor to the motion of oblate spheroids. However, due to the smaller acceleration of oblate spheroids, compared to spheres of the same volume, the relative contribution of history force is smaller for spheroidal particles.

The experimental results revealed that compared to spheres, particle-particle interactions are much more complicated for 1:2 spheroidal particles. At low impact factors, spheroidal particles undergo strong rotational motions during a binary collision which can lead to rotations of more than $180°$. The rotational interactions of spheroids were shown to decrease with the impact factor. Changes in the orientation of particles during collisions decrease the effective cross-sectional area of the particles and therefore leads to a net drag reduction. This mechanism which reduces the hampering effect of binary collisions for spheroids is absent for spheres. The proposed numerical framework successfully predicts the experimentally observed translational motion of spheroids in single and two-particle systems. However, our comparisons revealed that capturing the rotational motion of spheroids more accurately requires the incorporation of more accurate shape-specific models for rotational interactions of non-spherical particles.

The stronger fluid-particle interaction is another distinguishing phenomenon in magneto-Archimedes levitation of spheroidal particles. The substantial influence of particle-induced flow disturbances on the neighbouring particles is due to the high sensitivity of the rotational motion of oblate spheroids to small flow disturbances, an effect which increases with decreasing particle aspect ratio.

Major findings of this dissertation that are of direct relevance to the design optimization of MDS systems are summarized below:

- In chapter 2 we observed that decreasing the size of a particle from 4 to 1 mm can

reduce the levitation time of single spherical particles from about 2.5 seconds to approximately 32 seconds. This observation indicates the importance of particle size in MDS processes. Therefore, an accurate estimate of separation time in an MDS system requires prior knowledge about the size distribution of input particles.

- Particle shape is shown to be another critical influence parameter in MDS systems. Results on levitation time of single spheroidal particles (chapter 3) revealed that lowering the particle aspect ratio from 1 (sphere) to 0.1 (disk) yields approximately 150% percent increase in the single-particle levitation time.

- Particle-particles interactions are shown to lead to up to 45% increase in the levitation time of spherical particles during binary collisions. However, in chapter 3, we showed that the delaying effect of binary collisions between 1:2 ellipsoidal particles is weaker. The reason for this is attributed to the change in the orientation of non-spherical particles during collisions. In many-particle systems, collisions are responsible for increasing particle dispersion especially in the central region of the channel.

- DNS results of large MDS systems revealed that the separation performance of almost neutrally buoyant particles with $|1 - \rho_{\mathrm{p}}/\rho_{\mathrm{f}}| < 0.05$ is lower than that of the heavier and lighter particles that levitate closer to the channel walls. This difference can be attributed to the low gradient of the magnetic field in the centre of the channel and a higher possibility of collisions with other particles for almost neutrally buoyant particles.

5.2. Recommendations for future research

The understanding gained through numerical analysis of particle-laden flows in MDS processes has provided valuable insights into the important mechanisms that influence the collective motion of particles in magnetic density separation systems and has laid a foundation for several interesting future research directions. In this section, we address some of the most important topics which have not been explored in this dissertation, but they are recommended for further investigations. First, we discuss our recommendations in the more general context of PP-DNS simulations. Next, we address recommendations which are more specific to the MDS application.

5.2.1. General recommendations

- In this work, we proposed new methods to model the momentum transfer between particles and the continuous phase in the PP-DNS framework. The proposed strategies are mathematically well-founded. However, experimental validation of the physical accuracy of these models is very challenging. In this regard, particle-resolved simulations can be performed to test, and further improve the accuracy of these models, especially for non-spherical particles.

- The two-way angular momentum coupling strategy presented for non-spherical

particles in Chapter 4 takes a single Eulerian grid cell as the coupling volume. Considering the sensitivity of the motion of non-spherical particles to local flow disturbances, the extension of the method to distribute the coupling force over the volume occupied by the particle would better account for the shape and orientation of the particles.

- In this dissertation, we did not address the effect of initial background turbulence on the levitation dynamics of particles. The presented framework can be straightforwardly equipped with suitable initial conditions that describe the flow at the exit of the laminator to study the impact of background turbulence on the particle dynamics.

- The importance of time-dependent interactions such as history force in the motion of almost neutrally buoyant particles in viscous flows is illustrated in detail in Chapter 2 of this dissertation. Moreover, in Chapter 4, it was shown that capturing the experimentally observed rotational motion of particles requires more accurate shape-specific models for the particle rotational resistance. Nevertheless, accurate shape-specific models for time-dependent hydrodynamic interactions and the rotational resistance torque do not exist yet. In addition, in cases where the background flow has strong non-uniformities over the volume of particles, the momentum coupling models should be extended to take the effect of flow non-uniformities into account. Models for the quantitative prediction of shear-induced momentum transfer are also scarce. Using statistical methods similar to the one presented in Chapter 3, data from resolved simulations can be used to create models for these complex interactions. In view of currently available computer capacity, a large amount of data can be generated by particle resolved simulations. Incorporating statistical techniques can transform this PR-DNS data to models which can be efficiently employed in PP-DNS simulations.

- In immersed particle-particle interactions during the phase where the distance between the surfaces of the particles is very small, lubrication forces dominate. We disregarded lubrication effects in this dissertation. Therefore, incorporation of lubrication effects is recommended especially for non-spherical particles where a collision can have a significant influence on the rotational motion of particles.

5.2.2. MDS-specific recommendations

- The simulations performed in this work considered simple 1D magnetic fields. More complex 3D magnetic fields can be straightforwardly incorporated in the model to investigate the effect of more realistic magnetic fields in practical MDS systems.

- Due to the reasons addressed in Chapter 1, the carrier liquid considered in this work is a paramagnetic solution. The effects of the low viscosity and the superparamagnetic behaviour of ferrofluids in industrial MDS systems can be included in the present model. However, one should note that accurate simulations of MDS in a ferrofluid might require introducing models for time-dependent changes in the concentration of nano-particles, and non-equilibrium effects in

the magnetisation behaviour of ferrofluids in turbulent or transient conditions.

- In this study, we measured the magnetic field in the central region of the experimental setup. Extending the information on the profile of the magnetic field strength to a larger area can provide more insight into magneto-hydrodynamic interactions between the particles and the magnetic liquid. This can be achieved by performing additional field measurements or numerical simulations.

Bibliography

[1] M. Abadi, A. Agarwal, P. Barham, E. Brevdo, Z. Chen, C. Citro, G. S. Corrado, A. Davis, J. Dean, Matthieu Devin, et al. Tensorflow: Large-scale machine learning on heterogeneous distributed systems. *arXiv preprint arXiv:1603.04467*, 2016.

[2] M. Abolhassantash, M. M. Tavakol, O. Abouali, M. Yaghoubi, and G. Ahmadi. Deposition fraction of ellipsoidal fibers in the human nasal cavity- influence of non-creeping formulation of hydrodynamic forces and torques. *Int. J. Multiph. Flow*, 126:103238, 2020.

[3] Y. Akiyama and K. Morishima. Label-free cell aggregate formation based on the magneto-archimedes effect. *Appl. Phys. Lett.*, 98(16):163702, 2011.

[4] M. P. Allen and D. J. Tildesley. *Computer simulation of liquids*. Oxford university press, 2017.

[5] P. Anand, Samriddhi S. Ray, and G. Subramanian. Orientation dynamics of sedimenting anisotropic particles in turbulence. *Phys. Rev. Lett.*, 125(3):034501, 2020.

[6] H. I. Andersson and F. Jiang. Forces and torques on a prolate spheroid: low-Reynolds-number and attack angle effects. *Acta Mech.*, 230(2):431–447, 2019.

[7] H. I. Andersson and A. Soldati. Anisotropic particles in turbulence: status and outlook. *Acta Mech.*, 224(10):2219, 2013.

[8] H. I. Andersson, L. Zhao, and M. Barri. Torque-coupling and particle–turbulence interactions. *J. Fluid Mech.*, 696:319–329, 2012.

[9] U. Ts. Andres. Magnetic liquids. *Mater. Sci. Eng.*, 26(2):269–275, 1976.

[10] M. Ardekani, P. Costa, W. P. Breugem, and L. Brandt. Numerical study of the sedimentation of spheroidal particles. *Int. J. Multiph. Flow*, 87:16–34, 2016.

[11] M. N. Ardekani, G. Sardina, L. Brandt, L. Karp-Boss, R. N. Bearon, and E. A. Variano. Sedimentation of inertia-less prolate spheroids in homogenous isotropic turbulence with application to non-motile phytoplankton. *J. Fluid Mech.*, 831: 655–674, 2017.

[12] F. Auguste, J. Magnaudet, and D. Fabre. Falling styles of disks. *J. Fluid Mech.*, 719:388–405, 2013.

[13] G. Bagheri and C. Bonadonna. On the drag of freely falling non-spherical particles. *Powder Technol.*, 301:526–544, 2016.

[14] E. J. Bakker, P. C. Rem, and N. Fraunholcz. Upgrading mixed polyolefin waste with magnetic density separation. *Waste Manag.*, 29(5):1712–1717, 2009.

[15] S. Balachandar and J. K. Eaton. Turbulent dispersed multiphase flow. *Annu. Rev. Fluid Mech.*, 42:111–133, 2010.

[16] Mandy Barker. SOUP series, 2020. URL https://www.mandy-barker.com/soup-2. [Online; accessed 19-January-2021].

[17] A. B. Basset. *A treatise on hydrodynamics: with numerous examples*, volume 2. Deighton, Bell and Company, 1888.

[18] J. Bender and A. Schmitt. Constraint-based collision and contact handling using impulses. In *Proceedings of the 19th international conference on computer animation and social agents*, pages 3–11, 2006.

[19] E. Blums, A. Cebers, and M. M. Maiorov. *Magnetic fluids*. Walter de Gruyter, 2010.

[20] H. Brenner. The stokes resistance of an arbitrary particle. *Chem. Eng. Sci.*, 18 (1):1–25, 1963.

[21] H. Brenner. The stokes resistance of an arbitrary particle—iv arbitrary fields of flow. *Chem. Eng. Sci.*, 19(10):703–727, 1964.

[22] A. L. Brooks, S. Wang, and J. R. Jambeck. The chinese import ban and its impact on global plastic waste trade. *Sci. Adv.*, 4(6):eaat0131, 2018.

[23] S. L. Brunton, B. R. Noack, and P. Koumoutsakos. Machine learning for fluid mechanics. *Annu. Rev. Fluid Mech.*, 52:477–508, 2020.

[24] M. Buzzicotti, F. Bonaccorso, P. C. Di Leoni, and L. Biferale. Reconstruction of turbulent data with deep generative models for semantic inpainting from turb-rot database. *arXiv preprint arXiv:2006.09179*, 2020.

[25] A. T. Catherall, L. Eaves, P. J. King, and S. R. Booth. Floating gold in cryogenic oxygen. *Nature*, 422(6932):579–579, 2003.

[26] X. Chen, S. Liu, R. Sun, and M. Hong. On the convergence of a class of adam-type algorithms for non-convex optimization. *arXiv preprint arXiv:1808.02941*, 2018.

[27] M. Chrust, G. Bouchet, and J. Dušek. Parametric study of the transition in the wake of oblate spheroids and flat cylinders. *J. Fluid Mech.*, 665:199–208, 2010.

[28] M. Chrust, G. Bouchet, and J. Dušek. Numerical simulation of the dynamics of freely falling discs. *Phys. Fluids*, 25(4):044102, 2013.

[29] I. L Claeys and J. F. Brady. Suspensions of prolate spheroids in stokes flow. part 1. dynamics of a finite number of particles in an unbounded fluid. *J. Fluid Mech.*, 251:411–442, 1993.

[30] R. Clift, J. R. Grace, and M. E. Weber. *Bubbles, drops, and particles*. Courier Corporation, 2005.

[31] Wikimedia Commons. File:fal-2017-saunders island, falkland islands-black-browed albatross chick (thalassarche melanophris) 03.jpg — wikimedia commons, the free media repository, 2020. URL https://commons.wikimedia.org/w/index.php?title=File:FAL-2017-Saunders_Island,_Falkland_Islands-Black-browed_albatross_chick_(Thalassarche_melanophris)_03.jpg&oldid=488100881. [Online; accessed 19-January-2021].

[32] AB COMSOL. COMSOL multiphysics reference manual, version 5.3. *COMSOL AB*, 2018.

[33] C. T. Crowe, J. D. Schwarzkopf, M. Sommerfeld, and Y. Tsuji. *Multiphase flows with droplets and particles*. CRC press, 2011.

[34] R. H. Davis, J. M. Serayssol, and E. J. Hinch. The elastohydrodynamic collision of two spheres. *J. Fluid Mech.*, 163:479–497, 1986.

[35] J. R. A. De Koning, E. J. Bakker, and P. C. Rem. Sorting of vegetable seeds by magnetic density separation in comparison with liquid density separation. *Seed Sci. Technol.*, 39(3):593–603, 2011.

[36] S. C. R. Dennis, S. N. Singh, and D. B. Ingham. The steady flow due to a rotating sphere at low and moderate reynolds numbers. *J. Fluid Mech.*, 101(2): 257–279, 1980.

[37] G. Dodbiba, N. Haruki, A. Shibayama, T. Miyazaki, and T. Fujita. Combination of sink–float separation and flotation technique for purification of shredded pet-bottle from pe or pp flakes. *Annu. Rev. Fluid Mech.*, 65(1):11–29, 2002.

[38] P. A. Dunne, J. Hilton, and J. M. D. Coey. Levitation in paramagnetic liquids. *J. Magn.*, 316(2):273–276, 2007.

[39] J. Duplat and A. Mailfert. On the bubble shape in a magnetically compensated gravity environment. *J. Fluid Mech.*, 716, 2013.

[40] J. K. Eaton. Two-way coupled turbulence simulations of gas-particle flows using point-particle tracking. *Int. J. Multiph. Flow*, 35(9):792–800, 2009.

[41] S. Elghobashi and G. C. Truesdell. Direct simulation of particle dispersion in a decaying isotropic turbulence. *J. Fluid Mech.*, 242:655–700, 1992.

[42] S. Elghobashi and G. C. Truesdell. On the two-way interaction between homogeneous turbulence and dispersed solid particles. i: Turbulence modification. *Phys. Fluids A: Fluid Dynamics*, 5(7):1790–1801, 1993.

[43] P. Ern, F. Risso, D. Fabre, and J. Magnaudet. Wake-induced oscillatory paths of bodies freely rising or falling in fluids. *Annu. Rev. Fluid Mech.*, 44:97–121, 2012.

[44] EC EU. Proposal for a directive of the european parliament and of the council on the reduction of the impact of certain plastic products on the environment, 2018.

[45] F. G. Fan and G. Ahmadi. Dispersion of ellipsoidal particles in an isotropic pseudo-turbulent flow field. *J. Fluids Eng.*, 1995.

[46] R. C. Fernow. *Principles of Magnetostatics*. Cambridge University Press, 2016.

[47] K. Fröhlich, M. Meinke, and W. Schröder. Correlations for inclined prolates based on highly resolved simulations. *J. Fluid Mech.*, 901, 2020.

[48] I. Gallily and A. Cohen. On the orderly nature of the motion of nonspherical aerosol particles. ii. inertial collision between a spherical large droplet and an axially symmetrical elongated particle. *J. Colloid Interface Sci.*, 68(2):338–356, 1979.

[49] F. Gallo, C. Fossi, R. Weber, D. Santillo, J. Sousa, I. Ingram, A. Nadal, and D. Romano. Marine litter plastics and microplastics and their toxic chemicals components: the need for urgent preventive measures. *Environ. Sci. Eur.*, 30 (1):13, 2018.

[50] T. S. Galloway, M. Cole, and C. Lewis. Interactions of microplastic debris throughout the marine ecosystem. *Nat. Ecol. Evol.*, 1(5):1–8, 2017.

[51] G. H. Ganser. A rational approach to drag prediction of spherical and nonspherical particles. *Powder Technol.*, 77(2):143–152, 1993.

[52] Q. Gao, W. Zhang, H. Zou, W. Li, H. Yan, Z. Peng, and G. Meng. Label-free manipulation via the magneto-archimedes effect: fundamentals, methodology and applications. *Mater. Horiz.*, 6(7):1359–1379, 2019.

[53] M. R. Gent, M. Menendez, J. Toraño, and I. Diego. Recycling of plastic waste by density separation: prospects for optimization. *Waste Manag. Res.*, 27(2): 175–187, 2009.

[54] R. Geyer, J. R. Jambeck, and K. L. Law. Production, use, and fate of all plastics ever made. *Sci. Adv.*, 3(7):e1700782, 2017.

[55] D. Ghosh, T. Gupta, R. P. Sahu, P. K. Das, and I. K. Puri. Three-dimensional printing of diamagnetic microparticles in paramagnetic and diamagnetic media. *Phys. Fluids*, 32(7):072001, 2020.

[56] P. Gondret, M. Lance, and L. Petit. Bouncing motion of spherical particles in fluids. *Phys. Fluids*, 14(2):643–652, 2002.

[57] I. Goodfellow, Y. Bengio, and A. Courville. *Deep learning*. MIT Press, 2016.

[58] E. Guendelman, R. Bridson, and R. Fedkiw. Nonconvex rigid bodies with stacking. *ACM Trans. Graph.*, 22(3):871–878, 2003.

[59] K. Halbach. Physical and optical properties of rare earth cobalt magnets. *Nucl. Instrum. Methods. Phys. Res. B*, 187(1):109–117, 1981.

[60] J. Happel and H. Brenner. *Low Reynolds number hydrodynamics: with special applications to particulate media*, volume 1. Springer Science & Business Media, 2012.

[61] L. He and D. K. Tafti. A supervised machine learning approach for predicting variable drag forces on spherical particles in suspension. *Powder Technol.*, 345: 379–389, 2019.

[62] A. Hölzer and M. Sommerfeld. New simple correlation formula for the drag coefficient of non-spherical particles. *Powder Technol.*, 184(3):361–365, 2008.

[63] M. Hölzer, A.and Sommerfeld. Lattice Boltzmann simulations to determine drag, lift and torque acting on non-spherical particles. *Comput. Fluids*, 38(3): 572–589, 2009.

[64] B. P. B. Hoomans, J. A. M. Kuipers, W.J. Briels, and W. P. M. van Swaaij. Discrete particle simulation of bubble and slug formation in a two-dimensional gas-fluidised bed: a hard-sphere approach. *Chem. Eng. Sci.*, 51(1):99–118, 1996.

[65] M. Horowitz and C. H. K. Williamson. The effect of reynolds number on the dynamics and wakes of freely rising and falling spheres. *J. Fluid Mech.*, 651: 251–294, 2010.

[66] B. Hu. *Magnetic density separation of polyolefin wastes*. PhD thesis, Delft University of Technology, 2014.

[67] E. Izard, T. Bonometti, and L. Lacaze. Modelling the dynamics of a sphere approaching and bouncing on a wall in a viscous fluid. *J. Fluid Mech.*, 747: 422–446, 2014.

[68] R. Jain, S. Tschisgale, and J. Fröhlich. A collision model for dns with ellipsoidal particles in viscous fluid. *Int. J. Multiph. Flow*, 120:103087, 2019.

[69] J. R. Jambeck, R. Geyer, C. Wilcox, T. R. Siegler, M. Perryman, A. Andrady, R. Narayan, and K. L. Law. Plastic waste inputs from land into the ocean. *Science*, 347(6223):768–771, 2015.

[70] G. B. Jeffery. The motion of ellipsoidal particles immersed in a viscous fluid. *Proceedings of the Royal Society of London. Series A, Containing papers of a mathematical and physical character*, 102(715):161–179, 1922.

[71] M. Jenny, J. Dušek, and G. Bouchet. Instabilities and transition of a sphere falling or ascending freely in a newtonian fluid. *J. Fluid Mech.*, 508:201–239, 2004.

[72] F. Jiang, J. P. Gallardo, and H. I. Andersson. The laminar wake behind a 6: 1 prolate spheroid at 45 incidence angle. *Phys. Fluids*, 26(11):113602, 2014.

[73] G. G. Joseph and M. L. Hunt. Oblique particle–wall collisions in a liquid. *J. Fluid Mech.*, 510:71–93, 2004.

[74] R. Kaiser, L. Mir, and R. A. Curtis. Classification by ferrofluid density separation, April 20 1976. US Patent 3,951,785.

[75] S. E. Khalafalla and G. W. Reimers. Separating nonferrous metals in incinerator residue using magnetic fluids. *Sep. Sci. Technol.*, 8(2):161–178, 1973.

[76] I. Kim, S. Elghobashi, and W. A. Sirignano. On the equation for spherical-particle motion: effect of reynolds and acceleration numbers. *J. Fluid Mech.*, 367:221–253, 1998.

[77] J. Kim, P. Moin, and R. Moser. Turbulence statistics in fully developed channel flow at low reynolds number. *J. Fluid Mech.*, 177:133–166, 1987.

[78] D. P. Kingma and J. Ba. Adam: A method for stochastic optimization. *arXiv preprint arXiv:1412.6980*, 2014.

[79] M. S. Korlie, A. Mukherjee, B. G. Nita, J. G. Stevens, A. D. Trubatch, and P. Yecko. Modeling bubbles and droplets in magnetic fluids. *J.Phys.: Condens. Matter*, 20(20):204143, 2008.

[80] J. G. M. Kuerten. Point-particle dns and les of particle-laden turbulent flow-a state-of-the-art review. *Flow Turbul. Combust.*, 97(3):689–713, 2016.

[81] J. G. M. Kuerten, C. W. M. Van der Geld, and B. J. Geurts. Turbulence modification and heat transfer enhancement by inertial particles in turbulent channel flow. *Phys. Fluids*, 23(12):123301, 2011.

[82] J. B. Kuipers. *Quaternions and rotation sequences: a primer with applications to orbits, aerospace, and virtual reality*. Princeton university press, 1999.

[83] R. Y. S. Lai and L. F. Mockros. The stokes-flow drag on prolate and oblate spheroids during axial translatory accelerations. *J. Fluid Mech.*, 52(1):1–15, 1972.

[84] J. Ling, A. Kurzawski, and J. Templeton. Reynolds averaged turbulence modelling using deep neural networks with embedded invariance. *J. Fluid Mech.*, 807:155–166, 2016.

[85] S. Liu, M. Leaper, and N. J. Miles. Vertical flotation of particles in a paramagnetic fluid. *Powder Technol.*, 261:71–77, 2014.

[86] R. I. Loehrke and H. M. Nagib. Control of Free-Stream Turbulence by Means of Honeycombs: A Balance Between Suppression and Generation. *J. Fluids Eng.*, 98(3):342–351, 09 1976. ISSN 0098-2202.

[87] E. Loth. Drag of non-spherical solid particles of regular and irregular shape. *Powder Technol.*, 182(3):342–353, 2008.

[88] V. Luciani, G. Bonifazi, P. Rem, and S. Serranti. Upgrading of pvc rich wastes by magnetic density separation and hyperspectral imaging quality control. *Waste Manag.*, 45:118–125, 2015.

[89] H. F. S. Lui and W. R. Wolf. Construction of reduced-order models for fluid flows using deep feedforward neural networks. *J. Fluid Mech.*, 2019.

[90] J. Mallinson. One-sided fluxes–a magnetic curiosity? *IEEE T. Magn.*, 9(4): 678–682, 1973.

[91] C. Marchioli. *Collective Dynamics of Particles: From Viscous to Turbulent Flows*, volume 576. Springer, 2017.

[92] C. Marchioli and A. Fantoni, M.and Soldati. Orientation, distribution, and deposition of elongated, inertial fibers in turbulent channel flow. *Phys. Fluids*, 22 (3):033301, 2010.

[93] J. H. Masliyah and N. Epstein. Numerical study of steady flow past spheroids. *J. Fluid Mech.*, 44(3):493–512, 1970.

[94] M. R. Maxey and J. J. Riley. Equation of motion for a small rigid sphere in a nonuniform flow. *The Phys. Fluids*, 26(4):883–889, 1983.

[95] I. Mema, V. V. Mahajan, B. W. Fitzgerald, and J. T. Padding. Effect of lift force and hydrodynamic torque on fluidisation of non-spherical particles. *Chem. Eng. Sci.*, 195:642–656, 2019.

[96] K. A. Mirica, S. S Shevkoplyas, S. T. Phillips, M. Gupta, and G. M. Whitesides. Measuring densities of solids and liquids using magnetic levitation: fundamentals. *J. Am. Chem. Soc.*, 131(29):10049–10058, 2009.

[97] K. A. Mirica, S. T. Phillips, C. R. Mace, and G. M. Whitesides. Magnetic levitation in the analysis of foods and water. *J. Agric. Food Chem.*, 58(11):6565–6569, 2010.

[98] B. Mirtich and J. Canny. Impulse-based simulation of rigid bodies. In *Proceedings of the 1995 symposium on Interactive 3D graphics*, pages 181–ff, 1995.

[99] P. H. Mortensen, H. I. Andersson, J. J. J. Gillissen, and B. J. Boersma. Dynamics of prolate ellipsoidal particles in a turbulent channel flow. *Phys. Fluids*, 20(9): 093302, 2008.

[100] L. Muchova, E. Bakker, and P. Rem. Precious metals in municipal solid waste incineration bottom ash. *Water Air Soil poll.*, 9(1-2):107–116, 2009.

[101] J. L. Neuringer and R. E. Rosensweig. Ferrohydrodynamics. *Phys. Fluids*, 7(12): 1927–1937, 1964.

[102] A. Oberbeck. üeber stationäre Flüssigkeitsbewegungen mit Berücksichtigung der inneren Reibung. *J. Reine. Angew. Math.*, 1876(81):62–80, 1876.

[103] S. Odenbach. Ferrofluids-magnetisable liquids and their application in density separation. *Phys. Sep. Sci. Eng.*, 9(1):1–25, 1998.

[104] B. J. O'Donnell and B. Helenbrook. Drag on ellipsoids at finite reynolds numbers. *At. Sprays*, 15(4), 2005.

[105] OECD. *Environment at a Glance 2020*. 2020. URL https://www.oecd-ilibrary.org/content/publication/4ea7d35f-en.

[106] R Ouchene. Numerical simulation and modeling of the hydrodynamic forces and torque acting on individual oblate spheroids. *Physics of Fluids*, 32(7): 073303, 2020.

[107] R. Ouchene, M. Khalij, A. Tanière, and B. Arcen. Drag, lift and torque coefficients for ellipsoidal particles: From low to moderate particle Reynolds numbers. *Comput. Fluids*, 113:53–64, 2015.

[108] R. Ouchene, M. Khalij, B. Arcen, and A. Tanière. A new set of correlations of drag, lift and torque coefficients for non-spherical particles and large Reynolds numbers. *Powder Technol.*, 303:33–43, 2016.

[109] R. Ouchene, M. Khalij, B. Arcen, and A. Tanière. A new set of correlations of drag, lift and torque coefficients for non-spherical particles and large reynolds numbers. *Powder Technol.*, 303:33–43, 2016.

[110] S. S. Papell. Low viscosity magnetic fluid obtained by the colloidal suspension of magnetic particles patent(low density and low viscosity magnetic propellant for use under zero gravity conditions). *Patent NumberUS-PATENT-3, 215, 572; US-PATENT-APPL-SN-315096; US-PATENT-CLASS-149-2*, 1965.

[111] L. Parker. We made plastic. we depend on it. now we're drowning in it. *Nat. Geo.*, 2018.

[112] R. L. Pitter, H. R. Pruppacher, and A. E. Hamielec. A numerical study of viscous flow past a thin oblate spheroid at low and intermediate reynolds numbers. *J. ATMOS. SCI.*, 30(1):125–134, 1973.

[113] H. Polinder and P. C. Rem. Magnet and device for magnetic density separation, December 5 2017. US Patent 9,833,793.

[114] P. C. Rem, F. Di Maio, B. Hu, G. Houzeaux, L. Baltes, and M. Tierean. Magnetic fluid equipment for sorting secondary polyolefins from waste. *Environ. Eng. Manag. J.*, 12(5), 2013.

[115] F. W. Roos and W. W. Willmarth. Some experimental results on sphere and disk drag. *AIAA j.*, 9(2):285–291, 1971.

[116] L. Rosendahl. Using a multi-parameter particle shape description to predict the motion of non-spherical particle shapes in swirling flow. *Appl. Math. Model.*, 24 (1):11–25, 2000.

[117] R. E. Rosensweig. Fluidmagnetic buoyancy. *AIAA J.*, 4(10):1751–1758, 1966.

[118] R. E. Rosensweig. *Ferrohydrodynamics*. Dover Publications, 2013.

[119] S. Ruder. An overview of gradient descent optimization algorithms. *arXiv preprint arXiv:1609.04747*, 2016.

[120] S. K. P. Sanjeevi, J. A. M. Kuipers, and J. T. Padding. Drag, lift and torque correlations for non-spherical particles from Stokes limit to high Reynolds numbers. *Int. J. Multiph. Flow*, 106:325–337, 2018.

[121] S. K.P. Sanjeevi and J. T. Padding. On the orientational dependence of drag experienced by spheroids. *J. Fluid Mech.*, 820:1–13, 2017.

[122] F. O. Sarghini, G. De Felice, and S. Santini. Neural networks based subgrid scale modeling in large eddy simulations. *Comput. Fluids*, 32(1):97–108, 2003.

[123] L. Schiller and A. Naumann. Über die grundlegenden berechnungen bei der schwerkraftaufbereitung. *Zeitschrift des Vereines deutscher Ingenieure*, 1933.

[124] S. Serranti and G. Bonifazi. Techniques for separation of plastic wastes. In *Use of Recycled Plastics in Eco-efficient Concrete*, pages 9–37. Elsevier, 2019.

[125] S. Serranti, V. Luciani, G. Bonifazi, B. Hu, and P. C. Rem. An innovative recycling process to obtain pure polyethylene and polypropylene from household waste. *Waste Manag.*, 35:12–20, 2015.

[126] L. Shen and E. Worrell. Plastic recycling. In *Handbook of recycling*, pages 179–190. Elsevier, 2014.

[127] A. R. Shenoy and C. Kleinstreuer. Flow over a thin circular disk at low to moderate reynolds numbers. *J. Fluid Mech.*, 605:253–262, 2008.

[128] H. Shent, R. J. Pugh, and E. Forssberg. A review of plastics waste recycling and the flotation of plastics. *Resour. Conserv. Recycl.*, 25(2):85–109, 1999.

[129] J. Shimoiizaka, K. Nakatsuka, T. Fujita, and A. Kounosu. Sink-float separators using permanent magnets and water based magnetic fluid. *IEEE T. Magn.*, 16 (2):368–371, 1980.

[130] M. I. Shliomis. Magnetic fluids. *Soviet Physics Uspekhi*, 17(2):153, 1974.

[131] M. I. Shliomis. Ferrohydrodynamics: Retrospective and issues. In *Ferrofluids*, pages 85–111. Springer, 2002.

[132] H. A. Shute, J. C. Mallinson, D. T. Wilton, and D. J. Mapps. One-sided fluxes in planar, cylindrical, and spherical magnetized structures. *IEEE T. Magn.*, 36(2): 440–451, 2000.

[133] C. Siewert, R. P. J. Kunnen, M. Meinke, and W. Schröder. Orientation statistics and settling velocity of ellipsoids in decaying turbulence. *Atmos. Res.*, 142: 45–56, 2014.

[134] C. Singh, A. K. Das, and P. K. Das. Levitation of non-magnetizable droplet inside ferrofluid. *J. Fluid Mech.*, 857:398–448, 2018.

[135] N. Singh, D. Hui, R. Singh, I. P. S. Ahuja, L. Feo, and F. Fraternali. Recycling of plastic solid waste: A state of art review and future applications. *Compos. B. Eng*, 115:409–422, 2017.

[136] R. Smolkin, Y. M. Garin, V. S. Krokhmal, and O. P. Sayko. New process for placer gold recovery by means of magnetic separation. *IEEE T. Magn.*, 28(1): 671–674, 1992.

[137] W. Steffen, J. Grinevald, P. Crutzen, and J. McNeill. The anthropocene: conceptual and historical perspectives. *Philos. Trans. R. Soc. A*, 369(1938):842–867, 2011.

[138] S. Tajfirooz, M. Hausmann, J. Meijer, J.and Fr olich, and J. G. M. Kuerten. A statistical-learning method for predicting hydrodynamical drag, lift and pitching torque on spheroidal particles. *Physical Review E (under review)*, 2020.

[139] S. Tajfirooz, J. G. Meijer, R. A. Dellaert, A. M. Meulenbroek, J. C. H. Zeegers, and J. G. M. Kuerten. Direct numerical simulation of magneto-archimedes separation of spherical particles. *J. Fluid Mech.*, 910:A52, 2021.

[140] M. M. Tavakol, O. Abouali, M. Yaghoubi, and G. Ahmadi. Dispersion and deposition of ellipsoidal particles in a fully developed laminar pipe flow using non-creeping formulations for hydrodynamic forces and torques. *Int. J. Multiph. Flow*, 75:54–67, 2015.

[141] A. Tewari. *Atmospheric and space flight dynamics*. Springer, 2007.

[142] S. Tschisgale, L. Thiry, and J. Fröhlich. A constraint-based collision model for Cosserat rods. *Arch. Appl. Mech.*, 89(2):167–193, 2019. ISSN 14320681.

[143] K. Ueno, M. Higashitani, and S. Kamiyama. Study on single bubbles rising in magnetic fluid for small weber number. *J. Magn.*, 149(1-2):104–107, 1995.

[144] M. A. T. Van Hinsberg, J. H. M. ten Thije Boonkkamp, and H. J. Clercx. An efficient, second order method for the approximation of the basset history force. *J. Comput. Phys.*, 230(4):1465–1478, 2011.

[145] A. van Silfhout and B. Erné. Magnetic detection of nanoparticle sedimentation in magnetized ferrofluids. *J. Magn. Magn. Mater.*, 472:53–58, 2019.

[146] A. M van Silfhout, H. Engelkamp, and B. H. Erné. Magnetic sedimentation velocities and equilibria in dilute aqueous ferrofluids. *J. Phys. Chem. B*, 124 (36):7989–7998, 2020.

[147] B. van Wachem, M. Zastawny, F. Zhao, and G. Mallouppas. Modelling of gas-solid turbulent channel flow with non-spherical particles with large Stokes numbers. *Int. J. Multiph. Flow*, 68:80–92, 2015. ISSN 03019322.

[148] L. L. Vatta. Floating diamonds with nanomagnetic particles. In *Macromolecular Symposia*, volume 225, pages 221–228. Wiley Online Library, 2005.

[149] G. A. Voth. Disks aligned in a turbulent channel. *J. Fluid Mech.*, 772:1–4, 2015.

[150] G. A. Voth and A. Soldati. Anisotropic particles in turbulence. *Annu. Rev. Fluid Mech.*, 49:249–276, 2017.

[151] O. R. Walton. Numerical simulation of inelastic, frictional particle-particle interactions. In Rocco M. C., editor, *Particulate two-phase flow*, chapter 25, pages 884–911. Butterworth-Heinemann, 1993.

[152] W. W. Willmarth, N. E. Hawk, and R. L. Harvey. Steady and unsteady motions and wakes of freely falling disks. *The Phys. Fluids*, 7(2):197–208, 1964.

[153] F. L. Yang and M. L. Hunt. Dynamics of particle-particle collisions in a viscous liquid. *Phys. Fluids*, 18(12):121506, 2006.

[154] M. Zastawny, G. Mallouppas, F. Zhao, and B. Van Wachem. Derivation of drag and lift force and torque coefficients for non-spherical particles in flows. *Int. J. Multiph. Flow*, 39:227–239, 2012.

[155] H. Zhang, G. Ahmadi, F. G. Fan, and J. B. McLaughlin. Ellipsoidal particles transport and deposition in turbulent channel flows. *Int. J. Multiph. Flow*, 27 (6):971–1009, 2001.

[156] P. Zhao, J. Xie, F. Gu, N. Sharmin, P. Hall, and J. Fu. Separation of mixed waste plastics via magnetic levitation. *Waste Manag.*, 76:46–54, 2018.

[157] T. Zhu, F. Marrero, and L. Mao. Continuous separation of non-magnetic particles inside ferrofluids. *Microfluid. Nanofluid.*, 9(4-5):1003–1009, 2010.

Acknowledgements

In the course of my PhD, many people have been directly or indirectly involved in my research. The list of people who accompanied me on this journey is very long. However, I want to particularly express my gratitude to those who had significant contributions to this project. First of all, I would like to thank my direct supervisor Hans. Hans, I got to know you first as a teacher during my master studies. Since the very first lecture of "Modeling of Physical Phenomena", your knowledge, discipline, and pragmatic way of thinking have been inspiring for me. I am deeply grateful for the opportunity you afforded me to grow both personally and professionally, and for your support throughout these years. Next, I want to express my deep gratitude to my co-supervisor, Jos for his supervision, impactful experimental insights, and support. Hans and Jos, the unique blend of your leadership and your sense of humor made this research collaboration productive and enjoyable. Rik, thank you for your contributions to the experimental research, and the good times outside working hours.

My thanks are also extended to my defense committee for devoting their precious time to evaluate my thesis. Special thanks should be given to Jochen Fröhlich and his research group for hosting me at TU Dresden, and for the fruitful research collaboration. The project user committee members, Peter Rem, Jaap van de Hoek, Bin Hu, and Jesper Wijnja are also gratefully acknowledged for their feedback.

Without the students with whom I worked on this project, this path would have been far rockier and less joyful. I learned many things from each of you. Aled, it has been a truly pleasurable experience to work with you first as a supervisor and later as a colleague. Your contribution to this project was immense. Max, I very much enjoyed our scientific discussions that were often prolonged to lunch hours. It was a pleasure to have you in Eindhoven. Jochem, your perseverance in both experimental and numerical research was unique. Leon, your contribution to the "Turbulent" side of the project (unfortunately not included in this thesis) is remarkable.

Next, I wish to thank my great colleagues Erwin, Robin, Camila, Naud, Robbert, Haiyu, Nard, Bersan, Jinlin, Conrad, Abhijit, Aromal, Marie, Faizan, Rahul, Aravind, Xin, and others who made the daily work in Gemini North pleasant. Marzie and Aida, thank you for your company during lunches and coffee breaks. Special thanks to Marjan and Linda for bringing energy and harmony to the group. Marjan, I will miss your unrestrained waves of laughter in Gemini North hallways. Performing numerical simulations presented in this thesis would have been almost impossible without the technical support of Jan Hasker. Alireza, I want to thank you for all the discussions, your support and willingness to help me whenever I gave you a call. I would also like to express my great appreciation to Mandy Barker for generously letting me use one of her works as the main design element of the cover of this book. Shahrzad, thank you very much for designing the cover page.

Last, but definitely not the least, I want to thank my family, Johan and my friends for their support and encouragement that kept me going in the past four years.

Curriculum Vitae

Sina Tajfirooz was born on 07-08-1989 in Shiraz, Iran. He finished his secondary education in 2007 at Tohid high school in Shiraz and obtained his bachelor degree in mechanical engineering in 2011 at Persian Gulf University in Bushehr, Iran. After finishing his undergraduate studies, he worked as a design engineer in the oil and gas sector in Iran. In 2014, he moved to the Netherlands to join the master program Mechanical Engineering at Eindhoven University of Technology (TU/e). As a part of his master program, he worked as an intern researcher in DAF trucks N.V. where he was involved in numerical modelling of heat transfer in internal combustion engines. In 2016, he graduated within the group of Harald van Brummelen on the development of stabilized finite element models for flows in Flow-Induced Vibration. From 2016 he started a PhD in computational multiphase flow in the mechanical engineering department of TU/e. His project, the results of which are presented in this dissertation, addresses a computational study of particle-laden flows in magnetic density separation. The project was supervised by prof. dr. J. G. M. Kuerten and dr. ir. J. C. H. Zeegers and it was a collaboration between TU/e, NWO and UminCorp.

List of Publications & Conference Contributions

Publications

1. S. Tajfirooz, J.G. Meijer, R.A. Dellaert, A.M. Meulenbroek, J.C.H. Zeegers, and J.G.M. Kuerten (2021). Direct numerical simulation of magneto-Archimedes separation of spherical particles. *Journal of fluid mechanics*, 910, A52

2. S. Tajfirooz, M. Hausmann, J.G. Meijer, J.G.M. Kuerten, J.C.H. Zeegers, and J. Fröhlich (2020). A statistical learning method for predicting hydrodynamical drag, lift and pitching torque on spheroidal particles *Physical Review E* (Accepted, to be published).

3. L.C. Thijs, R.A. Dellaert, S. Tajfirooz, J.C.H. Zeegers, and J.G.M. Kuerten (2020). Reynolds-number-dependent honeycomb-generated wake turbulence *Journal of Turbulence* (Under review).

4. R.A. Dellaert, L.C. Thijs, S. Tajfirooz, J.C.H. Zeegers, and J.G.M. Kuerten (2021). Reducing turbulence intensity with honeycombs *European Journal of Mechanics - B/Fluids* (In preparation).

Conference contributions

1. Tajfirooz, S. (2018). Dynamics of nonmagnetic almost neutrally buoyant particles in a magnetic fluid. *12th European Fluid Mechanics Conference*, TU Wien, Vienna, Austria.

2. Tajfirooz, S. (2019). Direct Numerical Simulation of Magneto-Archimedes Levitation of Nonmagnetic Particles. *10th International Conference on Multiphase Flow*, Windsor Barra Hotel, Rio de Janeiro, Brazil.